3D Printed Stretchable Electronics: Fabrication using Aerosol Jet, Fundamental Mechanics, and Applications

Submitted in partial fulfillment of the requirements for

the degree of

Doctor of Philosophy

in

Mechanical Engineering

Jacob Brenneman

B.A., Physics, Goshen College

M.S., Mechanical Engineering, Carnegie Mellon University

Carnegie Mellon University

Pittsburgh, PA

December, 2022

© Jacob Brenneman, 2022

All Rights Reserved

Acknowledgements

The work highlighted in this thesis would not have been possible without the help and support of advisors, collaborators, friends, and family. First, my advisor Professor Rahul Panat has provided incredible support both personally and academically throughout my PhD experience. I have appreciated his advice on navigating in-depth research, providing clear expectations for completing my degree, and perspective during difficult life moments. I want to also thank my thesis committee members, Professor Gary Fedder, Professor Maarten de Boer, and Professor Sarah Bergbreiter. Gary Fedder was a close collaborator and instrumental in this work, and I greatly appreciate the insight and direction he provided.

I also want to thank my fellow group members and friends who were a large part of my last four years at Carnegie Mellon: Mert Arslanoglu, Sandy Ritchie, Chunshan Hu, Sanjida Jahan, Rit Bezbaruah, Dr. Bin Yuan, Dr. Azahar Ali, and Dr. Mohammad Sadeq Saleh. A special thanks goes to Derya Tansel who was such a close collaborator in this research that there is a section in the appendix to detail who was the lead on the various tasks completed in this work.

None of this would have been possible without the unwavering support and love of my wife Annalisa. She went from staying home to be with Margaret and Irene for their first year while finishing her master's degree, to a successful job to support us all, while being a constant source of love and support. I started my PhD as a new father of month-old twin girls, and we added Harriet to our family last year and it's been amazing seeing them grow up throughout my time at CMU. It was truly an honor to share their pre-school years with my post-school years. A very big thanks goes to Karen and Jim Harder for spending so much time with Margaret and Irene during the pandemic and making great family memories. A very special thanks goes to my mom who has always been caring and compassionate despite facing very difficult times in

the last few years. To my dad, who, among many many other things, gave me the spark and interest in science and gave me the best advice to “keep track of the units!”

Finally, I want to acknowledge the funding sources that made this research possible and the collaborating laboratories that provided access to equipment. Partial funding support came from the Department of Energy/National Energy Technology Laboratory (DE-FE0031743, DE-FE0026170), National Science Foundation (#1747608, #1757117), National Institute of Health (#RF1NS110483), an internal Moonshot award, and a Pennsylvania Health Infrastructure Grant. Also, the materials characterization facility at Carnegie Mellon University provided open access to cutting-edge microscopy equipment with great staff to provide invaluable assistance and maintenance. The micro robotics laboratory led by Professor Sarah Bergbreiter, and the soft machines laboratory led by Professor Carmel Majidi provided easy access and organized scheduling to great equipment.

Abstract

Electrical signals form the basis for information transfer in several biological systems and devices that capture these signals are of significant interest to the healthcare industry. Such devices are currently made from Si based components and metal interconnects and typically have an elastic modulus about 3-4 orders of magnitude higher than that of biological tissue. This gap has spurred the development of stretchable electronic devices where a soft platform 'hosts' the mechanically stiff electrical elements such as chips and interconnects, while the low elastic modulus substrate achieves a seamless interface with the biological tissue of interest. Such systems are playing an increasingly important role in emerging areas such as soft robotics and smart clothing. In this thesis, aerosol jet nanoparticle 3D printing is used to create a stretchable electronic system consisting of three-dimensional interconnects enabling multi-layered connections embedded within a thin (<100 µm in thickness) biocompatible elastomer membrane where elastic modulus gradients are used to mitigate the effects of the system stress.

The stretchable interconnect system chosen for this work is fabricated via a wafer-compatible process consisting of silver conductor encapsulated by polyimide printed directly on a polydimethylsiloxane (PDMS) elastomer substrate, followed by thermal sintering/curing. The different ideal processing conditions for each material result in several problems including delamination between polyimide layers, low electrical conductivity, and cracking of the 3D interconnects during fabrication. The delamination problem is solved by understanding the underlying mechanisms via a hypothesis-driven experimental and theoretical investigation to identify processing conditions that can eliminate delamination. The cracking problem for silver interconnects is solved by first identifying that the cracks originate due to capillary pressure prior to sintering, followed by changes to the process to prevent their formation. Fully embedded stretchable interconnects are enabled by the development of a compatible process that retains the stretchability of the PDMS and electrical conductivity of the silver. A method to print 3D pillars that extend through the top PDMS layer is developed to create multi-layered interconnection and external connection points, and Electrocardiogram (ECG) signals are captured by a multi-layered skin-wearable device fabricated with the developed process. The research presented in this thesis aims to develop an additive fabrication method for stretchable electronics, understand the fundamental mechanics of such systems, and use this knowledge to create a high-fidelity stretchable system that can capture bioelectronic signals.

Table of Contents

List of Tables

List of Figures

Chapter 1

Introduction

Biological systems, such as the nervous system in the human body, are extremely complex and soft electronic systems that are capable of multiple sensing modalities, signal transmission, signal processing, and return signal transmission to actuate responses to various inputs. Conventional electronic systems aim to do similar tasks, but their hardware is based on electron conduction rather than ionic and chemical signal transmission present in the nervous system.[1] The cells making up the nervous system and human body are soft structures relative to conventional electronic materials, and devices capable of sensing biological signals while also deforming with the soft human tissue are becoming increasingly important in healthcare,[2] and human-machine interfaces.[3] For example, conformal and comfortable sensing devices mimicking skin enable long-term health monitoring of sensitive neonates,[4] while soft wearable robotics can actively support rehabilitation of complex joints while maintaining full range of motion by mimicking the musculoskeletal system.[5] In fact, soft and conformal wearable biomonitoring sensors are considered to be a major part of the future of health care.[6]

One of the primary challenges in developing stretchable electronic devices stems from the disparate mechanical properties of conventional, high-performance electronics and soft stretchable substrates where the elastic modulus and strain to failure for individual components can vary over several orders of magnitude. The elastomeric substrate survives large strains (>100%), while the electronic materials typically only withstand 1-2% strain before rupture. Individual islands of stiff material are commonly utilized in stretchable and flexible electronics

so that during stretching or flexing, the applied strain is accommodated primarily by the elastomer substrate and the islands experience little strain.[7,8] However, these islands can still fail in several ways including delamination caused by stress concentrations at the interface, or by reaching a critical size where the island itself cracks. The stress at the interface can be reduced by introducing a material of intermediate stiffness between the soft elastomeric material and the stiff electronic material to create a stiffness gradient.[8,9] Exploiting ultrathin geometries,[10] and strain isolation[11] achieved by surrounding the stiff materials in liquid or very soft gel are additional methods to mitigate the modulus mismatch and incorporate stiff electronic materials in stretchable systems. Connection between the strain islands or individual components is made with electronic interconnects and they must accommodate a large strain as they deform along with the elastomer substrate.

Techniques used to design electrical interconnects capable of withstanding large strain are typically separated into two categories – the use of intrinsically stretchable electronic materials and the use of engineered geometries with patterned conventional electronic (stiff) materials.[12] The intrinsically stretchable electronic materials shown in Figure 1.1A-B include liquid metal, conductive polymers, and elastomer-metallic composite materials which can maintain electrical conductivity during deformation.[13] Liquid metal interconnects are capable of extremely high stretchability of up to 800% and have demonstrated some self-healing capabilities, but in general suffer significant changes in resistance during stretching due to the thinning of the cross section.[14,15] Composite materials of elastomers and electrically conductive fillers are also capable of extremely high stretchability, but are typically less conductive, and are difficult to pattern with high resolution to facilitate connections with other components.[16,17] In the second method shown in Figure 1.1C, conventional electronic materials are patterned with engineered geometries (e.g., buckled films or meandering interconnects) to achieve

deformable interconnects.[18-20] These engineered geometries have high conductivity and the resistance is stable throughout stretching due to the locally low strain, but the areal coverage of the meandering trace is relatively large. Using patterned geometries and metallic conductors, rather than intrinsically stretchable conductors, has the additional advantage of compatibility with conventional device assembly techniques to integrate off-the-shelf components.[21] Using a combination of both engineered geometries and intrinsically stretchable materials, recent advances in materials, fabrication technologies, and device design have enabled stretchable device components such as batteries,[22] displays,[23] capacitors,[24] and even transistors.[25]

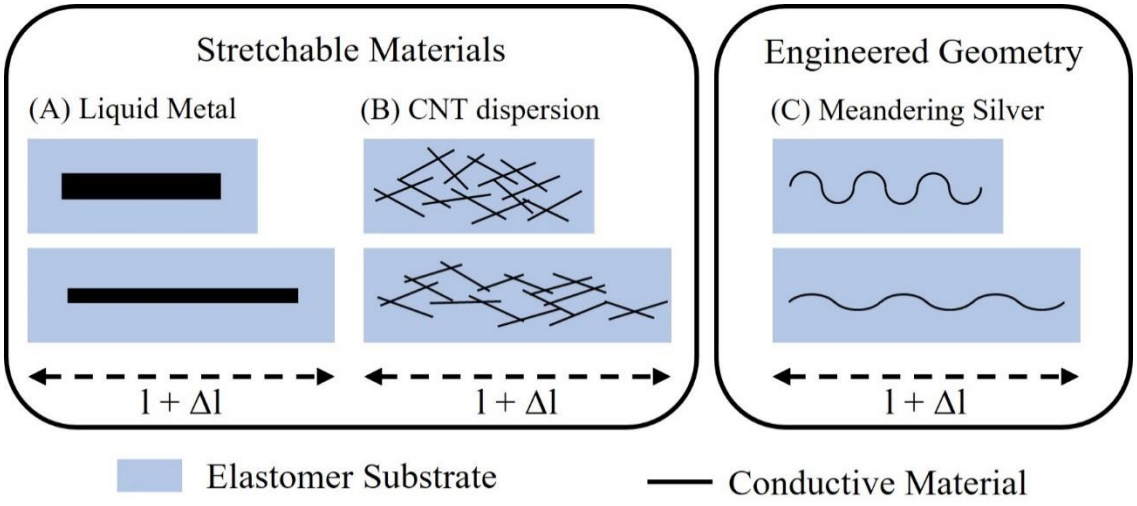

Figure 1.1: Design categories for stretchable interconnects. Intrinsically stretchable materials such as (A) liquid metal, or (B) a carbon nanotube network in an elastomer matrix can reach high strain before failure. Engineered geometries such as a (C) meandering silver traces can utilize conventional electronic materials with little change in resistance during stretching.

Material jetting, a type of 3D printing (or more formally called additive manufacturing or AM) process, provides an attractive alternative to lithographic techniques typically used to pattern engineered geometries in stretchable electronic platforms. Additive techniques offer distinct advantages such as the ability to pattern on a curved and uneven surface, simplicity in processability, availability of a wide array of printable materials, minimization of material

waste, digitized manufacturing, rapid prototyping capability, and the ability to print 3D architectures.[26] These advantages typically come at the cost of larger feature sizes, lower resolution, a slower serial process, and less mature processing techniques. Inkjet printing has been used extensively to fabricate functional electronics at length scales of 50-100 μm and requires the ink to have a viscosity <10 cPs. Coarse 3D features were demonstrated using this technique.[27,28] Electrohydrodynamic printing has demonstrated high resolution printed features in 2D and 3D using smaller nozzle diameters than inkjet using an additional electrostatic force by applying a voltage between the nozzle and the grounded substrate.[29,30] Laser-induced forward transfer (LIFT) can directly print donor material in either the solid or liquid phase in metallic, organic or carbon based materials.[31] Two photon induced photopolymerization and metal ion reduction have been shown to print 3D structures in both metals and polymers at micron and sub-micron scale features.[32,33] The additive printing techniques have contributed to the trends of miniaturization, personalization, and elasticity (i.e., having a softness similar to the biological tissue) for biomonitoring devices.

Aerosol jet is an additive manufacturing technique rapidly gaining popularity due to the ability to print fine features down to 10 μm in a wide range of ink viscosities and formulations including polymers, ceramics, and metallic inks.[34] This technique was developed primarily as a 2D and 2.5D printing technology and has recently been extended to print complex 3D features without any support structures including lattice structures[35] and micropillars[36] for functional power[37] and sensor[38-41] components. Realizing these functional 3D features in a stretchable electronic system is difficult or even impossible to achieve via traditional lithographic techniques.

Aerosol jet printing can incorporate heterogenous materials with 3D features to enable complex device architectures on a micron scale in a digitized workflow. However, integrating

functional 3D structures on a stretchable electronics platform via aerosol jet remains an unexplored area capable of unlocking rich feature possibilities. One such feature is the fabrication of vertical interconnect accesses (VIAs, also known as vias) which are commonly used in rigid circuit boards, but remain non-trivial to introduce into stretchable electronics.[42] Multi-layered designs allow for several stiff components to be stacked on one another and reduce the areal footprint, enabling highly stretchable and complex devices. Currently, most stretchable electronic systems utilize a single layer, and the area available to place the components is limited since there needs to be stretchable regions to accommodate the globally applied strain (100% coverage with stiff strain islands results in a non-stretchable device).[7,8] Investigating and solving fabrication challenges on a fundamental level for multi-material printing and demonstrating a functional 3D printed VIA on a thin stretchable substrate, therefore represents an important contribution to the fields of additive manufacturing and stretchable electronics.

In this thesis, a fabrication process is proposed and developed to directly print stretchable metallic interconnects on a thin polydimethylsiloxane (PDMS) substrate using an aerosol jet printing technique. A second layer of PDMS is then included to fully embed the interconnect, and 3D printed pillars are used to extend through the PDMS layer to make external connections and function as a VIA in multi-layered circuit. Chapter 2 describes the design and fabrication process flow of the stretchable electronic system in detail. Chapter 3 investigates the use of PDMS as a stretchable substrate material capable of supporting the curing and sintering of subsequently printed polymer and metallic layers. The PDMS is subjected to high temperatures under a vacuum environment to determine the effect of temperature on the mechanical properties of interest, including elastic modulus and stretchability. After the PDMS is shown to retain desirable mechanical characteristics, prototype interconnects are fabricated.

Chapter 4 investigates the cause of delamination that is observed and investigated with varied geometry in the printed interconnect. Analytical models are developed to test two hypotheses that the delamination is driven either by thermoelastic strain energy due to thermal expansion mismatch, or vapor pressure from absorbed moisture. Finite element models are developed to verify analytical results and to include complex geometry not captured by the analytical model. The delamination is shown to be driven by vapor pressure, and the parameterized model provides delamination mechanism maps and design guidelines for both geometry of the interconnect and process parameters to avoid delamination.

Following the solution to the delamination problem, 3D features are directly printed on the PDMS and polyimide support pad with the vacuum process developed in Chapter 3 and Chapter 4. However, the three-dimensional pillars exhibit cracking at the base of the pillar, and the conductivity of the interconnects is much lower than expected. Chapter 5 investigates the effect of process environment on the sintering of the nanoparticle ink and the resulting microstructure, electrical conductivity, and cracking. A stepwise experimental procedure of the sintering environment (i.e., vacuum, N_2 at atmospheric pressure, and air) is conducted to isolate the conditions under which cracking occurs and compare the resulting microstructure and conductivity. An air environment during thermal sintering does not result in cracking and more effectively removes the ligands surrounding the silver nanoparticle ink, allowing for increased coalescence, and increased electrical conductivity of the printed conductor. However, the air environment also destroys the PDMS at high temperatures, and a hybrid (air followed by vacuum) process sinters the silver and achieves high conductivity without cracking while preserving the mechanical properties of the PDMS.

Chapter 6 utilizes the mechanistic understanding and process developed in the previous chapters to demonstrate a fully embedded electrical interconnect with microscale pillars used

as a VIA for external connection and interconnection to another layer of printed conductors. The stretchable interconnect is mechanically and electrically characterized with tensile tests for three different meander angles to investigate the strain to failure, and cycles to failure. Finally, all the knowledge gained from the previous investigations enables the fabrication of a multi-layered skin-wearable stretchable device capable of capturing an electrocardiogram (ECG) signal with comparable performance to a commercially available electrode. Chapter 7 summarizes the thesis and discusses the future work to improve manufacturability and performance of the stretchable electronics system and fabrication process developed in this thesis.

Chapter 2

Design and Fabrication of 3D Multi-Material Electrical Interconnect

A major challenge in realizing stretchable electronics is the fabrication of the conductors which connect the various components of the circuit. This is true for components that are intrinsically stretchable as well as for those that are strain-isolated via rigid islands. The bulk of the research in this thesis is centered around exploring fabrication techniques and failure analysis to demonstrate robust stretchable interconnects directly printed on a PDMS substrate. Inclusion of 3D features or structures at the terminal points of the interconnect that enable connections with an external circuit, or the next layer of a multi-layered circuit (VIA) is another central goal of this thesis. This section details both the design of the 3D stretchable interconnects, and the fabrication techniques that enable the realization of the design.

2.1 Design of Meandering Interconnect

The electrical interconnect in this thesis is a meandering silver trace, encapsulated in polyimide, and fully embedded in PDMS as shown in Figure 2.1A. The meanders are defined by the meandering angle (θ), width of the interconnect (w), and the radius of curvature (r) as shown in Figure 2.1E. The interconnect is directly printed onto the PDMS and does not require a transfer step. The meander angle is varied throughout this thesis to investigate its effect on the strain to failure, but unless otherwise noted the radius of the meander, r, is 500 μm, and the width of the silver is 30 μm and the width of the PI, w, is 200 μm. Pads are located at the

terminal ends of the interconnect and are tapered at the transition from interconnect to pad to reduce stress concentration during stretching of the interconnect as shown in Figure 2.1B. The pads can then host 3D printed features such as pillars for external connection or as a VIA for multi-layered circuitry, lattices structures for battery electrodes or impact energy absorption, or freeform features for antenna structures. Pillars are utilized as the primary structure in this thesis because of the simplicity of design and fabrication, and because they mimic the typical shape of a VIA in a printed circuit board. Another layer of PDMS fully embeds the interconnect while the tips of the pillars are exposed to allow external connections as shown in Figure 2.1C.

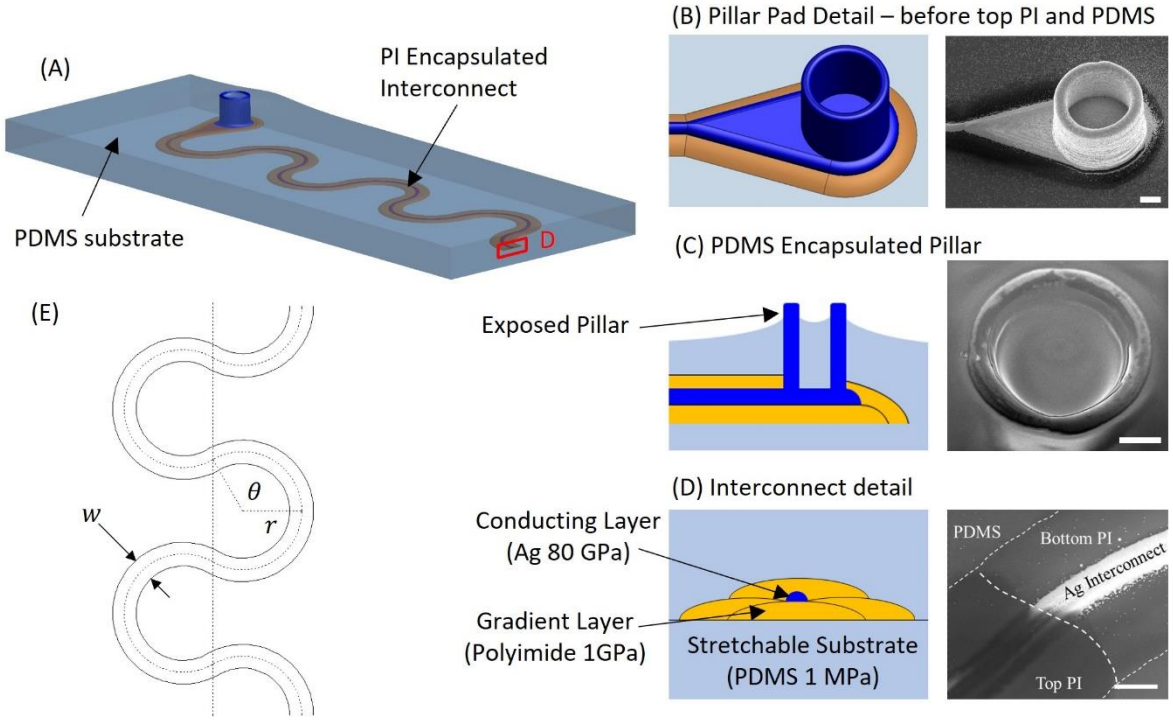

Figure 2.1: Design of 3D printed stretchable interconnects used in this thesis. (A) A schematic of the embedded and encapsulated meandering interconnect with (B) details of the pillar pad including the first polyimide layer and silver, but before the top layer of polyimide and PDMS have been applied, (C) the fully encapsulated pillar with the pillar tips exposed for external connection, and (D) the interconnect cross section showing each individual layer and the corresponding SEM images. The scale bars for the SEM images are 50 µm. (E) Details the design parameters for the meandering interconnects.

The pads at the terminal ends of the interconnect act as stiff island structures, such that under tensile deformation the strain is accommodated by the relatively soft elastomer and the stiff islands experience significantly reduced local strains and are connected to one another via the interconnects. In early designs, these stiff islands were constructed by the electronic components themselves.[7,8] However, mechanical stress is concentrated at the interface due to the large elastic modulus mismatch between the materials precisely at the location where the lowest bond energy in the system is often located. To address these issues, a material of intermediate stiffness can be introduced between the electronic component and the stretchable elastomer to create a stiffness gradient.[43-47] The presence of the stiffness gradient significantly reduces the strain at the interface of the electronic material and the intermediate material thereby reducing the delamination risk.[9] One drawback of introducing a stiffness gradient is that the area or length of the stiff island increases, which reduces the total area or length of the elastomer region which accommodates the majority of the strain. Encapsulating the meandering metal interconnects in a stiffness gradient can also be utilized traces to increase the strain to failure of the interconnects, with increases as high as 250% reported.[18,48]

In the work covered in this thesis, the stretchable elastomer material is polydimethylsiloxane (PDMS) (Sylgard 184, Dow Corning Corporation, Midland, MI), which has an elastic modulus of ~1×10^6 Pa when cured, and the electronically conductive material is sintered silver nanoparticle ink (Metalon JS-A426, NovaCentrix, Austin, TX or Prelect TPS 50, Clariant, Frankfurt, Germany) which has an elastic modulus of ~8×10^{10} Pa. Printed and cured polyimide (PI) (PI 2574, HD MircroSystems, Parlin, NJ) is used as an intermediate stiffness material between the silver and the PDMS and has an elastic modulus of ~1×10^9 Pa. More details on the preparation of materials, printing, sintering/curing, and material properties are described in Section 2.2. The first PI layer is shown in Figure 2.1B under the Ag before the

second layer of PI is printed. The second layer of PI can then be printed directly over the pad, excluding the pillar tips, creating a stiffness gradient above and below the silver pad or stiff island. The meandering interconnect is also encapsulated in PI as shown in Figure 2.1D.

2.1.1 Pillar Structures

The three-dimensional structures investigated in this thesis are primarily pillars due to the simplicity of design and similarity to VIAs in traditional printed circuit boards (PCBs). Several example pillar designs were fabricated and shown in Figure 2.2. Of the four pillar types fabricated, a majority of the focus is on the circular hollow pillar, Figure 2.2A, with some experimentation also involving the tapered full pillar Figure 2.2B.

The capabilities of the pillars to act as vias in multilayer prints, external connection points, or even targeted skin contact locations is shown in Figure 2.3. The pillar can extend through the PDMS layer and can be tuned to the thickness of the top layer of PDMS. Micropillars of this design have been fabricated up to several millimeters of height, so the PDMS thickness could reach the millimeter range. The pillars could even function as needle arrays protruding up to several millimeters from the surface of the PDMS as they can be hollow.

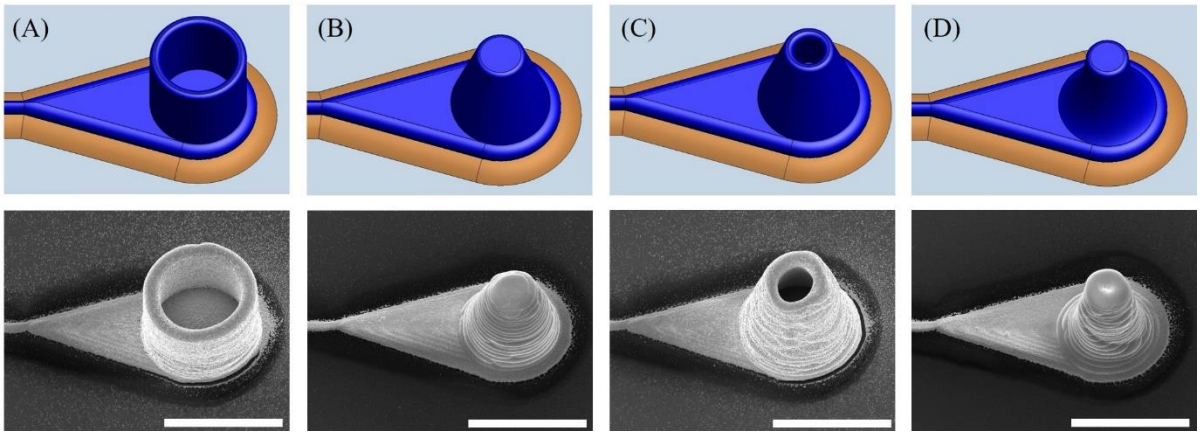

Figure 2.2: Renderings and SEMs of fabricated pillar geometries. Example geometries include the (A) circular hollow pillar, (B) tapered full pillar, (C) tapered hollow pillar, and (D) the curved full pillar. Scale bars are 200 μm.

The pillars also can function as an external connection point for either external wiring, or even as a mounting location for electrical components. Solder or silver paste can facilitate the connection as shown in Figure 2.3B. Additionally, early designs of the ECG patch discussed in Chapter 6 included the exposed pillar tips as targeted skin contact points for intimate skin to electrode contact as shown in Figure 2.3C. However, the small electrode contact area in this design resulted in unacceptably high contact impedance. Despite this drawback, interesting applications such as targeted drug delivery via microneedle arrays on a stretchable patch remain a possibility with this pillar design.[49]

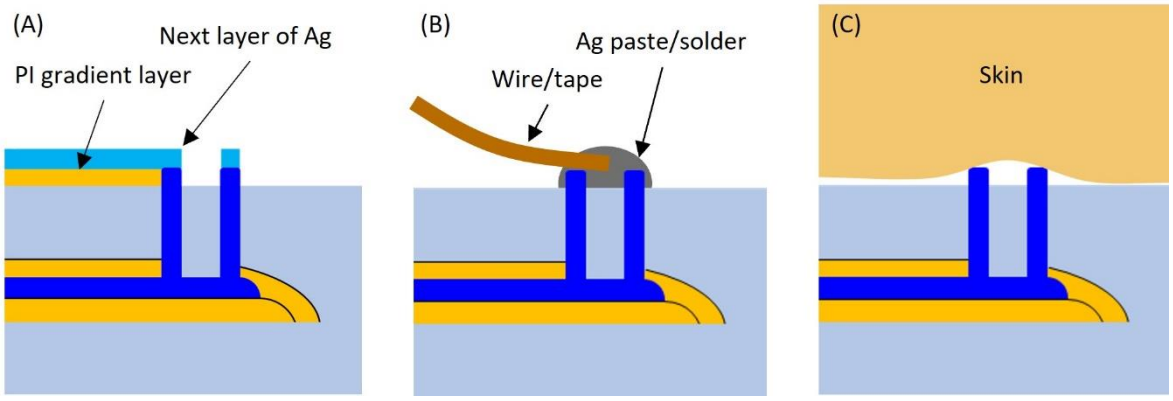

Figure 2.3: Exposed pillar tips designed as vias, external connections, and targeted skin contact. The exposed pillars can be (A) connectors for the next layer of circuit, (B) external connection points, and (C) targeted skin contact for an electrode or even micropillar for drug delivery.

To connect to the pillars on the next level shown in Figure 2.3A, another strain gradient layer of PI must first be printed. Ideally, the PI layer could be printed just to the edge of the pillar tip as shown in Figure 2.3A, but in practice this is difficult to control precisely without covering the exposed silver entirely. Instead, the PI can be printed just across the edge of the pillar to form a bridge between the PDMS, and the exposed pillar tips as shown in Figure 2.4. This bridge successfully suppresses the cracks that are observed at the transition from the pillar tip to the PDMS when the PI did not fully bridge between the PDMS and pillar tip. Then, the silver interconnect can be printed on the PI layer and then around the remaining rim of exposed silver to create the electrical connection.

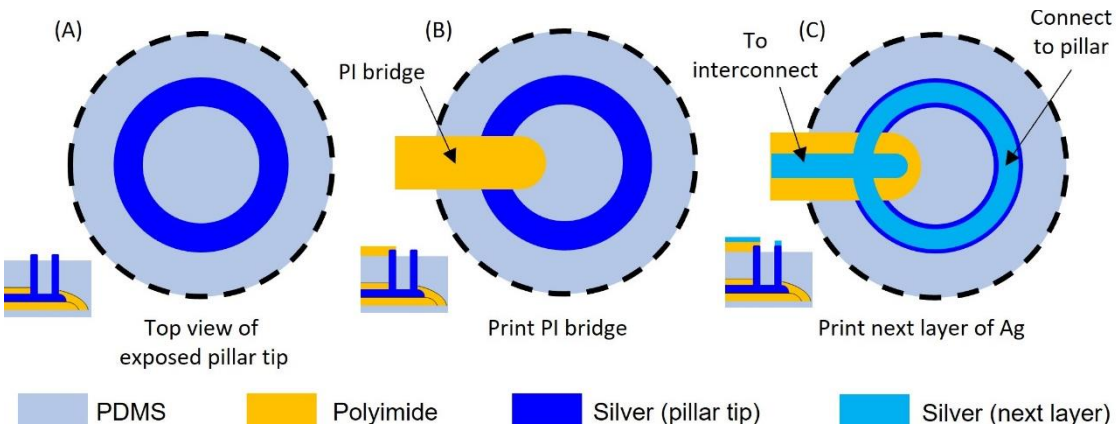

Figure 2.4: Detail of printed connection to the exposed pillar tip. (A) The top view of the exposed pillar after the top layer of PDMS has been deposited. (B) The PI layer is printed to form a bridge between the PDMS and the exposed Ag pillar tip. (C) The interconnect of Ag can then be printed across the PI bridge (represented by the lighter blue color) to make a crack free connection to the exposed pillar tip.

2.2 Fabrication of 3D Multi-Material Electrical Interconnect

The development of the fabrication process to solve challenges associated with integrating multiple materials and realizing functional 3D features with electrical interconnects is a focus of this work. The process used in several sections of this thesis are therefore different, and the experiments, analysis, designs, and conclusions that incrementally update the process are discussed in later sections. The culmination of those fundamental investigations is shown in

Figure 2.5, and illustrates the final fabrication process utilized in this work. The process shown in Figure 2.5 is utilized in the mechanical characterization of the stretchable interconnects and the electrocardiogram (ECG) demonstration in Chapter 6. This process represents a significant contribution to both additive manufacturing and stretchable electronics fields by providing a solution to printing and processing 3D multi-material electrical interconnects directly on an elastomer substrate.

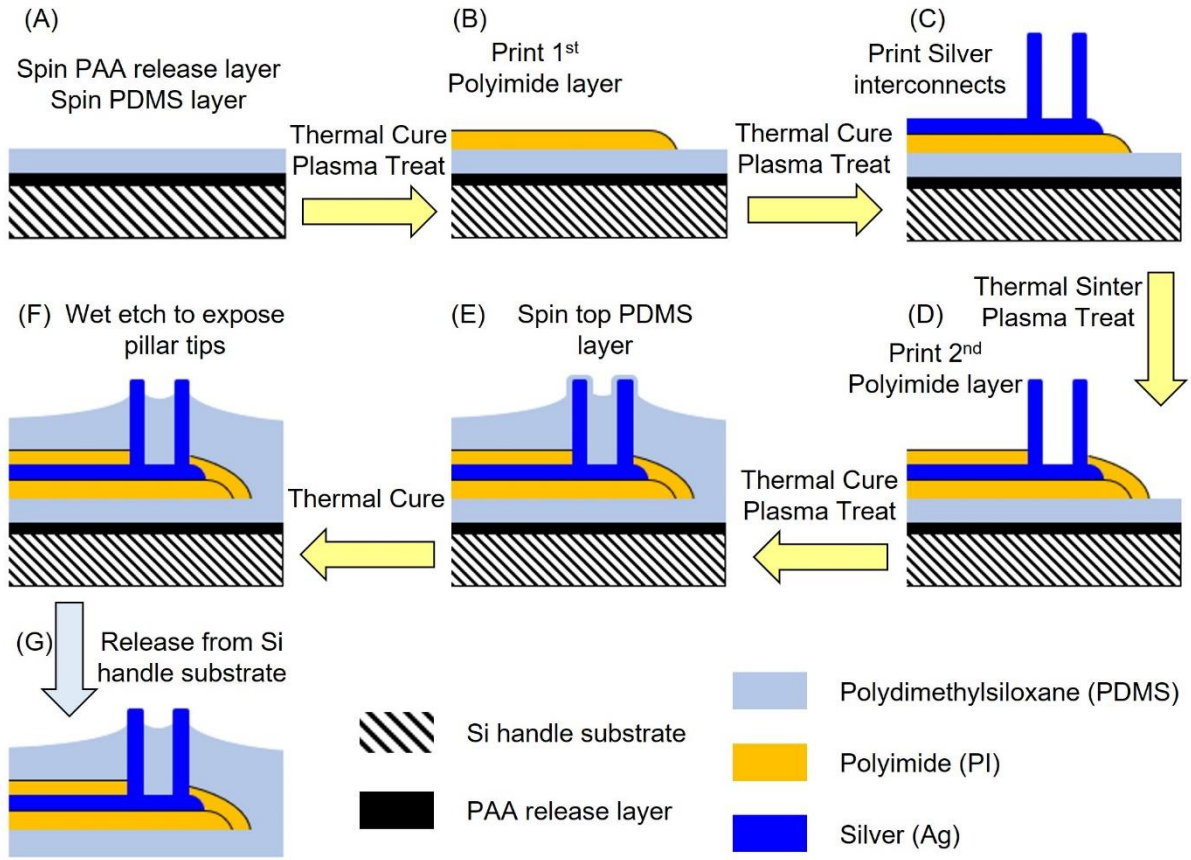

Figure 2.5: Schematic of fabrication process steps for 3D printed stretchable interconnects. The fabrication process starts with (A) spinning PAA release layer and first layer of PDMS onto a bare silicon wafer. (B) The first layer of PI is directly printed onto PDMS substrate. The PI is thermally cured and prepared with plasma treatment before the (C) Ag interconnects and pillars are printed in a layer-by-layer process on top of first PI layer. Ag is sintered and prepared with a plasma treatment before (D) the second PI layer is printed and cured. (E) The second layer of PDMS is spin cast to encapsulate everything and thermally cured. (F) Timed wet etch of PDMS to expose the pillar tips. (G) Release sample with saline soak.

2.2.1 Spin Casting Elastomer and Release Layer

The fabrication process starts by spin casting a polyacrylic acid (PAA) release layer on a four-inch silicon wafer (Figure 2.5A), which serves as a handling substrate, following a previously published recipe.[50] Polyacrylic acid sodium salt, 35% solution in water (18611-250, Polysciences Inc., Warrington, PA) is first diluted to 5% with DI water. The diluted solution is then divided into two containers, and one is adjusted to a pH of 2 using hydrochloric acid. The 5% acidic PAA is deposited on the wafer and spun at 600 rpm for 6 s followed by 2000 rpm for 30 s and a 15 min bake at 150 °C. The non-acidic 5% PAA layer is then spun at 600 rpm for 6 s followed by 2000 rpm for 30 s followed by a 2 min bake at 150 °C. The wafer is then immersed in 2 M $CaCl_2$ for 1 min, rinsed in DI water and dried, and finally baked for 2 min at 150 °C.

Following the PAA release layer, the PDMS elastomer is spin cast on top to a thickness of approximately 60 µm. The PDMS (Sylgard 184, Dow Corning Corporation, Midland, MI), is prepared by mixing the base (pre-polymer) and the curing agent (cross-linker) of the polymer at a 20:1 ratio by weight. The mixture is degassed for 30 min under vacuum to remove bubbles. The PDMS mixture was then spin-cast for 60 s at 500 rpm followed by 120 s at 1000 rpm. The spin-cast recipe is the same for the bottom layer and the top layer of PDMS. The ideal curing conditions from the supplier of the PDMS are between 25 °C to 150 °C. However, the polyimide and silver both require higher temperatures to fully cure/sinter, so the first layer of PDMS is cured under the same thermal and environmental conditions as the subsequent layers to minimize any changes in the PDMS during the next thermal treatments. The thermal treatments are discussed in more detail in Section 2.2.3, and the curing/sintering conditions are shown by Figure 2.7B. For single layer electronics, the top layer of PDMS can be cured under supplier specified conditions.

2.2.2 3D printing Multi-Material Interconnect with Aerosol Jet

The aerosol jet printing (AJP) technique can print fine features down to 10 μm in polymer, metal, and ceramic materials with 3D features to enable complex device architectures on a micron scale in a digitized workflow. The AJP (AJ 300 Optomec Inc, Albuquerque, NM) is used to print the PI and Ag interconnects in this work and the schematic of the AJP process is shown in Figure 2.6. The AJP has an ultrasonic (Figure 2.6A) and a pneumatic (Figure 2.6B) atomizer that convert the ink into aerosol droplets which is carried to the print head with a carrier gas (N_2). The ultrasonic atomizer is for inks with viscosities like water in the range of 1 - 10 cPs, while the pneumatic atomizer can atomize inks with higher viscosities of 10 - 1000 cPs. The pneumatic atomizer requires a higher carrier gas flow rate to atomize the ink, so the extra flow is removed with exhaust flow to enable comparable ink deposition rates to the ultrasonic atomizer. Regardless of the atomization method, the aerosol laden gas is then focused at the print nozzle (Figure 2.6C) using a separate sheath gas, again N_2, capable of focusing the aerosol stream to print features down to 10 μm[40,51] depending upon the nozzle size and gas flow parameters. The nozzle size, carrier gas flow rate, sheath gas flow rate, and atomization method all affect the feature size and quality, and several reports have investigated influence of each of the parameters.[34,52-54]

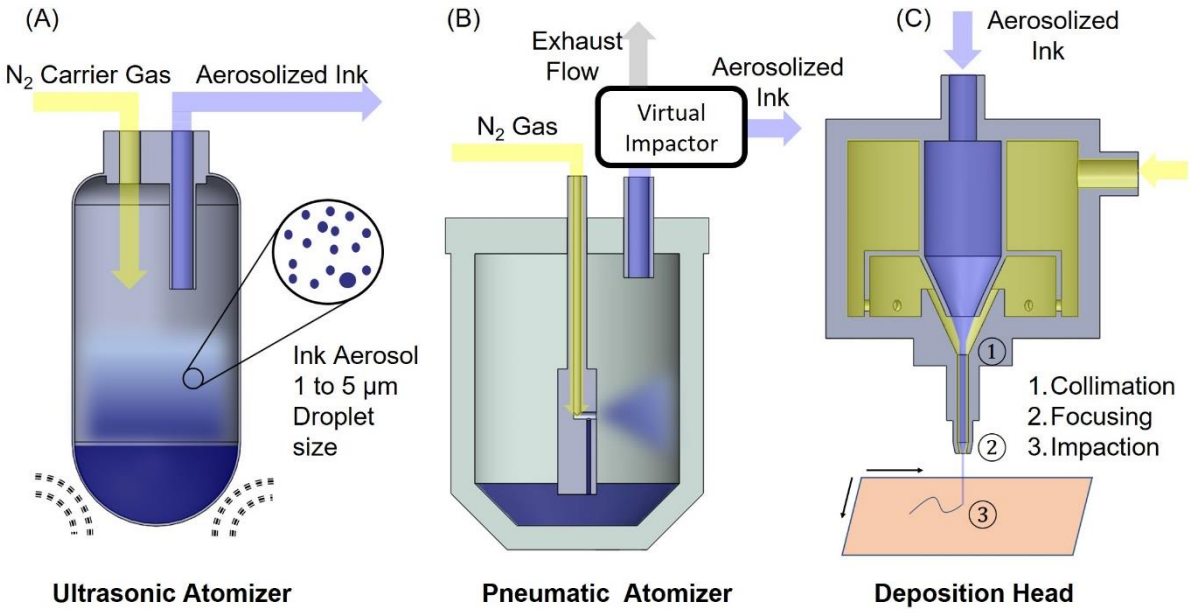

Figure 2.6: Schematic of the aerosol jet printing process. (A) The ultrasonic atomizer uses ultrasonic energy to atomize the ink and create an aerosol, while (B) the pneumatic atomizer uses gas flow to atomize the ink. The virtual impactor has two functions of 1. exhausting the extra N_2 gas needed to aerosolize the ink, and 2. only allowing a narrow band of aerosol particle sizes to pass through without impacting the side walls. (C) The ink is then carried to the deposition head where it is collimated with a sheath gas, and focused at the nozzle exit before depositing on the substrate.

The polyimide ink is prepared by mixing the PI precursor resin (PI 2574, HD MircroSystems, Parlin, NJ) with N-Methyl-2-pyrrolidone (NMP) at a ratio of 2:3 by volume. Prior to printing, the PDMS substrate is exposed to plasma treatment (PDC-001-HP, Harrick Plasma, Ithaca, NY) at 45 W for 2 min. Plasma surface modification of the PDMS (and PI when printing the Ag interconnects) increases the wettability and is also shown to increase the adhesion to the printed layers.[55,56] Without the plasma treatment, the PI ink 'beads up' and does not form a continuous line. To print the first layer of PI (Figure 2.5B), the pneumatic atomizer was used along with a 300 µm diameter nozzle, a sheath gas flow rate of 80-100 sccm, an atomization flow rate of 850 sccm, an exhaust flow rate of 800-820 sccm resulting in a carrier gas flow rate of 30-50 sccm. The specific printing parameters are determined by measuring lines printed on a test substrate (plasma treated glass slides). The printing parameters are

modified until the line width is 80-100 μm as measured using the alignment camera of the AJP. The AJ platen was heated to 60 °C and the printing speed was set at 1 mm/s. The PI layer was then cured according to the conditions in Figure 2.7B which is the same for each thermal cure/sinter except for the last PDMS layer.

Silver nanoparticle ink (Metalon JS-A426, NovaCentrix, Austin, TX) was utilized as the conductive ink in the interconnect shown in Figure 2.5C. This ink has been developed for aerosol jet printing in the ultrasonic atomizer and requires no additional preparation other than mixing before putting in the ultrasonic ink vial. A 150 μm diameter nozzle is used to print line ~30 μm, a sheath gas flow rate of 45-50 sccm, and a carrier gas flow rate of 25-30 sccm with a platen temperature of 60 °C and an ink bath temperature of 25 °C. For the interconnects the process speed is set to 1 mm/s, while for the layer-by-layer printing of the pillars, a slower 0.6-0.7 mm/s process speed is used which increases the layer height decreasing the time to build the pillars. The specific carrier gas flow rate, sheath gas flow rate, and process speed for the pillars is determined by printing test pillars consisting of 50 layers starting at nominal printing parameters on a test substrate (usually a glass slide). Depending on the height of the test pillars, printing parameters are changed to achieve 150 μm tall test pillars as measured with the alignment camera on the AJP. Following the procedure for the printed PI layer, prior to printing the surface is prepared with the same plasma conditions, and after printing the silver is sintered in the same thermal conditions as previous layers.

Following the sintering of the silver layer, the second layer of PI is printed on top to fully encapsulate the silver as shown in Figure 2.5D. The printing parameters for the second PI layer are the same as the first layer of PI. The design in this work includes three side by side printed traces of PI for the second layer as shown in Figure 2.1D, which allows the second layer of PI to contact the PDMS substrate, the first layer of PI, and encapsulate the silver layer. It also

tapers off the thickness of the embedded interconnect to reduce stress concentrations at the edge.

After the curing step of the PI, the sample undergoes another plasma treatment before PDMS is spin cast on top of the entire wafer (Figure 2.5E). Residual PDMS on the tips of the pillars (Figure 2.5F) can be removed with a 10 s soak in Dynasolve (Versum Materials, Tempe, AZ), followed by 5 min soak in an isopropyl alcohol bath, and a drying step at 100 °C for 30 min. The sample can now be released by placing the wafer in a saltwater solution (0.5 M NaCl) for approximately 1 hr (Figure 2.5G) to remove the PAA layer. Prior to release, the samples are cut to shape using a 2-axis cutting tool (Curio™, Silhouette America, Lindon, UT, USA) with a 30-degree blade. Higher angle blades were experimented with, but the cut would not be clean and bunch up. At this stage, a fully embedded interconnect with external connections is finished and can be connected to as shown in Figure 2.3B. To fabricate multi-layered circuits, steps from Figure 2.5B-F can be repeated with the pillars acting as vias between layers, and the in-plane connection to the pillar can be made using the design shown in Figure 2.4.

2.2.3 Thermal process steps

Each material that is used in this work requires a thermal processing step, and the ideal or manufacturer recommended processing conditions (temperature, time) are different for each material. Not only are the processing conditions different, but the ideal process conditions for one material may exceed the maximum temperature limit for another material. This is the case for the stretchable electronics platform described in this work, where the ideal sintering temperature for the silver is 300 to 500 °C, and the curing temperature for the PI ink is 200 °C, which are both higher than the 150 °C maximum temperature limit of the PDMS.[57-59]

This creates a problem when the goal is to print and sinter/cure the nanoparticle silver and PI inks directly on the stretchable PDMS substrate. Several sections of this thesis are focused on developing a processing condition that is compatible with each material in the system and still results in robust electrical and mechanical performance during the fabrication steps, testing, and use. Chapter 3 focuses on the PDMS mechanical performance after exposure to high temperatures in vacuum to investigate if thermal processing using vacuum is a viable method to reach the higher temperatures required to sinter nanoparticle silver ink and cure PI ink. Chapter 4 investigates delamination between the interconnect layers during processing and introduces a drying step to mitigate the popcorning effect where absorbed water is vaporized during thermal processing and can cause internal pressure to drive crack growth and delamination. Chapter 5 focuses on the process conditions that affect the electrical conductivity of the silver interconnect and avoid cracks that can form during solvent evaporation phase of the thermal processing of the nanoparticle ink printed on soft substrates. The culmination of the work detailed in those sections is the final process used in this work shown in Figure 2.7B, which represents several improvements from the first process that was investigated and shown in Figure 2.7A.

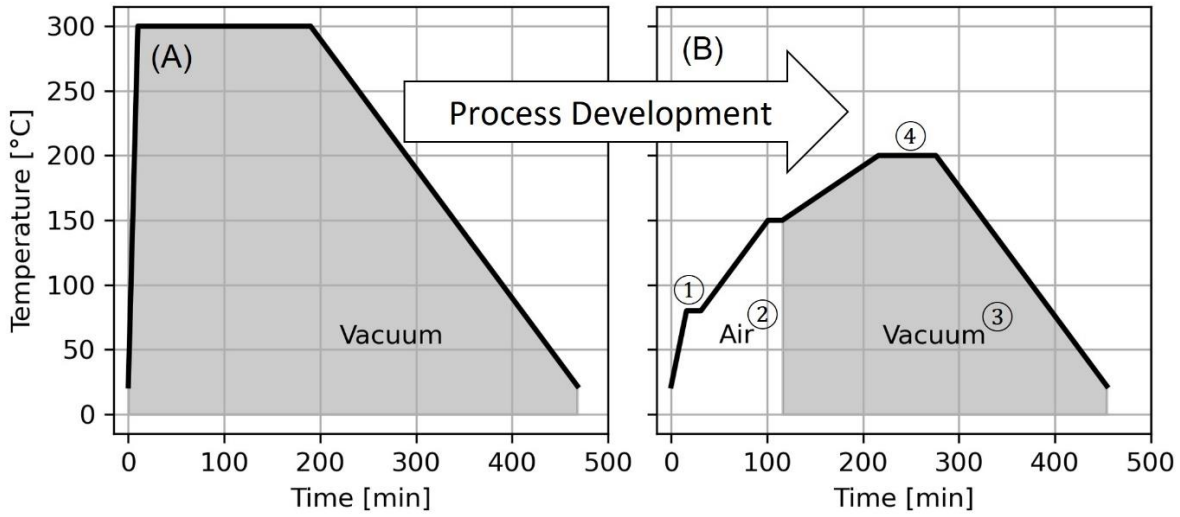

Figure 2.7: Process development to integrate multiple materials in 3D stretchable interconnect. (A) The first process investigated that was compatible with each material. (B) Final process in this work that mitigated delamination and cracking while increasing electrical conductivity and mechanical strength. Changes include 1. a drying step to solve delamination problem, 2. conduct drying step under air to reduce film stress and promote the removal of ligands and binders in ink, 3. conduct sinter step under vacuum to increase conductivity, cure polyimide, and 4. reducing maximum temperature to preserve PDMS mechanical strain to failure.

2.3 Conclusions

Integrating functional 3D structures on a stretchable electronics platform including multiple materials can unlock rich feature possibilities, but fabrication challenges associated with multi-material printing on a thin stretchable substrate are numerous. These challenges include incompatible ideal processing temperatures, delamination between printed layers, and integrating 3D features. The following chapters address these challenges in detail and provide the conclusions leading to the fabrication process to achieve the 3D meandering interconnect design. In this chapter, a process solution utilizing an aerosol jet printer to realize a multi-material stretchable interconnect with stiffness gradients forming strain islands, and 3D pillars for use as external contact and VIAs in a multi-layered printed circuit is detailed.

Chapter 3

Mechanical Response of PDMS After High Temperature Exposure

PDMS exhibits a high stretchability (strain to failure >100%) and that is well above that of the skin (maximum elastic strain ~15%), with similar stiffness (elastic modulus of PDMS is ~1 MPa while skin is several hundred kPa) making it an ideal candidate for wearables biomonitoring devices.[60,61] In addition to having similar mechanical properties, PDMS is a popular substrate material for stretchable electronic devices due to its biocompatibility, sub-micron resolution, leak-proof packaging, and resistance to weathering.[60,62-65] The properties of as-made PDMS can be further modulated by changing the mixing ratios of its base elastomer to curing agent from 5:1 to 33:1.[66]

When PDMS is used as a substrate material for the stretchable interconnects described in the previous chapter, temperatures as high as 200 to 300 °C are experienced during the fabrication processes to sinter the silver nanoparticle ink or to cure the PI ink. The ability to subject PDMS polymer to the process temperatures used in microelectronics manufacturing for flip-chip bonding, or solder-ball attach would allow a significant flexibility in the types of electronic circuits and functionalities that can be integrated with devices that use PDMS as the substrate material.[35] A study of the evolution of volatile materials from PDMS showed that the degradation at high temperatures is due to the formation of Si-O bonds (oxidation), and is accelerated in the presence of heat and oxygen.[67,68]

The mechanical properties of PDMS have been measured in literature for different cure times, thicknesses, and strain rates,[69-73] including a comparison for various mixing ratios of PDMS base to curing agent.[70,71] These studies show that the elastic modulus of PDMS increases with a decrease in mixing ratio, a decrease in thickness, and an increase in the strain rate.[69-71] These reports of PDMS properties, however, have been limited to the low strain elastic region.[72,73] The behavior of PDMS films in tension exhibit incompressible hyperelastic material behavior and models such as those proposed by Ogden or Mooney-Rivlin can be used to fit all the experimental data from low strain all the way to failure.[74-77]

The focus of this chapter is to subject the PDMS to thermal conditions required for sintering the silver nanoparticle ink, curing the polyimide, and other common microelectronics packaging techniques. The hypothesis is that the mechanical properties of the PDMS can be retained if the oxygen in the environment is removed (i.e., by pulling a vacuum) during exposure to high temperature. The aim is to gain a comprehensive understanding of the changes in stiffness and strain-to-failure (two properties most important to strechable electronics applications) of PDMS films with a 20:1 mixing ratio exposed to high temperatures at low vacuum (1 Torr). Hyperelastic models are fit to the data for future use in engineering process conditions for the fabrication of stretchable circuits directly on PDMS substrates.

Contents of this chapter have been published as:
Tansel, D. Z., Brenneman, J., Fedder, G. K., & Panat, R. (2020). Mechanical characterization of polydimethylsiloxane (PDMS) exposed to thermal histories up to 300 °C in a vacuum environment. *Journal of Micromechanics and Microengineering, 30*(6). doi:10.1088/1361-6439/ab82f4

3.1 Experimental

The PDMS samples (Sylgard 184, Dow Corning Corporation, Midland, MI), are fabricated by mixing the base (pre-polymer) and the curing agent (cross-linker) of the polymer at ratios of 20:1 and 10:1 by weight. The PDMS and release layer are spin cast according to the recipe

in section 2.2.1. The thermal process conditions are varied as a part of this chapter, and so they do not follow the final process shown in Figure 2.7B. All PDMS specimens are initially cured at 100 °C in atmospheric conditions using rapid heating and cooling determined by the on/off conditions of the hotplate. Some of the specimens are then thermally treated in a nitrogen vented vacuum chamber for 1 hr at 1 Torr for temperatures of 100 °C, 200 °C, and 300 °C using the same rapid heating and cooling rates. Table 3.1 details the different conditions applied to the PDMS samples. Four samples are tested for each condition shown in Table 3.1. Specimens are cut to shape using a benchtop cutter (Curio™, Silhouette America, Lindon, UT, USA) and released in saline overnight to dissolve the PAA. Thicknesses of all the PDMS samples are measured with a surface profilometer (Dektak 3, Bruker Corporation, Billerica, MA). An aperture card is used to handle each specimen to ensure smooth insertion into the tensile testing machine as shown in Figure 3.1B. After the sample is clamped in the tensile testing machine, the sides of the aperture card are cut and removed to isolate the thin PDMS sample between the clamps.

Table 3.1: Summary of thermal process conditions for PDMS study.

Condition	Mix Ratio	Initial cure Temperature	Post Cure Temperature in 1 Torr Vacuum
A	10:1	100 °C	-
B	20:1	100 °C	-
C	20:1	100 °C	100 °C
D	20:1	100 °C	200 °C
E	20:1	100 °C	300 °C

3.2 PDMS Characterization

PDMS specimens are cut to a modified type-C specimen shape described in ASTM D412[78] with dimensions as shown in Figure 3.1. The dog-bone shape has a thin test section at the center, 10 mm long and 6 mm wide, with wider sections at the ends. The specimen is clamped in the tensile testing machine (Instron Model 5943, Norwood, MA) at the wide ends and stretched at a rate of 1 mm/min. Note that the dog-bone geometry helps minimize the effects from the clamps while maintaining uniform local stress and strain in the test section. The tensile test measures the displacement of the clamps throughout the test and the force required to extend the sample.

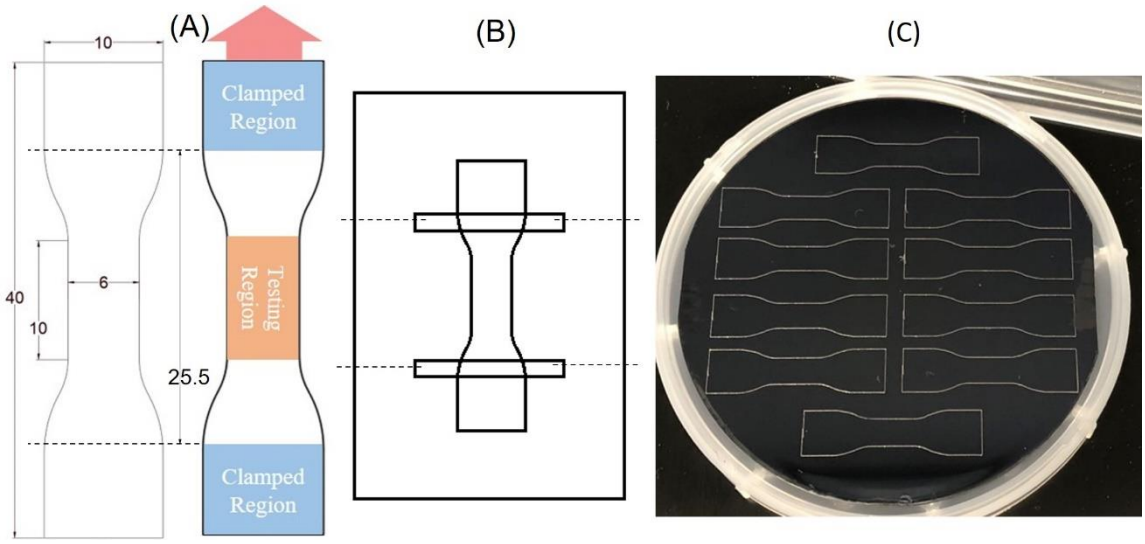

Figure 3.1: Dogbone sample design for PDMS tensile test. (A) The dimensions of the dogbone shape with the test region and clamping region highlighted with units in millimeters. (B) Aperture card schematic to support and hold sample prior to insertion in the tensile tester. Cuts are made with scissors along the dotted lines after clamping in tensile tester and middle section of the aperture card is removed to release the sample. (C) An optical image of 10 cut samples on handle substrate before release.

The clamp displacement measured by the tensile tester needs to be scaled to the displacement of the test section, L_t, shown in the orange region of Figure 3.1A. To measure the local engineering strain in the test section, benchmarks in this region are manually tracked

via image analysis (InfiniProbe TS-160, Infinity Photo Optical Co., Boulder CO, USA). The local test section strain is then analyzed for every 1 mm of clamp displacement. The global strain uses the clamp displacement, ΔL_{global}, as the change in length of the test section, ΔL_t, because it is a measured output of the Instron, but it needs to be scaled to find the local engineering strain, ε_{eng}. The relationship between the local and global strains is shown in Figure 3.2, which relates the local engineering strain, ε_{eng}, to the global engineering strain, $\varepsilon_{\text{global}}$, via a correlation factor, m, as

$$\varepsilon_{\text{eng}} = m\,\varepsilon_{\text{global}} = m\,\frac{\Delta L_{global}}{L_t} = \frac{\Delta L_t}{\Delta L_{global}}\frac{\Delta L_{global}}{L_t} \qquad 3.1$$

From Figure 3.2, the relation between ε_{eng} and $\varepsilon_{\text{global}}$ is linear with a correction factor, m = 0.458. A finite element analysis (ANSYS Inc, Canonsburg, PA) of the test geometry shown in Figure 3.1A, assuming a hyperelastic behavior of the PDMS, yields a correction factor m_{FEA} of 0.48, which is within 5 % of that extracted from Figure 3.2. The measured correction factor of 0.458 is thus used to calculate the engineering strain for all data using the modified type-C dogbone geometry.

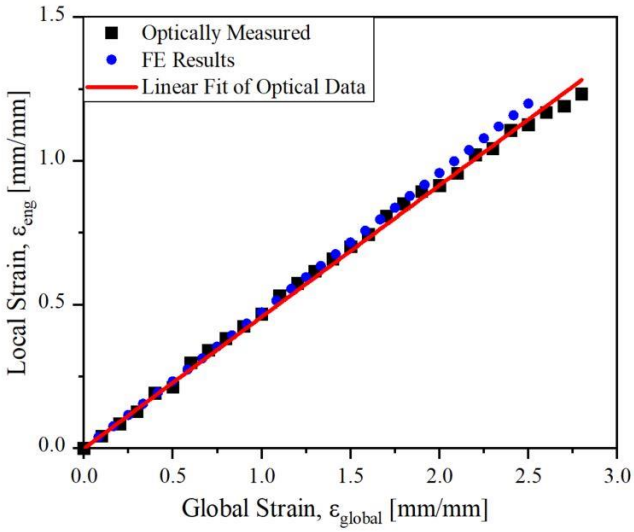

Figure 3.2: Local strain measured optically vs global strain measured from clamp displacement. The linear fit yields a correction factor of 0.458 for the modified type-C dogbone sample shape.

The elastic modulus of PDMS is often reported in literature, though there is no specification in ASTM D412 for how to calculate the modulus for rubber-like materials. Specifying the linear region is thus determined by the tester, and there are reported elastic modulus values using data from 1 % strain[69] all the way up to 40 % strain[72] and even 100 % strain[70] as the linear region. In the present work, we extract the elastic modulus as the slope of the linear fit of the data up to 5 % engineering strain and the corresponding engineering stress and then compare that to the instantaneous elastic modulus from the fit of Ogden's hyperelastic model. A series of snapshots of the Condition-B PDMS sample being stretched in the Instron testing machine is shown in Figure 3.3.

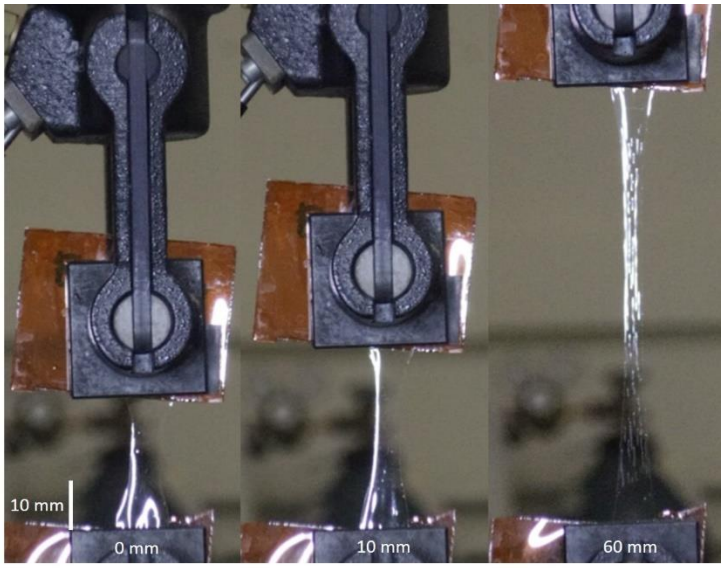

Figure 3.3: Sample of PDMS stretched at 0 mm, 10 mm, and 60 mm extension. The PDMS shown is a condition-B sample.

3.3 Results and Discussion

The load-displacement data and the engineering stress-strain plots for the films after applying the correction factor as defined in Equation 3.1 are shown in Figure 3.4A-E. Hyperelastic behavior and average failure strain higher than 100 % is evident for all the conditions tested, and the maximum engineering stress is a few MPa at failure. The box plots

of the strain-to-failure and elastic modulus of the PDMS samples are plotted in Figure 3.4F-G. For 10:1 PDMS (Condition-A), the elastic modulus of 1.815 MPa is similar to that reported in literature.[69,79,80] For the 20:1 PDMS, however, the as-fabricated films (Condition-B) showed a softer film behavior with a modulus of 0.627 MPa, or 65 % reduction compared to Condition-A. The average strain to failure for the samples with Condition-B was about 300 %, showing high stretchability. As the films were subjected to thermal histories of 100 °C, 200 °C, and 300 °C, however, the average strain-to-failure reduced to 250 %, 224 %, and 106 %, respectively, while the elastic modulus initially increased to 0.81 MPa, but then decreased to 0.71 MPa and 0.62 MPa, respectively. In fact, a 1 hr extra time at 100 °C (Condition-B vs Condition-C) increases the stiffness by 30%. However, the stiffness values are still less than that for as-deposited PDMS with a 10:1 mixing ratio. One-way analysis of varaince (ANOVA) was performed for the resulting failure strain and elastic modulus and showed a significant difference between the populations of Conditions B through E for the failure strain (F (3, 12) = 35.1, $p = 3.2 \times 10^{-6}$) and a lack of statistically significant difference for the elastic moduli (F (3, 12) = 1.97, $p = 0.17$).

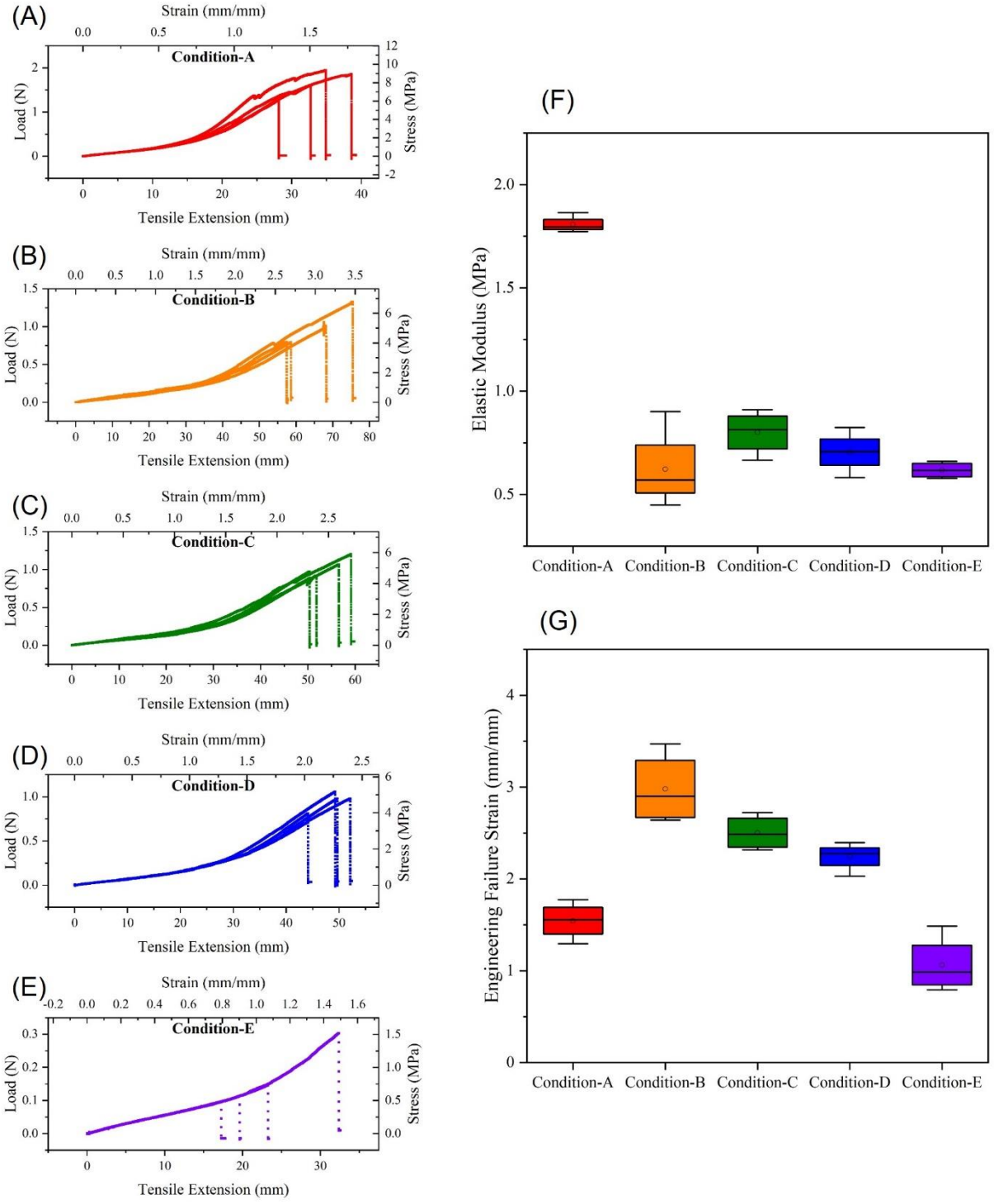

Figure 3.4: Tensile test data for PDMS samples exposed to different thermal conditions. (A-E) Display raw data from tensile tester given as load vs extension (i.e. clamp displacement) with a sample size n = 4 for each condition. Engineering stress vs engineering strain included on separate axis. (F) Compares the elastic modulus, and (G) compares the failure strain for each condition tested.

Hyperelastic material models[74,81] are used to describe the behavior of rubber like materials, such as PDMS films, over the entire stress/strain curve. The Ogden model utilizes a linear combination of the principle stretches λ_1, λ_2, and λ_3, instead of the stretch invariants used by other hyperelastic models to simplify the mathematical operations needed to utilize the material models. Equations in this section follow the original development from Ogden, and starts with the strain energy function U defined as[74]

$$U(\lambda_1, \lambda_2, \lambda_3) = \sum_{r=1}^{N} \frac{\mu_r}{\alpha_r} (\lambda_1^{\alpha_r} + \lambda_2^{\alpha_r} + \lambda_3^{\alpha_r} - 3) \qquad 3.2$$

where μ_r and α_r are material fitting parameters. For incompressible solids, the principal stresses can be written as

$$\sigma_i = \lambda_i \frac{\partial U}{\partial \lambda_i} - p \qquad (i = 1,2,3) \qquad 3.3$$

Where p is an arbitrary hydrostatic pressure. For uniaxial tension tests, the principal stretch, $\lambda_1 = \lambda$, is along the direction of stretching, and the corresponding principal stress $\sigma_1 = \sigma$, and the other principal stresses $\sigma_2 = \sigma_3 = 0$. Additionally, the remaining principal stretches $\lambda_2 = \lambda_3 = \lambda^{-1/2}$ due to the incompressibility constraint, the arbitrary hydrostatic pressure is eliminated, and the following relationship is found by evaluating Equation 3.3 with 3.2.[74]

$$\sigma_{eng} = \frac{\sigma}{\lambda} = \sum_{r=1}^{N} \mu_r \left[\lambda^{\alpha_r - 1} - \lambda^{-(1+\frac{1}{2}\alpha_r)} \right] \qquad 3.4$$

Since the goal is to fit the Ogden hyperelastic material model to our force and displacement data, which is accompanied by initial sample geometric measurements, it is convenient to have a model which utilize the engineering stress and strain ($\sigma_{eng}, \varepsilon_{\text{eng}}$). The form of Equation 3.4 provides that convenience by noticing that the stretch $\lambda = 1 + \varepsilon_{\text{eng}}$. In addition, the instantaneous shear modulus is given by the Ogden model to be

$$G = \frac{1}{2}\sum_{r=1}^{N} \mu_r \, \alpha_r \qquad 3.5$$

and the Young's (elastic) modulus is

$$E = 2G(1 + \nu) \qquad 3.6$$

where ν is Poisson's ratio, assumed to be 0.5 since PDMS has been shown to behave as an incompressible material.[82]

Table 3.2 gives a summary of the values of modulus, failure strain, and the parameter fit with the Ogden model for all the conditions tested in this study. The Ogden model can be a sum of infinte terms, and first to third-order (N = 1 to 3) models are explored to describe the observed PDMS stress-strain behavior. The second-order Ogden model (N = 2) is chosen as there was a noticeable impact on the correlation coefficient (R^2) by increasing N from 1 to 2, but not from 2 to 3. Figure 3.5 shows the Ogden N = 2 fit for one set of samples, illustrating its suitability. To satisfy kinematic requirements of the strain energy function, a necessary and sufficient condition on the coefficients is that $\alpha_i \mu_i > 0$. Futhermore, it is common to require at least one set of coefficient pairs (α_i, μ_i) to be negative to capture characteristic behavior from other tests such as biaxial stress tests, and so the fit was performed holding the second coefficient pair (α_2, μ_2) to be negative for consistancy to previously reported data.[74,76]

Table 3.2: Fitting parameters each thermal condition and corresponding PDMS material properties. Shear modulus (G) elastic modulus (E), and R^2 are reported for the Ogden model, and the elastic modulus from the linear fit up to 5% strain is reported alongside for comparison.

	Elastic Modulus	Failure Strain	Ogden Constants					Ogden Model	
	E	ε_{eng}	α_1	α_2	μ_1	μ_2	R^2	G	E
Condition	[MPa]	[%]	[−]	[−]	[MPa]	[MPa]	[−]	[MPa]	[MPa]
A	1.82	155	5.030	0.000	0.214	0.000	0.9945	0.538	1.614
B	0.63	298	4.140	−1.259	0.065	−0.172	0.9988	0.244	0.732
C	0.81	250	4.541	−2.915	0.060	−0.122	0.9974	0.314	0.943
D	0.71	225	4.806	−1.131	0.053	−0.294	0.9997	0.292	0.877
E	0.62	106	5.888	−0.038	0.015	−12.441	0.9992	0.278	0.835

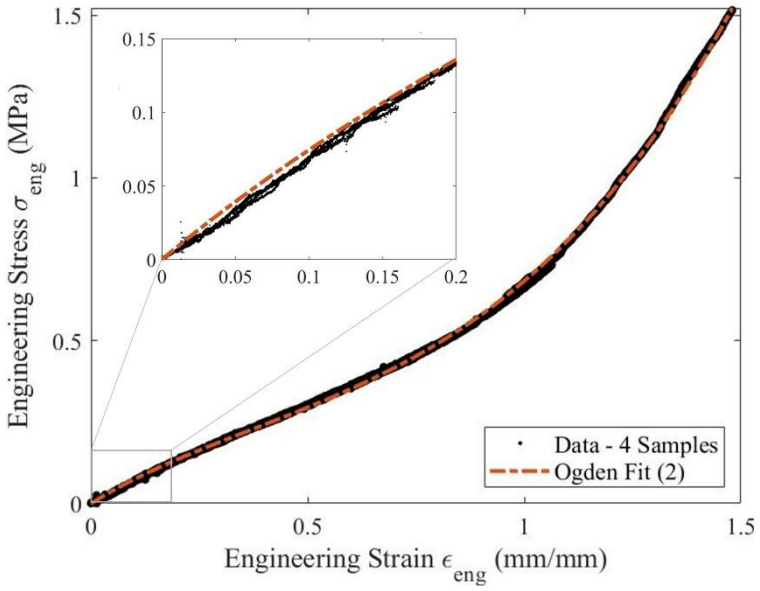

Figure 3.5: Ogden Fit (N = 2) to test data consisting of 4 samples of 20:1 PDMS cured at 300 °C.

While the Ogden model coefficients are largely phenomenological with no direct physical interpretation, there has been recent work linking the coefficients to physical parameters,[81] one of which has been linked to the aging, or further crosslinking of the PDMS.[76] A consistent trend appears in each of the coefficients for the 20:1 samples cured under vacuum, with the α coefficients increasing and the μ coefficients decreasing with increasing thermal exposure. In addition, the coefficient pairs of the Ogden model conveniently sum together to give the instantaneous shear modulus as shown in Equation 3.5. The elastic modulus resulting from the Ogden model matches the same decreasing trend found from the linear fit from the first 5 % of strain. Hopf et al. suggest that crosslinking of the polymer chains is increased with aging and temperature, which is shown to increase the stiffness in PDMS.[76] However, the results summarized in Table 3.2 indicate a different trend, where increased exposure temperature softens the PDMS specimens. We speculate, then, that the dominating effect responsible for this trend is increased thermal decomposition of the PDMS rather than increased crosslinking when the material is exposed to higher temperatures in vacuum.

3.3.1 Additional Elastomer Substrates

Sylgard 184 PDMS is a widely used elastomer in stretchable electronics because of its desirable properties such as high strain to failure, low elastic modulus, optical clarity, and approved usage in implantable biomedical applications. There are, however, additional stretchable substrates that could be utilized. In particular, a stretchable substrate capable of withstanding the high temperatures required to sinter the silver without the need for a vacuum oven would be advantageous. A commercially available two-part formulation of silicone (MoldMax 60, Smooth-On, Macungie, PA) claims service temperatures up to 294 °C. To test if the stretchability is affected by higher temperature process conditions a collaborator from the Electrical and Computer Engineering department Derya Tansel performed tensile tests on the MoldMax 60 silicone when cured at room temperature in air at 24 hr, which is the recommended curing schedule from the manufacturer, cured in the hybrid cycle shown in Figure 2.7B for 3 cycles to simulate the same conditions during the stretchable interconnect fabrication, and in air to 200 °C for 1 hr. There was no significant difference in the strain to failure for the different curing conditions, and the average value was close to the reported 132 % strain to failure from the manufacture's data sheet.[83] This is comparable to the 106 % strain to failure of the Sylgard 184 PDMS when heated to 300 °C and would also function as a suitable replacement for stretchability. However, the red color of the MoldMax 60 is undesirable in skin wearable devices, and the lack of a commercially available etchant could make it difficult to expose the pillars and integrate them into a multi-layered device. Additional stretchable substrate formulations include Ecoflex (Ecoflex 00-31, Smooth-On, Macungie, PA), which boasts extremely high strain to failure of 900 % and low modulus of 70 kPa[84] or polyurethane formulations such as Baymedix (Baymedix FD103, Covestro, Leverkusen, Germany). The high strain to failure and low modulus of Ecoflex may prove to be better suited

in wearable devices compared to Sylgard 184, but more research is needed, especially to test if multi-layered devices can be achieved.

3.4 Conclusions

The results discussed in this chapter indicate that the 20:1 PDMS maintained suitable mechanical properties and hyperelastic behavior through high-temperature treatment, including maintaining significant film stretchability. There is, however, a decrease in desired mechanical performance as the post-cure heating temperature increases from 100 °C to 300 °C, and the failure strain decreases from 250 % to 106 %. Interestingly, the modulus decreases from 0.805 MPa to 0.621 MPa over the same increase in temperature which is beneficial for interfacing with other softer materials. The softening of the PDMS upon heating indicates that polymer chain degradation rather than crosslinking occurs at temperatures up to 300 °C. Decreasing the amount of cross-linker is shown to reduce the elastic modulus and increase the strain to failure. The stress-strain response of the films is represented by a second-order Ogden hyperelastic model useful for future investigations where material properties of 20:1 PDMS after exposure to high thermal treatment is required. This chapter demonstrates the suitability of the vacuum thermal treatment for the subsequent microelectronics fabrication processes in temperatures up to 300 °C as the hyperelasticity of PDMS is maintained and an acceptable reduction of the strain to failure is observed.

Chapter 4

Mitigating Interfacial Delamination in Electrical Interconnects

The design of the stretchable interconnects utilized in this thesis integrates heterogeneous materials such as metals, polymers, and elastomers, which results in interfaces prone to delamination under stress. Compounding adverse interactions occur at heterogeneous interfaces where mechanical stress is concentrated due to the elastic modulus mismatch between the materials precisely at the location where the weakest bonds in the system are often found. In addition to concentrating stress, heterogeneous interfaces generate stress during temperature changes due to thermal expansion mismatch in the materials. Additionally, printing the silver nanoparticle ink typically requires sintering the nanoparticles at high temperatures (150 to 300 °C) and introduces micropores where moisture can vaporize and generate internal pressure if completely encapsulated. Larger disparities in material properties present in stretchable electronics systems, and unique interfaces of printed metallic conductors are expected to accentuate the delamination problem currently observed in conventional rigid electronics.[85]

The investigation covered in this chapter is undertaken to understand delamination between polyimide layers that was observed during the processing of the prototype interconnects. The first aim is to utilize aerosol jet 3D printing of different interconnection geometries to identify the conditions under which delamination can occur. The second aim is

to obtain a mechanistic understanding of this problem by developing a non-linear parameterized fracture model to develop delamination mechanism maps and use this knowledge to provide design guidelines to avoid delamination. To verify the parameterized straight crack model and extend the applicability to meandered geometry, two finite element (FE) models are developed and compared against the nonlinear theoretical model.

Contents of this chapter have been published as:
Brenneman, J., Tansel, D. Z., Fedder, G. K., & Panat, R. (2021). Interfacial delamination and delamination mechanism maps for 3D printed flexible electrical interconnects. *Extreme Mechanics Letters*, 43. doi:10.1016/j.eml.2021.101199

4.1 Sample Fabrication

First, PDMS is spin-cast onto a silicon wafer having a polyacrylic acid (PAA) release layer following the procedure outlined in Chapter 2. The delamination study was a part of the process development, and so does not follow the exact same thermal treatments and interconnect design shown in Chapter 2. The polyimide (PI) layer is printed with three side-by-side patterns then cured in a vacuum chamber at 1 Torr for 3 hr at 300 °C with a rapid temperature ramp rate which deviates from the final process in this thesis but is consistent with the process determined to be compatible with PDMS discussed in Chapter 3. These curing/sintering process conditions are the same for each layer in this chapter and are illustrated by Figure 4.1A. Silver nanoparticle ink is then printed directly onto the cured PI layer utilizing the ultrasonic atomizer. After sintering the silver, another layer of PI precursor was printed on top of the silver to encapsulate the silver interconnects in PI. The top PI layer was then cured, under the same processing conditions as the bottom PI layer, to complete the sample fabrication. The PI thickness is controlled by the number of overlapping print passes. In total, 21 samples were fabricated, covering three different thicknesses of PI shown in Figure 4.1B, where the thickness is measured with a profilometer (Dektak 3, Bruker Corporation, Billerica, MA).

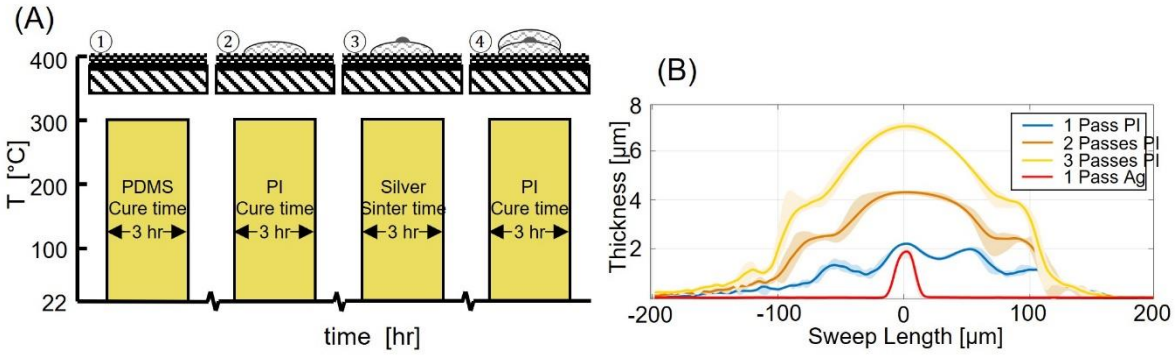

Figure 4.1: Thermal process schematic for delamination study with cross section profiles. (A) Sintering and curing profiles for each fabrication step 1) spinning PDMS and release layer onto silicon wafer followed by 2) printing of the base layer of PI, 3) printing of silver, and 4) printing of the top layer of PI. (D) Profilometer scan of a printed silver profile, and printed PI profiles with varied number of printing passes. The solid lines are the average of three scans at different locations along the trace, and the shaded envelope shows the minimum and maximum extent of the scans.

4.2 Delamination Observations

Figure 4.2 shows optical and SEM images of the polymer-polymer delamination observed. The delamination was observed between the bottom and the top PI layers, with the silver interconnect in-between. As shown in Figure 4.2C, the width of the silver interconnect line at the ends of the stretchable circuit was about 50 µm, while that at the center was 30 µm. We observed that the delamination happened only for the section of the circuit where the silver interconnect width was about 50 µm (created by 3 side-by-side passes of AJ printing) and not for a width of 30 µm (created by a single pass) as shown in Figure 4.2C. We note that optical images were taken of the samples between every process step (Figure 4.1B), and delamination was observed to occur during the cure of the final layer of PI, but only for samples with the thickest PI layers (i.e., with 3 printing passes). Of the 8 samples with the thickest top and bottom PI, a total of three samples showed delamination. For 13 other samples with thinner PI, we did not observe any delamination (see Figure 4.2A for a representative SEM image). We also observed that the surface of the silver interconnect (Figure 4.2B and inset images) shows

characteristic surface roughness due to sintered nanoparticles. This surface roughness allows for the additional surface area and mechanical ‘interlocking’ for the top layer of polyimide to bond to the silver. This improves the bond strength compared to the interface of the silver and bottom polyimide layer, which is smooth due to the nature of the cured polyimide. Figure 4.2B shows SEM images of the delamination, with insets showing high magnification images that clearly illustrate polymer-polymer delamination with the silver interconnect delaminating along with the top polyimide layer. The measured profiles of the PI thicknesses are shown in Figure 4.1D and were used in the models described later.

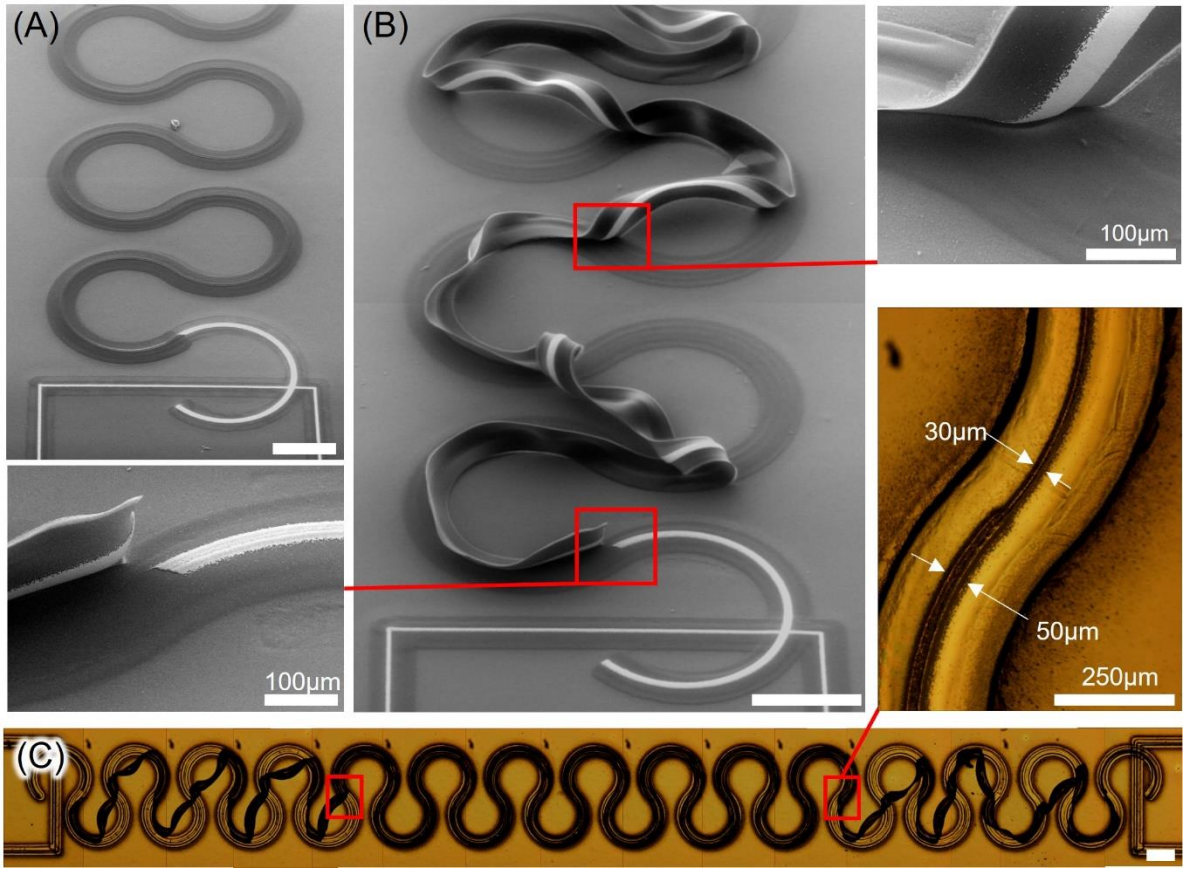

Figure 4.2: Delamination between PI layers of prototype stretchable interconnect. (A) SEM image of bonded sample with a single print pass of PI on the top and bottom layers encapsulating the silver. (B) SEM image of delaminated sample with three printing passes of PI comprising the top and bottom layers encapsulating the silver. (C) An optical image, taken after final cure, of the entire printed interconnect. The delamination region is limited to the two ends where the silver trace is 50 µm vs 30 µm wide after the final cure. Inset: transition region from wide to thin silver, image taken before final cure. All scale bars are 500 µm unless otherwise noted.

4.3 Analytical Models of Delamination

The polymer-polymer delamination shown in Figure 4.2 is observed to occur only for thick PI layers and only at the locations where the metallic interconnects were widest (e.g. Figure 4.2C) during thermal processing to 300 °C of the second layer of polyimide. These observations generated two hypotheses: 1) the delamination was caused by thermal expansion differences between different materials, and 2) the delamination was caused by internal pressure generated by absorbed moisture vaporizing at high temperatures. To test these hypotheses, two parametric analytical models are developed. A thermoelastic model follows a previously reported model, while a vapor pressure model is adapted from the blister model for this application. While the vapor pressure is determined to be the driving factor for delamination, the thermoelastic model and results are detailed here as it may be relevant for polyimide layers that are thicker than those used in the design discussed in this thesis. Finite element models are also developed to validate the vapor pressure model and extend the results to meandering geometries.

Identical material properties are used in analyzing both the analytical and FE models and are discussed below. For thermoset polymers such as PI, a linear decrease of modulus with increasing temperature up to the glass transition temperature has been reported. Therefore, the elastic modulus of PI at 300 °C is linearly extrapolated from the datasheet and taken to be 1.72 GPa; with a glass transition temperature of 320 °C.[86] The PI moisture uptake is taken to be 2 % from the manufacturer data sheet.[87] Poisson ratio for PI is taken to be 0.34.[86] The bond strength for two PI layers, both cured at 300 °C, was measured to be 30 N/m using T-peel test.[88] The T-peel test generally includes plastic energy dissipation, in addition to the interfacial fracture. Although the blister delamination modeled in this work is expected to include some plastic deformation, we take the critical energy release rate, G_c, to be 30 J/m^2, which is expected to be the upper bound of the fracture energy. For silver, the Poisson ratio is taken to be 0.37 and an

elastic modulus of sintered silver film is taken to be 2.3 GPa, and yield stress of 45 MPa from earlier work.[36] For silver and PI, the tangent modulus is taken to be about 10 % of the elastic modulus.

4.3.1 Thermoelastic Strain Energy Model for Delamination

The first hypothesis tested is that the cooling of the multi-layered interconnect from its curing temperature (300 °C) to room temperature would induce a significant elastic stress due to the thermal mismatch of the multiple materials present in the stack. This stress can then be relieved when the crack propagates, and the top layer of PI and silver delaminates (Figure 4.2B). The strain energy available in the top PI layer and silver layer per delaminated area is then the energy release rate, *G*. A thermoelastic strain model is used to determine the strain energy available in the silver and top PI layer assuming a zero-stress state at the curing temperature, thin film assumption, and no external forces following the derivation from the reference.[89] The delamination region and the multilayer stack modeled is shown in Figure 4.3A.

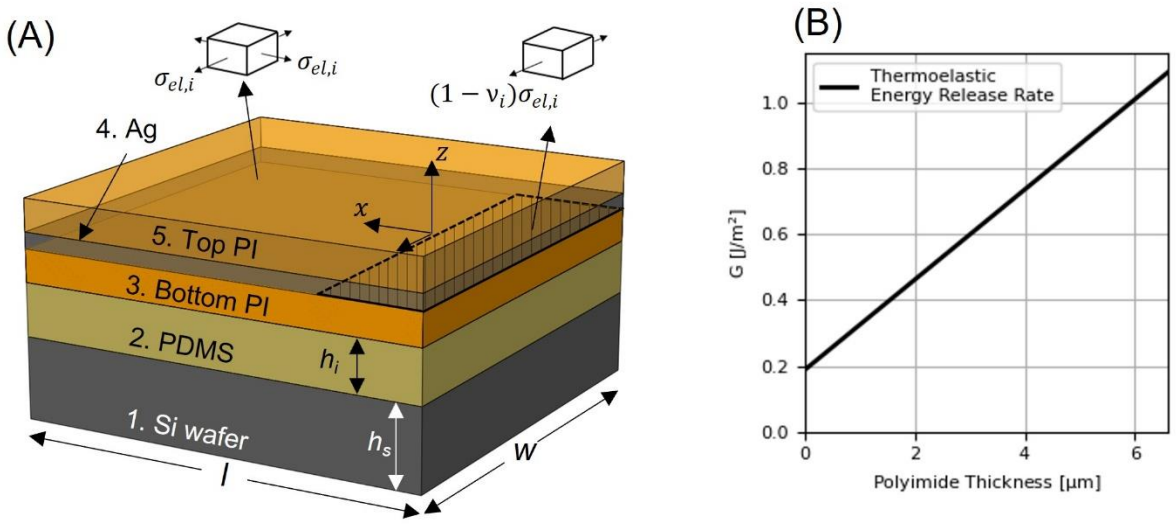

Figure 4.3: Thermoelastic strain energy delamination model and results. (A) The model set up is shown with the delaminated region shown by the hatched area between the silver and the bottom PI layer. The stress state far ahead and behind the delamination front are shown. (B) The results of the thermoelastic energy release rate model with increasing polyimide thickness.

The model is a 1D model where the thicknesses of the layers, h_i, are varied between the different layers, the width of the layers, *w*, is normalized to the width of the interconnect, and the length of the system, *l*, is normalized to unity.[90] The crack is assumed to extend the length of *w*. When completely bonded, layers sustain an equi-biaxial elastic strain, $\varepsilon_{el,i}$, due to the thermal expansion mismatch with the Si handle substrate. The corresponding biaxial stress magnitude is $\sigma_{el,i}$, and the stress state far ahead of the delamination front and behind the delamination front is shown in Figure 4.3A. The strain in the delaminated region is relaxed in the *x* direction, but parallel to the crack it remains pinned by the remaining bonded section. The Si handle substrate is much thicker than the other layers in the stack ($h_s \gg h_i$) and dominates the thermal contraction during cooling. Then, the elastic strain in each layer, which supplies the energy to drive delamination, is given by the difference with the thermal expansion to the Si substrate as

$$\varepsilon_{el,i} = (\alpha_s - \alpha_i)\Delta T \tag{4.1}$$

where α_i is the coefficient of thermal expansion of the i^{th} layer, and ΔT is the change in temperature. The energy release rate, *G*, is then the sum of the change in elastic strain energy of the silver layer and top PI layer.

$$G = \frac{\partial U_{Ag}^{el}}{\partial A_d} + \frac{\partial U_{PI}^{el}}{\partial A_d} \tag{4.2}$$

where the change in elastic strain energy of individual layers, U_i^{el}, is

$$\frac{\partial U_i^{el}}{\partial A_d} = \frac{(1+v_i)}{2(1-v_i)} E_i \varepsilon_{el,i}^2 h_i \tag{4.3}$$

where A_d is the delaminated area of the layer, E_i is the elastic modulus, v_i is the Poisson's ratio, and h_i is the height of the i^{th} layer.[89]

The available energy per unit area for delamination increases linearly with increasing PI thickness because of h_i in Equation 4.3 and is 0.5 to 1.0 J/m^2 for PI having thicknesses of 2 μm and 6 μm, respectively as shown in Figure 4.3B. These values are over an order of magnitude lower than that required for delamination (30 J/m^2).[88] In a system where the layer thicknesses are significantly larger, the thermoelastic strain energy will play a significant role in delamination. In the current case, however, the available strain energy is unable to drive the experimentally observed delamination. We thus reject the hypothesis that the delamination observed in Figure 4.2 is driven by thermoelastic strain energy in the flexible electronic interconnect system.

4.3.2 Vapor Driven Delamination Model

A second hypothesis stating that the delamination shown in Figure 4.2 is driven by vapor pressure in the system is tested with a nonlinear vapor driven delamination model. The silver conductor is encapsulated by polyimide (PI) which has remarkable usable temperature range, and high strength and stiffness.[4,18,91-94] However, polyimide is extremely hygroscopic, and the adhesion strength has been shown to depend on the moisture loading of the polyimide.[95] While typical temperatures experienced during device operation are low, high temperatures are required during device fabrication to cure polyimide or sinter metallic inks. The moisture absorbed in the polymer can diffuse to voids or defects in the material, and at high temperature can vaporize and result in internal pressure to drive delamination or facture at material interfaces. Such interfacial delamination has been observed in thermoset polymers in the fabrication and assembly of electronic systems and is called the 'pop-corning' effect.[85,96,97] Several models have been reported to describe the delamination initiated at a circular edge (blister test),[98,99] along a straight surface,[100-102] and to measure the interfacial adhesion.[103]

Additionally, models have investigated the role of vapor availability, and one model parametrically describes the steam driven delamination at high temperatures by considering a circular blister geometry at a point defect.[85,96,104] Given the importance of vapor availability to drive crack growth, blister deformation must be accurately captured for all geometric configurations typical of printed electronics. Nonlinear models are required to capture both the effects from the tensile stress developed in very thin membranes and the bending stress developed in thicker films. However, a model linking vapor availability in a straight crack (e.g., those caused by long interconnects that act as crack initiators) with the capability to model both thin membrane-like films and thicker plate-like films has not been previously reported to my knowledge.

The vapor driven delamination model development begins by considering the cross section of the meandering interconnects as shown in Figure 4.4A. The inset in Figure 4.4A shows the top PI layer, the silver interconnect, and the bottom PI layer. Note that PI is a hygroscopic material capable of absorbing 2% of its mass in water under at room temperature and humidity, and the moisture absorption into the bottom PI layer is expected to be governed by Fick's law.[105] For the length scales relevant in this investigation (e.g., Figure 4.1D), the absorbed moisture in the PI layers can reach saturation at room temperature and humidity within an hour.[96,106] This time scale is within the range of wait times in our fabrication process shown in Figure 4.1C. Then, at high temperatures occurring during the curing stage, the moisture from the bottom PI layer directly under the crack surface is assumed to diffuse to the silver interface (i.e., initial crack). Note that at the boundary between the silver interconnect and PI, there are voids due to the surface porosity of sintered nanoparticles, which allow the moisture to vaporize and create pressure at the boundary as shown in Figure 4.4A.

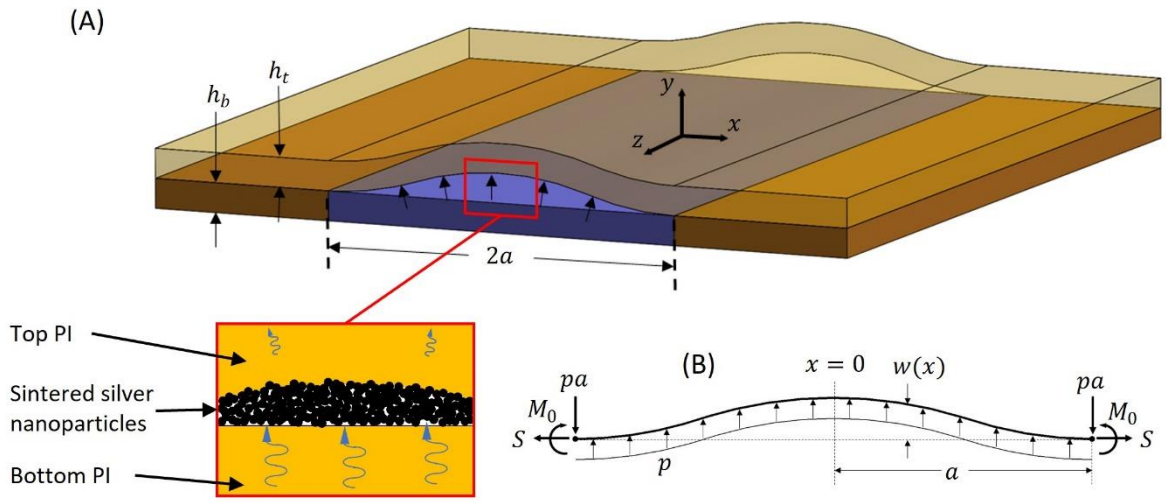

Figure 4.4: Vapor driven delamination model schematic and free body diagram. (A) The polyimide layers are assumed to be saturated with water. The moisture is then able to diffuse to the boundary with silver and vaporize in the voids between the rough surface of the sintered silver and the polyimide as shown in the inset image. The area directly below the delaminated surface (purple region in A) is the volume of saturated polyimide available to deliver water to the crack void area. The crack is straight and long in the z direction as shown in (A). The corresponding free body diagram for the vapor driven model is shown in (B) for the deformed state of the top layer of polyimide.

The initial crack surface is assumed to be between the silver and the bottom PI layer. This assumption comes from the experimental observation of the crack interface observed in Figure 4.2B and this sets up the model shown in Figure 4.4B where the geometry in the *z* direction is assumed to be straight and normalized to unit length. Because the PI at both sides of the silver along the *x* direction are fixed, a tensile reaction develops as the thin film is stretched during the bending deformation. On one extreme of the dimensional combinations in our experiments, a wide silver trace (50 μm) with a thin PI layer (2 μm) results in a membrane like behavior where the tensile stresses dominate. On the other extreme, a narrower silver trace (30 μm) with a thick PI layer (6 μm), results in a case where the bending stresses are most significant. To consider both the membrane stresses and the bending stresses, nonlinear von-Kármán plate theory is utilized to have a unified model for the entire parameter set. Models of this type do not have exact solutions, but Timoshenko[107] provides a near exact solution for this one-

dimensional case that requires only a simple root finding numerical method. The membrane stress, σ_m, bending stress, σ_b, and transverse deflection, w, are

$$\sigma_m = \frac{S}{h} = \frac{Du^2}{a^2 h} \tag{4.4}$$

$$\sigma_b = \frac{-12Dy}{h^3}\frac{d^2w}{dx^2} = \frac{-12a^2py}{h^3u^2}\left(u\,\mathrm{csch}(u)\cosh\left(\frac{ux}{a}\right) - 1\right) \tag{4.5}$$

$$w = \frac{pa^2(a^2 - x^2)}{2Du^2} - \frac{pa^4}{Du^3\tanh u}\left(1 - \frac{\cosh\frac{ux}{a}}{\cosh u}\right) \tag{4.6}$$

where p is the vapor pressure, a is the half crack length, h is the thickness of the plate, y is the distance from the plate centerline, x is the distance from the blister center, D is the flexural rigidity of the plate, and S is the developed tensile reaction force. The second term in Equation 4.6 describes the contribution of membrane stresses. The first term of the transverse deflection in Equation 4.6 is similar to the beam theory result with the addition of the simplifying term, u, described as

$$u^2 = \frac{Sa^2}{D} \tag{4.7}$$

This term links the flexural rigidity to the developed tensile stress and is dependent on the geometry, pressure applied, and material properties being modeled. The solution for the u term is found by applying fixed boundary conditions at both end points in the *x* direction. Therefore, the extension of the film by the tensile reaction force *S* in plane strain is equal to the difference between the length of the deformed curve and the initial crack length 2*a* which is

$$a\varepsilon_m = \frac{Sh^2a}{12D} = \frac{1}{2}\int_0^a \left(\frac{dw}{dx}\right)^2 dx \tag{4.8}$$

where ε_m is the strain due to membrane stress. This expression now relates the bending deflection of the plate, to the extension or strain of the neutral plane due to membrane stress. After substituting Equation 4.6 into Equation 4.8 and performing the differentiation and integration, Equation 4.8 can be rearranged into the following relationship.

$$\frac{D^2h^2}{p^2a^8} = -\frac{9}{u^7\tanh u} - \frac{3}{u^6\sinh^2 u} + \frac{12}{u^8} + \frac{2}{u^6} \tag{4.9}$$

For a given pressure, material, and geometry, *u* can now be found. While Equation 4.9 gives an analytical relationship for *u*, numerical methods such as a root finding method must be used to solve for *u* in order to get the stresses (Equation 4.4 and 4.5) and the deflection Equation 4.6.

The contributions from the membrane and bending stress (Equation 4.4 and 4.5) in the delaminating plate are both normal in the same direction and can simply be added together to find the total stress on a differential element. The strain energy density w^{el} for uniaxial normal stress is then

$$w^{el} = \int_0^{\varepsilon} \sigma\, d\varepsilon = \int_0^{\varepsilon} \frac{E}{(1-\nu^2)}\varepsilon\, d\varepsilon = \frac{E\varepsilon^2}{2(1-\nu^2)} = \frac{h^3}{24D}\sigma^2 \tag{4.10}$$

The strain energy, U^{el}, can now be found by integrating the strain energy density over the entire volume and including both the membrane and bending stress.

$$\begin{aligned} U^{el} &= \frac{h^3}{12D}\int_{\frac{-h}{2}}^{\frac{h}{2}}\int_0^a (\sigma_m + \sigma_b)^2\, dxdy \\ &= \frac{Dh^2u^4}{12a^3} + \frac{a^5p^2(u^2\operatorname{csch}^2 u + u\coth u - 2)}{2Du^4} \end{aligned} \tag{4.11}$$

Note that the symmetry of the stress states around $x = 0$ is used to make the limits of the integral 0 to a, which simplifies the expression and introduces a factor of 2 to Equation 4.11. The energy release rate, also known as crack extension force, is

$$G = \frac{1}{2}\left(\frac{dU^{el}}{da}\right)_p \qquad 4.12$$

where U^{el} is given by Equation 4.11. Equation 4.12 can be numerically solved using the finite difference method but does not have an exact solution, because u is dependent upon a. The derivative in Equation 4.12 may be taken at constant pressure or constant displacement resulting in equivalent energy release rate determinations (with the exception of the sign) when the change in crack length is small, but the constant pressure condition is most easily implemented in this case because p appears explicitly in Equation 4.11.

In vapor pressure driven delamination, the absorbed water is diffused from the bottom layer of polymer to the boundary with the silver and evaporated into the micro voids at high temperature during the final cure step. The ideal gas law can be used to relate the developed pressure and volume, *V*, of the void given the temperature, *T*, and available water molecules.

$$pV = n_a RT \qquad 4.13$$

$R \approx 8.314$ J·K^{-1}mol^{-1} is the ideal gas constant. The total number of absorbed water molecules available, n_a, to fill the void is assumed to be contained in the bottom layer of polymer directly under the crack area, which is shown in Figure 4.4A as the purple region. The total number of absorbed water molecules available can then be described by geometric terms

$$n_a = 2ah_b\left(\frac{\rho_{poly} wt\%}{M_{molH_2O}}\right) \qquad 4.14$$

where $h_b$is the bottom polymer thickness, ρ_{poly} is the density of the polymer, $wt\%$ is the weight percentage of water absorbed (2% for the polyimide used in this analysis), and M_{molH_2O}

is the molar mass of water. Vapor pressure will reach saturated steam pressure, $p_{sat}(T)$, if there is enough water present. However, if the deflection of the blister is large, the void volume may grow large enough where there is not enough water absorbed in the polymer to reach saturated steam pressure (i.e., $p_{sat}V > n_aRT$). This region is called the vapor starved region, and in this case the pressure will be less than p_{sat} and will depend on the void volume and moisture content under the blister. The void volume of the blister is found by integrating the deflection of the polyimide (Equation 4.6) across the crack length.

$$V = 2\int_0^a w\,dx = \frac{2a^5p(u^2 - 3u\coth u + 3)}{3Du^4} \tag{4.15}$$

Combining Equation 4.15 with Equation 4.13 and solving for *p,* the pressure in the vapor starved region is

$$p_{vs} = \sqrt{\frac{3Du^4n_aRT}{a^4(u^2 - 3u\coth u + 3)}} \tag{4.16}$$

The vapor starved pressure, p_{vs}, is a function of u, which in turn is a function of pressure and must be found numerically; again, implemented with a root finding method. The saturated vapor pressure, on the other hand, is simply a function of temperature and can be found in steam tables. The internal blister pressure is found for both the saturated and vapor starved conditions:

$$p = \begin{Bmatrix} p_{sat} & \text{if } p_{sat}V \le n_aRT \\ p_{vs} & \text{if } p_{sat}V > n_aRT \end{Bmatrix} \tag{4.17}$$

Modification of vapor driven model for serpentine geometry

The model in the previous section assumes that the interconnect is straight, i.e., has an infinite radius of curvature (Figure 4.4A). The geometry of the interconnect in our experiments,

however, is serpentine (Figure 4.2). This geometry is incorporated into our model by considering the difference in energy release rate separately on the inner side of the interconnect (G_i) vs the outer side of the interconnect (G_o). For curved interconnects, the total strain energy contribution to the numerator of Equation 4.12 increases by a factor of $2\pi r$, due to the out-of-plane dimension being axisymmetric instead of Cartesian (i.e., normalized to unity), with r being the radius of curvature. The differential crack growth area (the denominator of Equation 4.12), changes from $2da$ to $4\pi(r-a)da$ for the crack face on the inner edge of the serpentine, and $4\pi(r+a)da$ for the crack face on the outer edge of the serpentine. Inserting these values into Equation 4.12, an estimation of the differences between the inner and outer crack extension forces are:

$$G_i = \frac{2\pi r}{4\pi(r-a)}\left(\frac{dU^{el}}{da}\right)_p = \frac{r}{(r-a)}G$$
$$G_o = \frac{2\pi r}{4\pi(r+a)}\left(\frac{dU^{el}}{da}\right)_p = \frac{r}{(r+a)}G \qquad 4.18$$

4.4 Model Prediction and Comparison with Experiments

Figure 4.5 maps the energy release rate, *G*, as predicted by the analytical model as a function of two critical dimensions of the problem. The first dimension is the PI thickness, which in this case is set equal for both the top and bottom layers. The second dimension is the initial crack length, 2*a*, which is the width of the silver interconnect lines. The black isolines in Figure 4.5A represent constant thickness and constant crack length. The crack length and PI thickness isolines are then plotted in Figure 4.5B and Figure 4.5C, respectively.

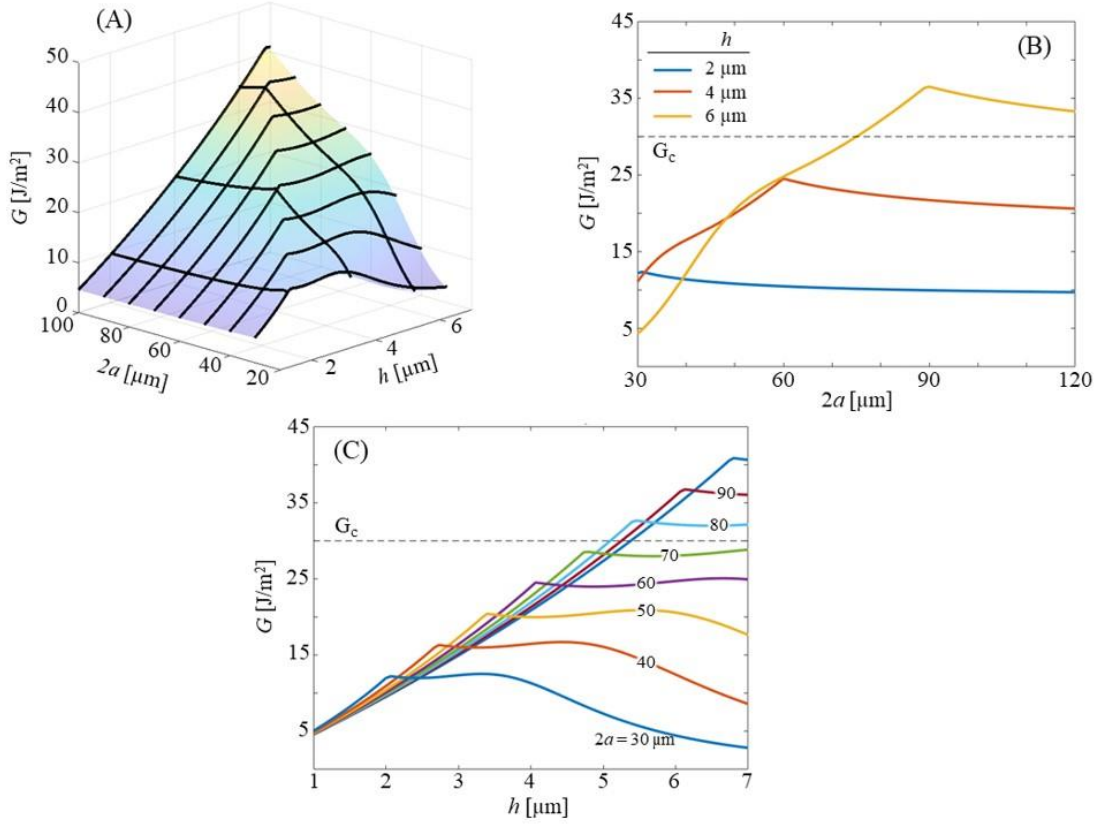

Figure 4.5: Energy release rate vs crack length, and PI layer thickness. (A) The surface plot shows the mapping of the energy release rate varying both the crack length, in this case 2a which is initially the silver width, and the PI layer thickness, where the top layer and bottom layer are the same thickness matching our test samples. (B) Holding the PI layer thickness constant, three curves are shown from the surface plot matching the thickness of the PI in test samples. (C) Holding the crack length constant, the effect of continuously increasing PI layer thickness is shown for various crack lengths, 2a.

Figure 4.5B shows the energy release rate increasing with initial crack length for both the 4 μm and 6 μm-thick PI. From Figure 4.5B, it is interesting to note that only the 6 μm-thick PI sample crosses the critical energy release threshold at a 76 μm crack length, signaling the onset of delamination. This result is consistent with the experimental observation that only samples with thicker PI (6 μm thick) delaminate during the curing of the top layer of PI. In experiments, the samples with a PI thickness of 2 μm and 4 μm did not show any delamination. This strong match between the model and experiments provides confidence regarding the hypothesis of the delamination mechanism. We note, however, that the delamination threshold is reached at an

initial crack length of 76 μm, which is higher than the 50 μm maximum silver width observed in experiments (Figure 4.2C). The model shows that the energy release rate for an initial crack length of 50 μm is 20.5 J/m^2. This minor difference between our experimental observations and the model can be attributed to PI thickness variation not captured in model, material property variations from reported values at the specific temperature, the additional thermoelastic strain, and moisture loading of the PI layer which effects both the vapor available and the interfacial toughness between the PI layers. The trend predicted in Figure 4.5, however, is consistent with the observed experimental delamination represented in Figure 4.2.

In Figure 4.5B, the energy release rate reaches a limit and starts decreasing at crack lengths of 59 μm and 88 μm for the 4 μm and 6 μm-thick PI films, respectively. The energy release rate then flattens and converges to a value as the crack length increases. This limit is the onset of vapor starvation described by Equation 4.17, where there is no longer enough moisture to maintain the saturated steam pressure. Reducing the available moisture is then a critical step in reducing the likelihood of delamination by limiting the energy release rate in the vapor starved region. This can be achieved by several methods such as incorporation of a drying step prior to the final high temperature cure, utilizing a polymer encapsulant with a lower moisture update, or by reducing the thickness of the bottom polymer layer.

Vapor starvation occurs at a smaller crack length for thinner layers of PI, as shown in Figure 4.5B, for two reasons. First, there is less moisture available for a given crack length, because the bottom layer of PI is thinner and therefore has less total moisture absorbed. Second, the deformation for thinner top PI layer (small h) at the same pressure is larger, creating a larger void for the vapor to fill at the same crack length. This is exemplified by the 2 μm-thick PI, where it becomes vapor starved at 30 μm and converges to a lower energy release rate of

approximately 10 J/m. Therefore, the top and bottom PI layer thicknesses have different effects on the developed energy release rate and can be investigated independently.

Figure 4.6 shows the effect of independently varying the bottom and top PI thicknesses on the energy release rate. The surface map in Figure 4.6A shows the energy release rates for two different crack lengths of 60 μm and 80 μm, where the top and bottom PI thicknesses are varied from 1 μm to 10 μm. Both surfaces indicate two distinct regions: the vapor starved region and the vapor rich or saturated region. The vapor rich region is wavy with a larger energy release rate and has no dependence on the bottom layer of PI, except to form the boundary where it becomes vapor starved. This is shown in Figure 4.6C where the top PI layer thickness h_t is held constant, and three curves for different bottom PI thicknesses h_b overlap until reaching the vapor starvation region. Then, once the vapor starvation region is reached, the energy release rate slowly decreases and converges to a value which is determined largely by the bottom layer of PI. This is shown in Figure 4.6D more clearly, where the bottom PI layer thickness is held constant in the three different graphs. The energy release rate in the vapor starved region is nearly independent of the top layer of PI as the curves converge to a single value independent of crack size and top PI thickness. Furthermore, the magnitude of the converged energy release rate in the vapor starved region is only dependent on the thickness of the bottom layer of PI. Thus, the energy release rate is determined by the available moisture to fill the voids and can be limited to a maximum value - independent of crack size - if the moisture loading can be reduced in the bottom layer of PI to the point of vapor starvation.

Figure 4.6B represents a delamination mechanism design map linking the three geometric parameters of silver interconnect width, top PI thickness, and bottom PI thickness to the likelihood of delamination of any of those combinations. This delamination map is created from the isolines in Figure 4.6A where the surface intersects with the critical energy release

rate, signifying the onset of delamination. Additional isolines of critical energy release rate for different crack lengths are plotted in Figure 4.6B to complete the map. The area filled in with blue represents conditions where delamination is likely to initiate for crack lengths or silver widths of 60 μm. Design guidelines to reduce the energy release rate can be extracted from this mapping and include: 1) reducing the bottom PI thickness to reduce the moisture available, 2) increasing the top PI thickness to increase the mechanical stiffness of the system which results in less strain energy for a given pressure, and 3) printing smaller silver interconnect widths to reduce the initial crack length.

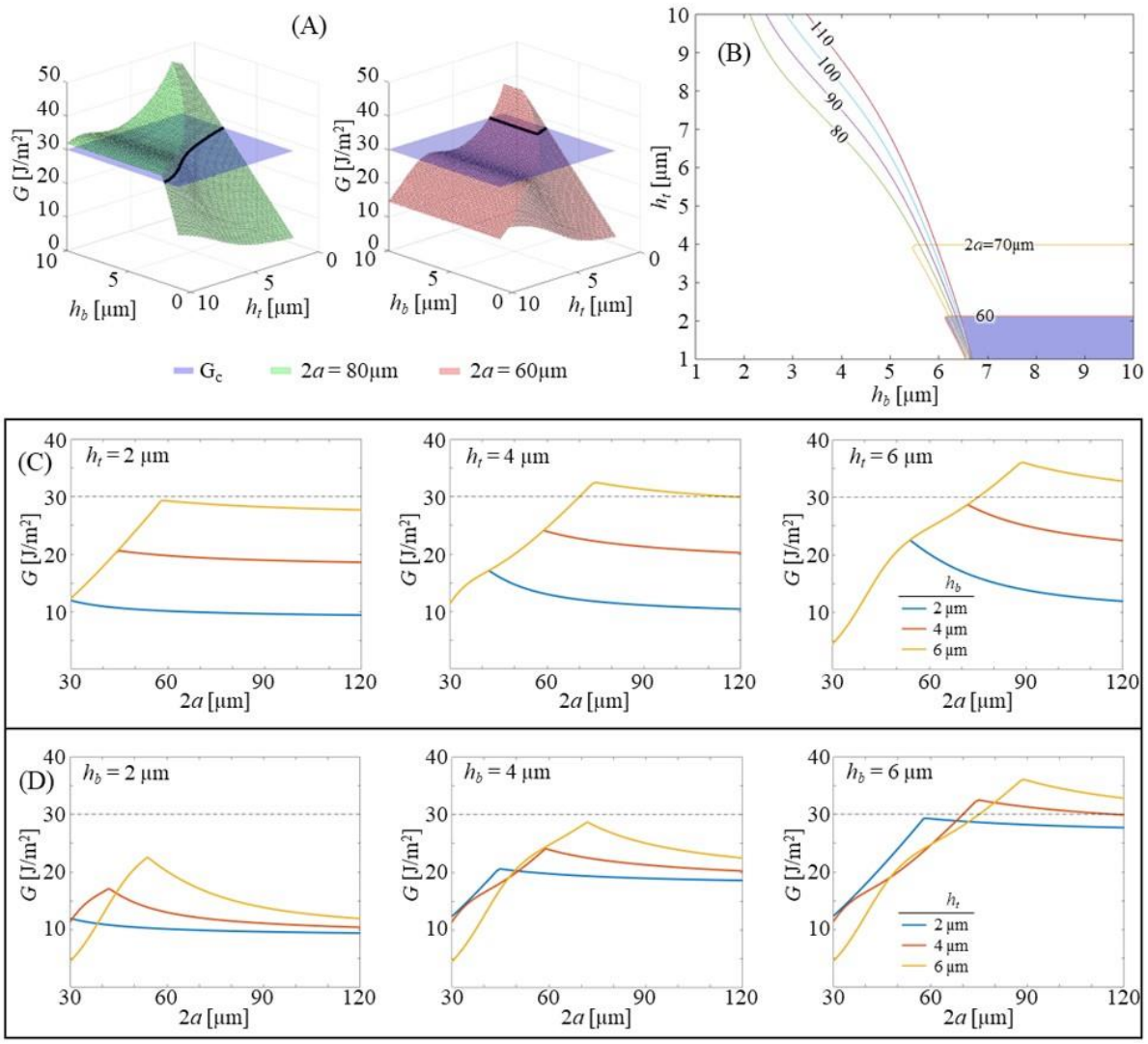

Figure 4.6: Delamination Mechanism Maps. (A) The surface plots show the mapping of the energy release rate varying both the top and bottom PI thickness for two different crack lengths. The blue surface on both plots is the critical energy release rate of 30 J/m^2 and the isolines are highlighted in black at the critical energy release rate. Any portion of the surface higher than the critical energy release rate will delaminate These isolines are then plotted in (B) for each silver width or crack length (2a) to create a design map of regions with and without delamination for all three geometric parameters. The delamination region is highlighted in blue as an example for the 60 μm crack length. (C) Individual graphs hold the top layer of PI constant, while showing curves for three different thicknesses of the bottom layer of PI. (D) Individual graphs hold the bottom layer of PI thickness constant, while showing curves for three different thicknesses of top PI. Part (C) and (D) show the individual effects of the top and bottom PI thicknesses in the vapor starved and vapor rich region along with the critical energy release rate of 30 J/m^2 shown by the dotted line.

4.5 Validation of Analytical Model by Finite Element Modeling

The analytical model described in section 4.3.2 captured both the bending and tensile stresses developed in thin polymer films/plates arising from a non-linear behavior. The model, however, still makes important assumptions such as small angle approximations, and no contribution from shear stress. While these assumptions are widely made with good results on the maximum stress developed, an accurate deformation result is important for determining the energy release rate in this model. In this section, results from the FE are discussed and compared against the analytical model to investigate the significance of these simplifications.

To validate the analytical model, two FE models were developed. The first FE model was designed as a 1:1 comparison with the analytical model to validate the deflection and strain energy results. A 2D analysis was conducted in ANSYS (Ansys Inc., Canonsburg, PA) with boundary conditions shown in Figure 4.7A. The void volume was calculated by summing the deflections of the surface nodes along the crack. Vapor starvation was detected (described in section 4.3.2) and the input pressure was iteratively changed until the error of $p_{vs}V$ and $n_a RT$ was less than 0.1%. The deflection of the midline nodes, reaction force in the *x* direction transverse to the interconnect, and strain energy were outputs of interest.

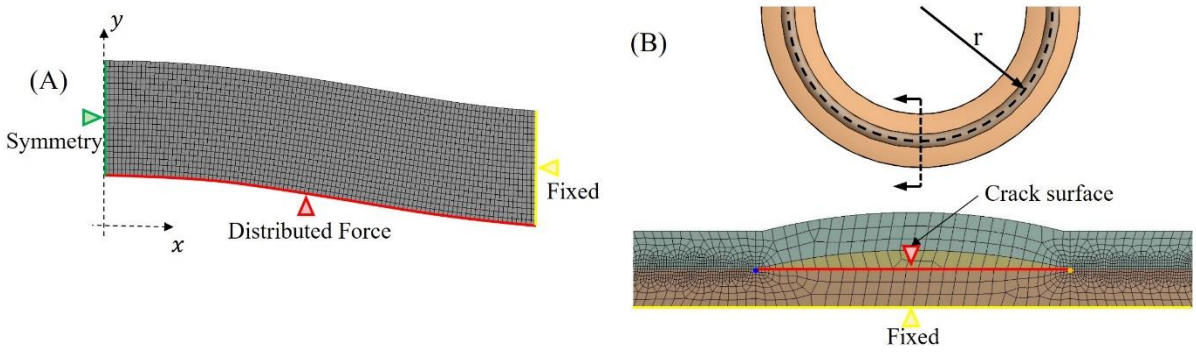

Figure 4.7: Finite Element models of vapor driven delamination. Model (A) is a direct comparison to analytical parametric model with fixed, symmetry and distributed force boundary conditions with plane strain behavior on 2D elements. Model (B) is axisymmetric 2D model to capture the meandering geometry, top and bottom layer of PI, presence of silver conductor, elastic/plastic material properties and the progressive interfacial delamination behavior. The blue and orange crack edge represents the inside and outside edge of the meander geometry.

The second model in Figure 4.7B was developed to capture more of the complexities that were not modeled in the analytical model including the presence of the silver interconnect, the meandering geometry, and incorporation of nonlinear material properties, and crack growth. A 2D axisymmetric model was developed with the cracks in a meandering pattern, i.e., a distance '*r*' away from the center of the axis around which the meander revolves (Figure 4.7B). The silver layer was included to match with the profile as shown in Figure 4.1A and D. The interface between the top and bottom layer of PI was modeled with shared nodes that could separate if the critical energy release rate criterion was met. The critical energy release rate is a material property, or in the case of interfacial delamination, a function of the bond strength. The virtual crack closure technique (VCCT) was utilized to calculate the energy release rate, *G*. The vapor pressure and void volume were calculated at each sub step, and if the vapor starvation condition was met, the simulation was stopped. Both the inner edge and outside edge of the crack were allowed to grow, and the energy release rate for each crack edge was calculated independently, allowing a comparison with the theoretical meander model (Equation 4.18).

Figure 4.8A compares the maximum displacement w_{max}, the tensile vs bending reaction characterized by the parameter u, and the energy release rate, G, between the analytical model and the first FE model. The displacement comparison in Figure 4.8A shows that the analytical model captures the nonlinear behavior shown by the FE analysis. The same trends are captured, with the FE model predicting a more rapid increase of maximum displacement, which in turn, affects the energy release rate, G, shown in Figure 4.8C. Once the vapor starved region is met, both models show the limit and reduction of the energy release rate. The nonlinear stress distribution is precisely captured as shown in the comparison for the u parameter in Figure 4.8B. This shows that the bending and tensile stress reactions are developed similarly in both the FE model and the analytical model as the deformation increases due to a larger crack length or higher pressure. This excellent agreement gives strong confidence that the parametric analysis of vapor delamination in printed electronics can be carried out using the analytical framework described earlier.

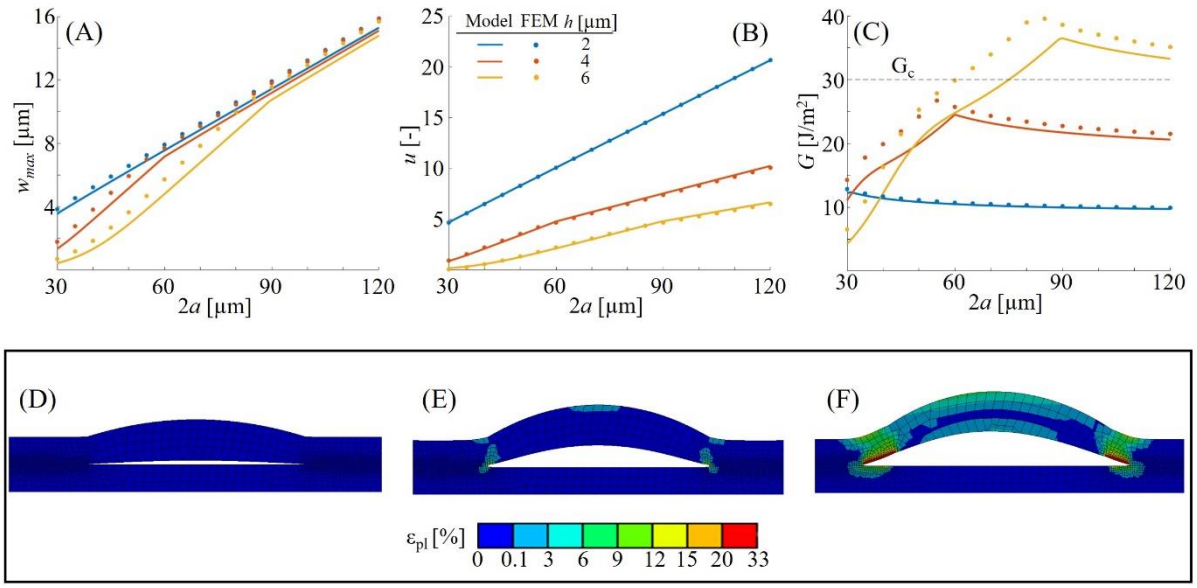

Figure 4.8: Finite element model results and comparison with analytical model. (A-C) Compares the analytical model to the direct comparison FE model. (A) Comparison of the maximum displacement w_{max} at the center of the blister. (B) Comparison of the u factor, which determines whether the deformation behavior in the blister is membrane or plate dominated. (C) Comparison of the energy release rate development between the two models also showing the critical energy release rate of 30 J/m^2. (D-F) Results of the progressive crack growth model with meander geometry. Growth of the crack is shown in (D-F) for a PI thickness of 6 µm and silver width of 50 µm where (D) the crack is just opening due to a lower pressure, (E) the crack is just about to grow, and (F) the crack has preferentially grown towards the inside edge. The energy release rate just before growth in (E) is G_i = 29.7 J/m^2 and G_o = 27.9 J/m^2. The plastic strain ε_{pl} is displayed by the color map and shows minor plastic strain just before crack growth (E) and not completely through the thickness of the top PI; contrasting with (F) where plastic strain has occurred across the thickness of the PI after initial delamination.

The second FE model incorporating the meanders and silver layer is shown in Figure 4.8D-F and shows the crack growth as pressure is applied to the crack surfaces. In Figure 4.8D, when the crack is just starting to grow as the void is pressurized, deformation is elastic and reversable. In the next step Figure 4.8E, the crack is just about to grow on the inner edge as the pressure has increased to $0.92p_{sat}$ and the inside edge and outside edge have an energy release rates of 29.7 and 27.9 J/m^2, respectively. This is larger than both the first FE model and analytical model, where the predicted energy release rates are 25.3 and 20.5 J/m^2, respectively. This difference may be due to the presence of the silver interconnect, and the 'elastic hinge' boundary formed between the edge of the thin film and the bulk rather than the fixed boundary

condition in both the analytical model and first FE model. The theoretical meander model in Equation 4.18 estimates that the energy release rate on the inner face, G_i, to be 8.7 % larger than G_o, and the FE analysis calculates that it is 6.5 % larger. Figure 4.8F then shows the progressive growth of the crack where the preferential direction is on the inside edge. The plastic strain after crack growth is through the thickness of the top PI layer, indicating significant plastic deformation, but not enough to rupture the meandering blister. Despite the added complexity of the meander FE model, the close agreement between the absolute and relative values of G_i and G_o lends confidence to both analytical model and the theoretical meander model developed in this chapter.

4.6 Design Implications

Several important design guidelines come out of the results discussed in this chapter. Careful design of the geometry of the printed interconnections, the fabrication process parameters, and the materials; all have an impact on reducing the likelihood of delamination. Geometric design guidelines along with insights related to process parameters and material choice can be elucidated from the geometric parameter models investigated. Design guidelines to mitigate vapor driven delamination are highlighted below:

- Reduce moisture availability by
    - Reducing thickness of the bottom encapsulant layer
    - Incorporating a drying step before final cure in oven
    - Utilizing encapsulant with low moisture uptake
- Reduce width of printed nanoparticle-based traces to decrease the initial crack length
- Increase the thickness of the top layer of encapsulant layer
- Increase the meander radius, and

- Decrease the curing/sintering temperature

Reducing the moisture available is the most effective way to mitigate vapor driven delamination in flexible and stretchable electronics, and can be addressed with geometric design, process design, and material choices. Introducing a drying step or slow temperature ramp is perhaps the most easily implemented design change to reduce moisture availability, as it only requires simple oven temperature control and a short period of time to drive off moisture before reaching the final curing or sintering temperature. Reducing the width of the printed nanoparticle-based trace is a geometric design parameter that can be changed to address delamination, but design changes in the conductor geometry may affect the electrical performance. If possible, conductor cross sections with higher aspect ratio will decrease the likelihood of vapor driven delamination while maintaining required electrical conductance. Increasing the thickness of the top polymer layer is another geometric design consideration as the increased bending resistance reduces the energy release rate for smaller cracks where the bending stresses dominate. However, increasing the thickness of the top polymer layer also increases the thermoelastic driven energy release rate. Increasing the meander radius can also mitigate delamination, but also impacts the areal footprint of the interconnection and can impact conductor densities. Decreasing the sintering/curing temperature will significantly reduce the maximum vapor pressure and proportionally reduce the thermoelastic strain to drive delamination. However, changing the sintering temperature may limit choice of material for the conductor or the sintering method[108] and may affect the mechanical and electrical properties of the interconnect.

4.7 Conclusions

Experimentally observed delamination is analyzed using a nonlinear fracture model with vapor pressure as the driving force. The results from the analytical model are consistent with experimental observations and are verified through FE modeling. The parametric model results in ‘delamination mechanism maps’ for flexible and stretchable electronics where two regimes described as vapor rich and vapor starved control the delamination. Transitioning from the vapor rich to vapor starved region, the energy release rate is limited and dominated by the moisture availability rather than the top film thickness and initial crack size. Designing a flexible and stretchable interconnection geometry and process in the vapor starved regime is therefore critical in reducing the likelihood of delamination. A delamination mechanism map and design guidelines are presented to reduce the energy release rate in both vapor pressure and thermoelastic driven delamination. The metallic interconnection width is shown to be the second most critical dimension by both experimental observation and parametric model as the energy release rate can be reduced by 77 % when the metallic width is reduced from 50 μm to 30 μm when all other parameters are kept the same. Meander geometries are also investigated via a perturbation of the straight crack model, and the inside edge of the meander is shown to have a higher energy release rate when compared to the outside edge. These results provide important design considerations for improving the reliability of printed flexible and stretchable electronic devices.

Chapter 5

Sintering Process Development for Nanoparticle Silver Ink in 3D Stretchable Interconnects

Printed colloidal nanoparticle inks, such as the silver ink used to fabricate the 3D interconnects developed in this thesis, must be sintered to continuous structures, and achieve electrical conductivity. Thermal sintering is the most common method to achieve conductivity, with higher temperatures and longer exposure times generally yielding films with higher conductivity.[109] However, directly printed conductors on flexible and stretchable substrates are usually sintered at lower temperatures to preserve the stretchable (polymer) substrate, resulting in lower conductivities and brittle material properties.[36,110] Several methods have been investigated to sinter metallic nanoparticles without damaging the substrate materials including pulsed laser,[39,111] microwave,[112] chemical,[113] flash sintering,[114,115] or plasma sintering.[116] These methods are capable of removing caping ligands from the nanoparticles and facilitate nanoparticle coalescence. Additionally, the ink composition can be tuned to reduce the sintering temperature to achieve high conductivity by changing the nanoparticle size and nanoparticle capping materials to promote sintering at lower temperatures.[117,118]Additional ink formulations include dispersed metallic nanowires,[119] carbon nanotubes,[120] or particle free metal-organic decomposition (MOD) inks.[121] Regardless of the type of sintering method used,

flexible interconnect systems are accompanied with engineering strategies such as discontinuous interlayers[65,122] or serpentine or self-similar geometries[123] to prevent cracking in the conductive layer due to its elastic modulus mismatch with the soft substrate. Additionally, intermediate layers (with an intermediate elastic moduli) have been utilized to reduce stiffness gradients and prevent cracking.[9,18]

Previous investigation from Chapter 3 shows that utilizing inert or vacuum environments can preserve PDMS up to temperatures as high as 300 °C, while maintaining its stretchability. This would allow for thermal sintering of the metallic conductor consistent with the process temperatures capable of fabricating complex 3D structures including lattices, wavy plates, and pillar structures directly on the stretchable substrate.[35,124] These 3D structures open a wide design space for stretchable electronics such as multi-layered electronics, targeted epidural contact, wireless data and power transfer, and external wired connections. However, inert ambient environments have been shown to decrease the removal of the organic capping ligands and binders, which is required before sintering can occur in metallic nanoparticle inks.[113,125-127] Cracking in colloidal inks is also a common occurrence,[128-131] and several models have linked an increase in the solvent evaporation rate to an increase in cracking due to the capillary pressure, which leads to increased tensile stress in the drying film.[132-134]

The research covered in this chapter is undertaken to demonstrate a fabrication method to create directly printed crack-free interconnects with 3D pillars for external connectivity and multi-layer connection as described in Chapter 2. The focus is on understanding the mechanisms of interconnect cracking that would guide mitigation strategies and understanding microstructure development during sintering of colloidal nanoparticle inks to increase electrical conductivity, while also maintaining process conditions that are compatible with the PDMS substrate. We hypothesize that cracking observed in initial prototypes occurs due to

capillary pressure during drying and sintering steps, and that organics in the nanoparticle ink need to be effectively removed to promote sintering. An experimental stepwise variation of the thermal/atmospheric process conditions from a purely vacuum based process (developed in Chapter 4) to a hybrid process, which includes the presence of air during the drying step, is caried out to test this hypothesis. The hybrid process is shown to produce crack-free interconnects with high conductivities (up to 56% of bulk metal) while having an excellent compatibility with the underlying polymer materials. Shear tests are carried out to demonstrate the strength of printed pillars that act as conductive connections to the external environment, while an adhesion test is used to establish adequate bonding between the top and the bottom PDMS layers encapsulating the interconnects. Utilizing these learnings, an embedded 3D stretchable interconnect directly printed on PDMS with high conductivity and no cracks is demonstrated.

Contents of this chapter have been published as:
Brenneman, J., Tansel, D. Z., Fedder, G. K., & Panat, R. (2022). High-Conductivity Crack-Free 3D Electrical Interconnects Directly Printed on Soft PDMS Substrates. *Advanced Materials Technologies*. doi:10.1002/admt.202200396

5.1 Experimental Method

5.1.1 Sample Geometry

The 3D stretchable electronic interconnect in this investigation consisted of aerosol jet printed silver interconnects printed directly onto a printed polyimide layer. The schematic of the sample layout is shown in Figure 5.1C. There are 12 interconnects on each sample wafer including three meandering interconnects and one straight interconnect for each sample set: hollow circle pillars, full taper pillars, and four wire resistance samples. Two different pillar designs were selected to focus on this work and include the circular hollow pillar (Figure 5.1A), and the tapered full pillar (Figure 5.1B). The pillars are utilized to investigate the cracking at the pillar base and the shear loading, while the four wire resistance samples are used to measure the conductivity of the printed silver interconnect using four-point resistance measurement.

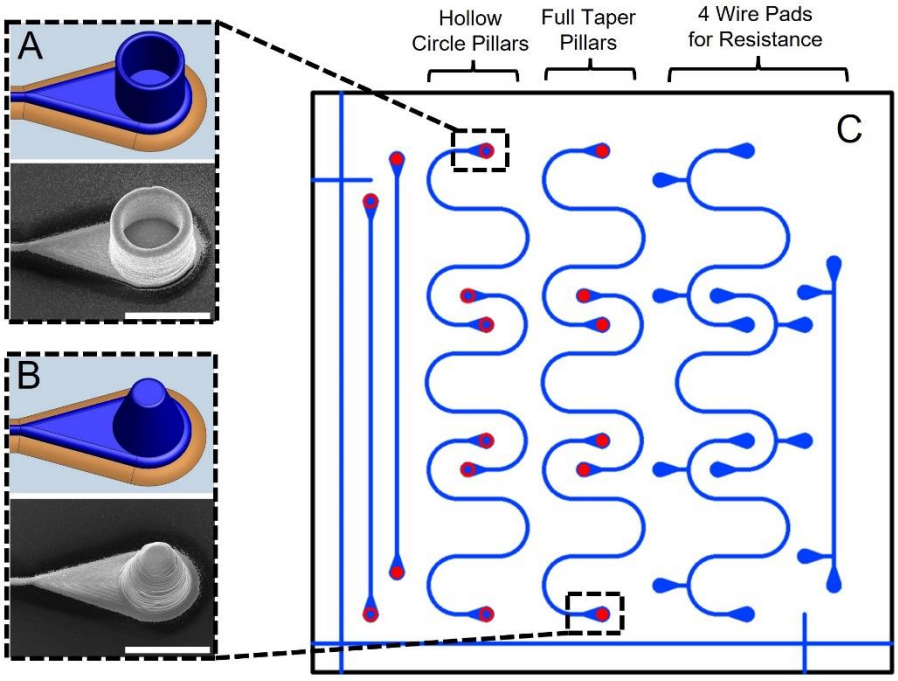

Figure 5.1: Sample layout and pillar types used for sintering investigation. The sample layout (C) where the four repeated samples are shown for the hollow circle pillars, full taper pillars, and the 4 wire samples for precise resistance measurements. Each sample set is printed on a 1 cm x 1 cm wafer and has three meander interconnects and one straight interconnect. Renderings and SEMs of fabricated geometries are shown in (A-B) for the (A) hollow circular pillar and (B) taper pillar. Scale bars are 200 μm.

5.1.2 Sintering Environments

Pretreatment of the PDMS, curing of the PI layers, and sintering of the Ag layer is conducted inside of a vacuum chamber with programmable temperature ramp rates and holding steps capable of reaching 300 °C and 0.13 Pa vacuum with either air or N_2 as the filler gas. The process conditions are varied between samples to investigate its effect on the cracking and conductivity of the silver layer. The process condition being tested is kept the same for the PI curing and Ag sintering steps within the same sample to minimize any effect of the differential treatment of the PI. The initial thermal treatment carried out under vacuum conditions is shown in Figure 5.2A, including a drying step that is incorporated to prevent delamination between the PI layers (an outcome of Chapter 4). The hybrid process, starting with drying in air followed by sintering in vacuum, is shown in Figure 5.2B. The process conditions are summarized in Table 5.1, where process conditions #2 and #17 correlate with the processes shown in in Figure 5.2A and B, respectively.

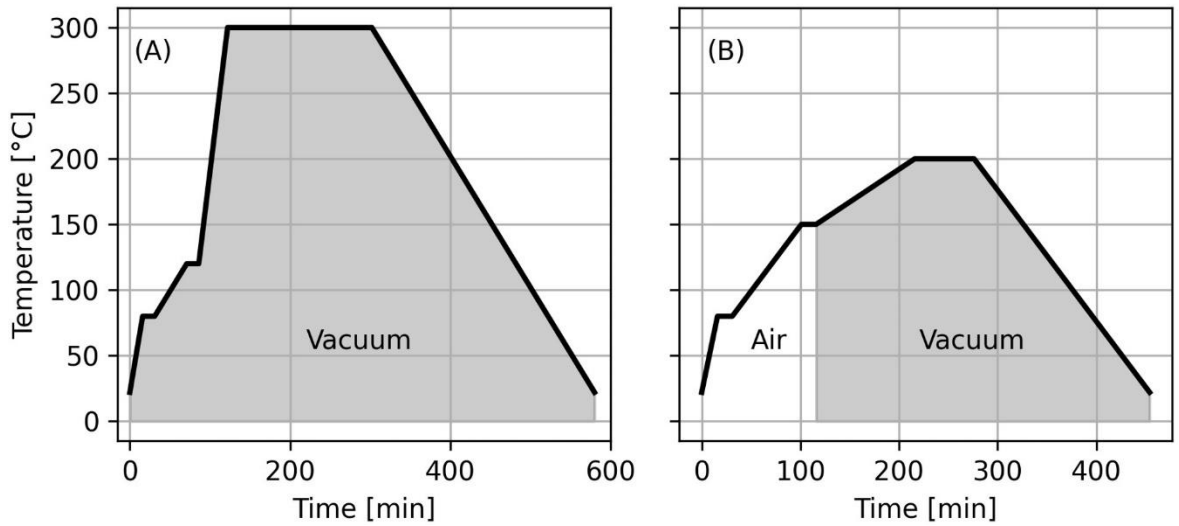

Figure 5.2: Sintering process development - initial full vacuum to hybrid process. (A) First prototype sintering thermal profile that caused low conductivity and cracking. (B) The proposed profile to achieve simultaneous elastic PDMS and high conductivity and crack free interconnects and pillars.

Table 5.1 shows the printed and sintered silver interconnect lines fabricated using 18 different process conditions evaluated in this chapter. For each process condition, the conductivity is reported as the average of measurements from four interconnects shown in Figure 5.1C, along with crack observations and compatibility with PDMS. Since the study is focused on sintering environments and the effect on cracking, electrical conductivity and microstructure, a majority of the samples are printed without the PDMS or PAA release layer present. Interconnects fully embedded in PDMS are then fabricated according to the process shown in Figure 2.5 and tested (experiment 16-18 in Table 5.1).

Table 5.1: Sintering process conditions and the resulting conductivity, cracking, and PDMS compatibility.

		Drying Step			Sintering Step				Observations			
Experiment	Sample Substrate	Pressure	Gas	Max Temp	Pressure	Gas	Max Temp	Ramp Rate	Conductivity	Cracks	Compatible with PDMS	Problem
		[kPa]	[-]	[°C]	[kPa]	[-]	[°C]	[°C min^{-1}]	[%] of Bulk Ag			
1	Si	-	-	-	0.13	N_2	300	5	0.00008%	Severe	Yes	Cracking
2	Si	0.13	N_2	120	0.13	N_2	300	5	0.28%	Severe	Yes	
3	Si	0.13	N_2	150	0.13	N_2	300	5	0.06%	Severe	Yes	
4	Si	0.13	N_2	120	0.13	N_2	300	0.5	2%	Severe	Yes	
5	Si	0.13	N_2	120	0.13	N_2	300	0.5	1%	Severe	Yes	
6	Si	101	N_2	120	101	N_2	300	5	29%	Minor	No	
7	Si	101[a]	N_2	120	101	N_2	300	5	28%	Moderate	No	
8	Si	101	N_2	120	101	N_2	300	5	16%	Moderate	No	
9	Si	101	N_2	120	101	N_2	300	0.5	24%	None	No	Compatibility with PDMS
10	Si	101	Air	120	101	Air	300	5	62%	None	No	
11	Si	101	Air	120	101	Air	300	5	67%	None	No	
12	Si	101	Air	150	101	Air	200	5	64%	None	No	
13	Si	101	Air	150	101	Air	200	5	59%	None	No	
14	Si	101	Air	150	0.13	N_2	300	5	56%	None	Yes	None
15	Si	101	Air	150	0.13	N_2	200	5	39%	None	Yes	
16	PDMS+ PAA+Si	101	Air	150	0.13	N_2	200	5	25%	None	Yes	
17	PDMS+ PAA+Si	101	Air	150	0.13	N_2	200	0.5	37%	None	Yes	
18	PDMS+ PAA+Si	101	Air	150	0.13	N_2	300	5	43%	None	Yes	

[a] Included a vacuum purge step

5.1.3 Sample Characterization

Sample interconnect resistance is measured with a four-point probe at the locations shown in Figure 5.1C (2401 SourceMeter, Keithley Instruments, Cleveland, OH). Pillar to pillar resistance is measured with two-point probe at the locations shown in Figure 5.1A and B. Cross-sectional profiles of the printed lines are measured with profilometer scans (Dektak 3, Bruker Corporation, Billerica, MA) to determine conductivity of the sintered silver along with the resistance measurements. The Ag cracks and microstructure are characterized with SEM images (Quanta 600, FEI, Hillsboro, OR) utilizing focused ion beam (FIB) (Nova Nanolab 600, FEI, Hillsboro, OR) cutting to expose the cross section of cracks and internal microstructure of the traces and pillars. ImageJ[135] and TauFactor[136] are used to analyze the images. Additionally, thermogravimetric analysis (TGA) (Q50, TA Instruments, New Castle, DE) is performed on the Ag nanoparticle (NP) ink in both air and nitrogen to investigate the binder and surfactant removal under inert and reactive environments.

The pillar shear test set-up is shown in Figure 5.3. In this setup, the samples are loaded horizontally on a four-axis micro stage to allow for their precise positioning under the load cell (LSB200, Futek, Irvine, CA) and contact head, as shown in Figure 5.3B. The samples are positioned so that the contact head would apply the load on the pillar about 50 μm from the pillar base, as shown in Figure 5.3A. The optical images captured with the attached camera are analyzed with ImageJ to measure the distance from the pillar base to the contact point for use in the stress calculations along with SEM images taken pre and post failure. The load cell is mounted on a linear stage (X-LSM025, Zaber Technologies Inc., Vancouver) and driven at a constant rate of 0.5 μm/s. A MATLAB (MathWorks, Natick, Massachusetts) script is used to record both the displacement and load simultaneously.

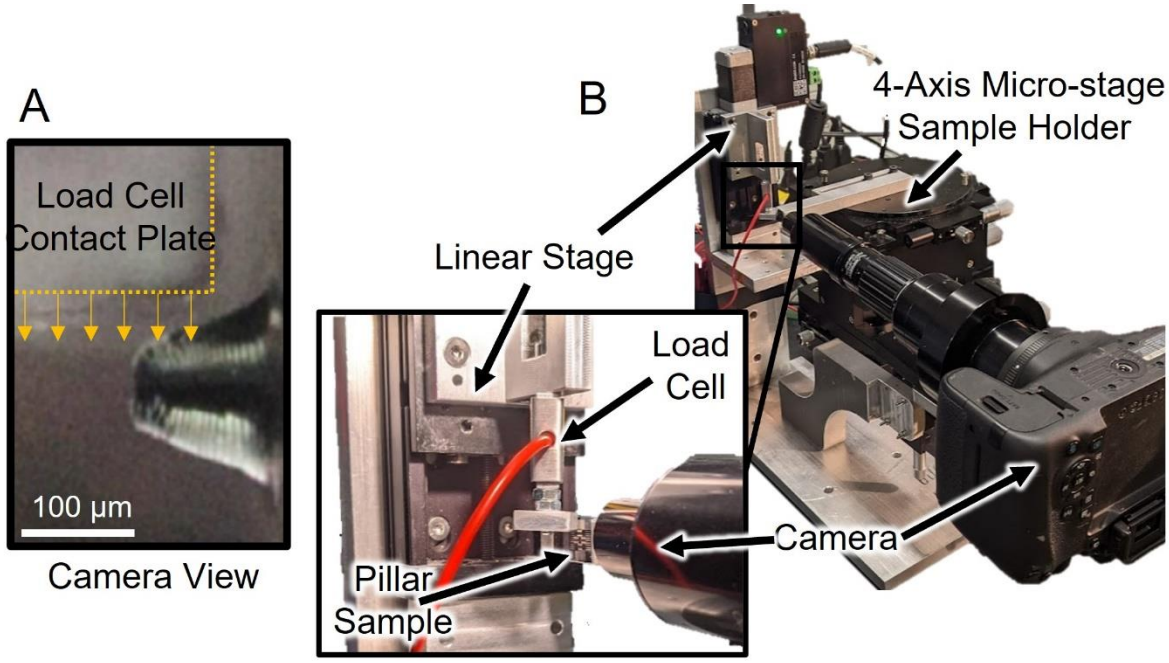

Figure 5.3: Micropillar shear test set up. The pillars were placed under shear loading from the contact plate moving down at a constant velocity. (A) The view from the camera shows the contact plate (the edge is highlighted by the dotted line) approaching the pillar as it moves downward (shown by the arrows). (B) The test set up with the four-axis micro-stage sample holder, the load cell attached to the linear stage, and camera are shown. The inset image has more details of the load cell and pillar sample location.

Adhesion between the top and bottom PDMS layers is tested using ASTM D3359 Tape Adhesion Test (Test Method B - guidelines for 50-125 µm thick materials).[137] The bottom layer of 20:1 PDMS is spin cast, cured at 100 °C for 1 hr, and treated with three heating profiles as shown in Figure 5.2B to replicate the curing and sintering conditions of PI and Ag. The top layer of 20:1 PDMS is spin cast and cured at 100 °C for 1 hr. Cross sections following ASTM D3359 are cut using a sharp cutter (Curio™, Silhouette America, Lindon, UT, USA). A tape is then used according to the same standard to test the adhesion between the two PDMS layers.

5.2 Mitigating Cracks Developed During Thermal Sintering

For process conditions 1-5 in Table 5.1, the samples experience vacuum during the drying step at the beginning of the thermal treatment and all display cracking as represented in Figure

5.4 and Figure 5.5. Focused Ion Beam (FIB) cuts are made to image the cross section of the crack to investigate the crack morphology. Close-up images of the crack (Figure 5.4C and Figure 5.5C) show that the crack extends through the entire layer of the silver with a separation of 3.2 µm for the taper pillar and 4.0 µm for the circular pillar, indicating mode-I fracture. Additionally, the silver layer delaminates from the substrate in both the taper pillar and circular pillar geometry as the crack extends underneath the pillar displaying shear or mode-II fracture as shown in the Figure 5.4D and Figure 5.5D. The delamination distance under the tapered pillar is over 18 µm and continues out of the field of view of the image. Under the hollow circular pillar, the delamination distance was measured to be 28 µm, which extends under a large portion of the pillar wall. The delamination also occurred under the meandering interconnect side of the crack as well, but not to the same extent as under the pillar.

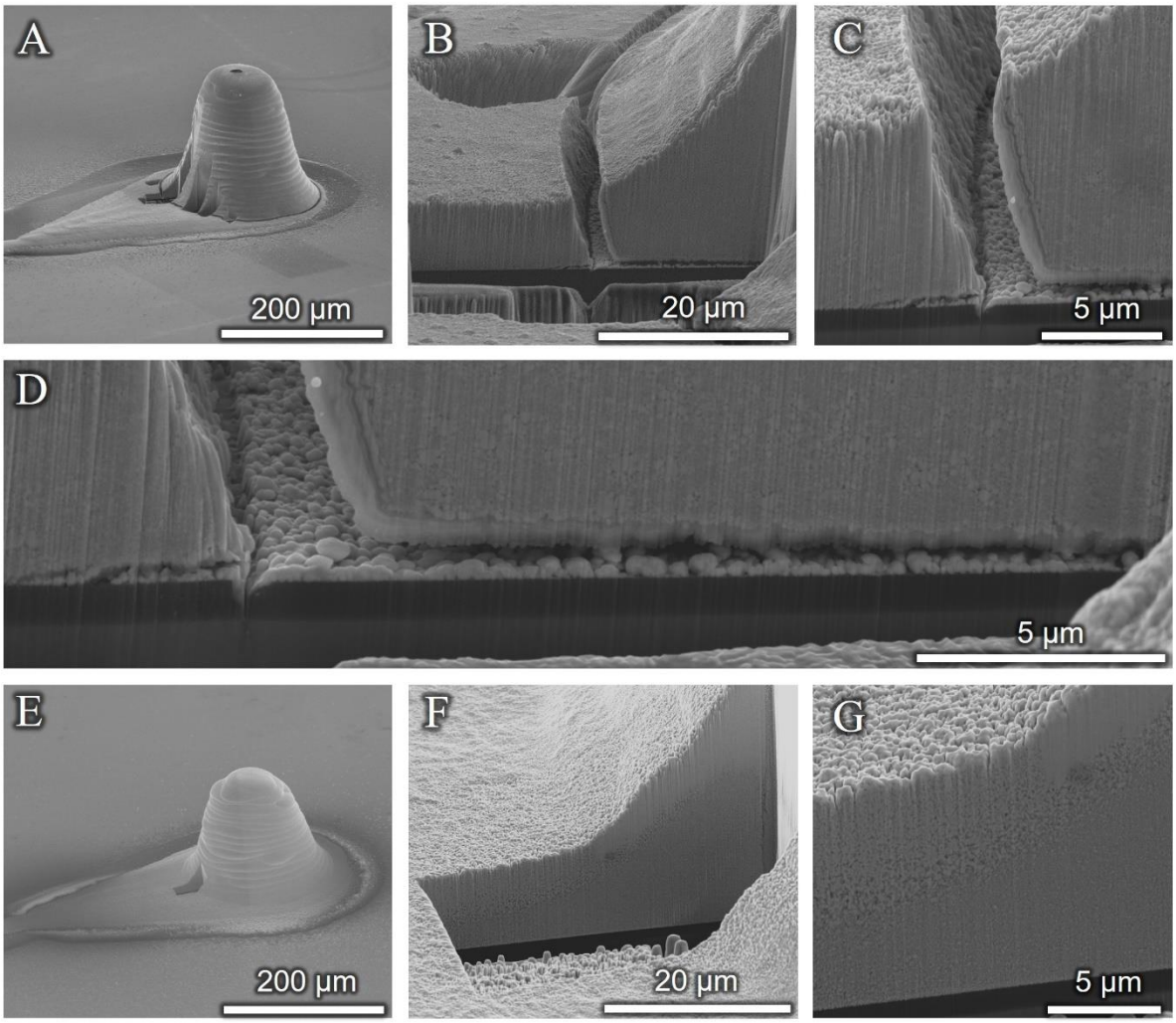

Figure 5.4: SEM images of uncracked and cracked tapered pillar geometry with FIB cross sections. (A-D) Shows cracked taper pillar with FIB cross section when sintered under process 2. (E-G) Shows uncracked taper pillar with FIB cross section to verify no internal cracking when sintered under process 13.

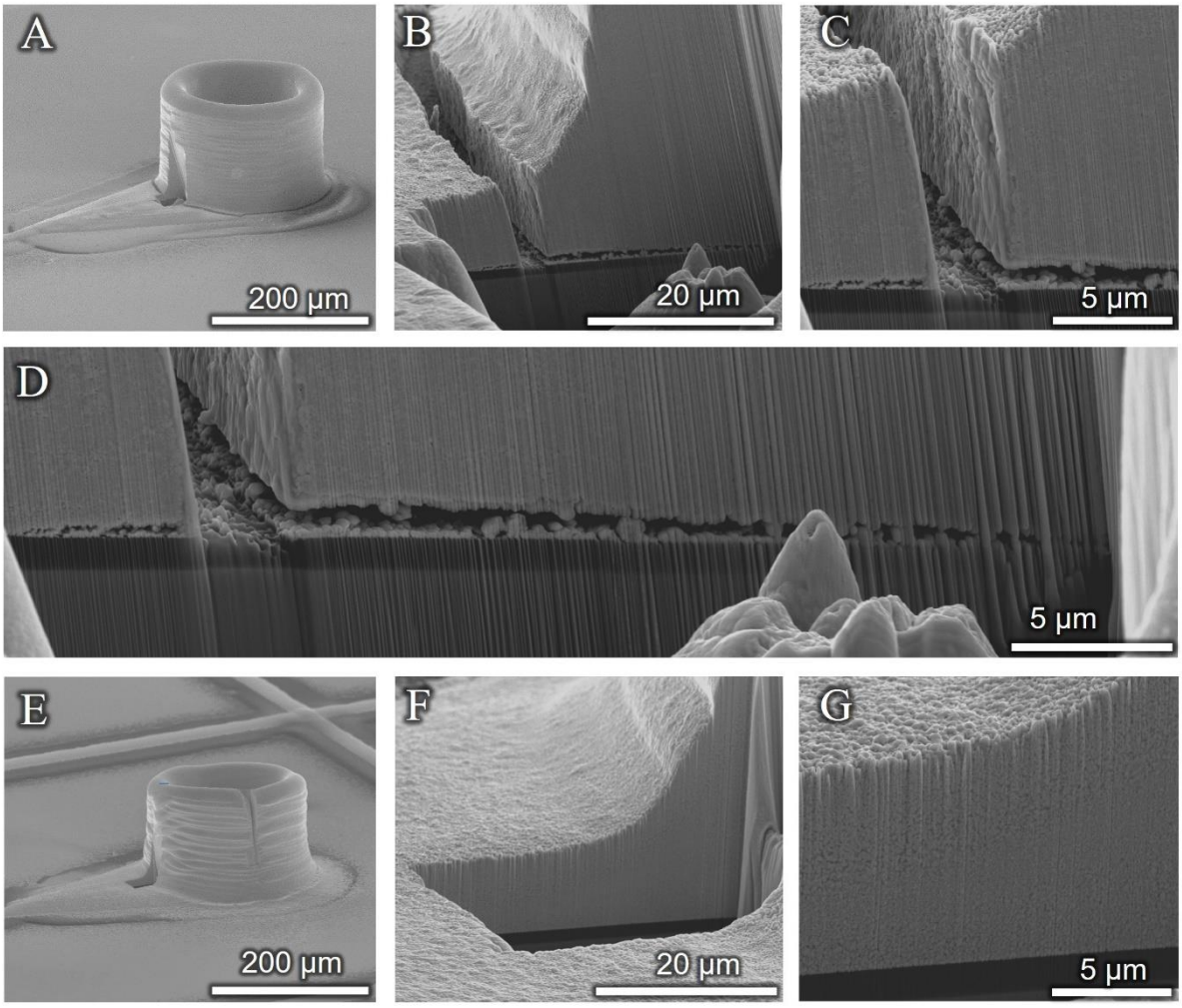

Figure 5.5: SEM images of uncracked and cracked circular pillar geometry with FIB cross sections. (A-C) Shows cracked hollow circular pillar with FIB cross section when sintered under process 2. (E-G) Shows uncracked hollow circular pillar with FIB cross section to verify no internal cracking when sintered under process 13.

The location of the cracks at sharp geometric transitions such as the pillar base (Figure 5.4 and Figure 5.5) and the pad-to-interconnect boundary (Figure 5.6), but not on the meandering interconnects, indicates that local stress concentration is important for crack initiation. We note that thermal expansion mismatch between the different materials would cause a residual stress during thermal cycling. The thermal expansion mismatch, however, is unlikely to be the critical driving force for cracking in the current investigation, because all samples subjected to the same thermal profile should demonstrate similar cracking behavior, which is not the case in

the current observations (e.g., for samples subjected to similar thermal histories, cracking is observed only in the samples subjected to vacuum and nitrogen environments in the initial drying step). This assessment led to the hypothesis stating that the increased solvent evaporation rate in vacuum and nitrogen, relative to air, increases the local stress to a level which is capable of initiating cracks during the drying of the packed particle structures.

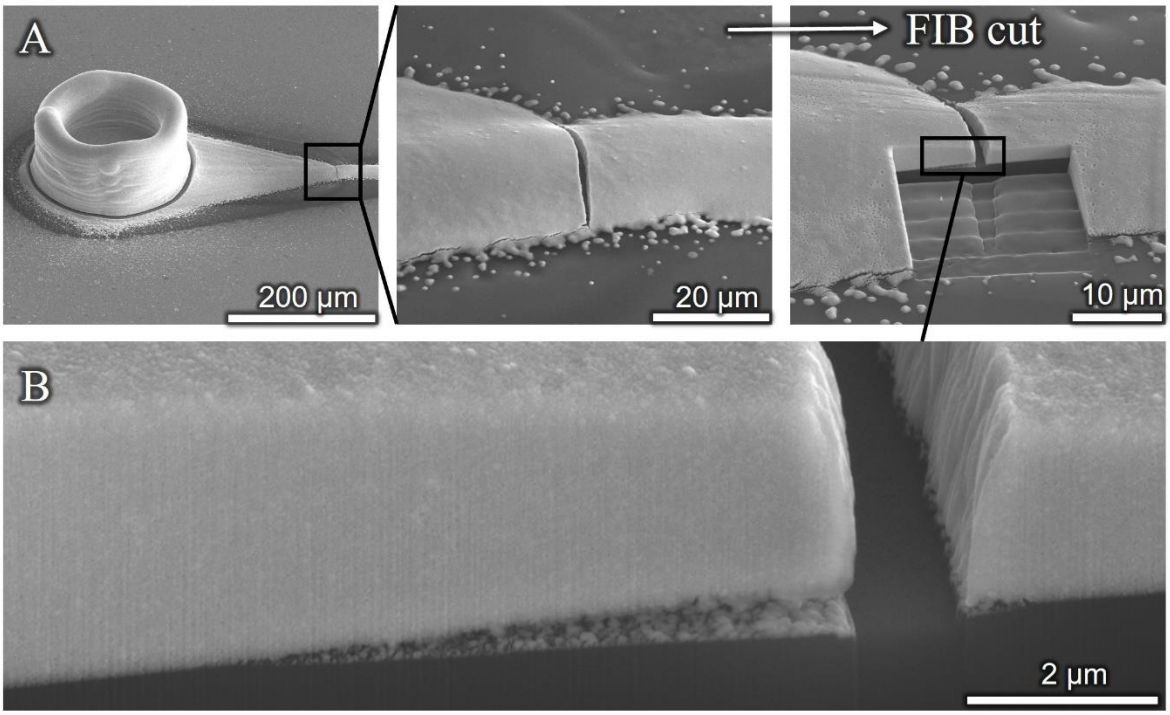

Figure 5.6: SEM of crack at the pillar pad to interconnect transition. (A) SEM image of the pillar, pad and interconnect, where the inset images show the close of the interconnect transition, and the FIB cut location on process 3. (B) SEM image of the FIB cut cross section.

Cracking in printed metallic nanoparticle (NP) inks has been observed across printing techniques including extrusion,[128] inkjet,[130] and aerosol jet printing.[129] We note that cracking during drying of thin films of colloidal dispersions is a well-documented phenomenon and there is rich discussion about the stress and material response leading to cracking.[138] The driving force for cracking is typically provided by the capillary pressure between particles developed during drying as depicted in Figure 5.7B.[139,140] Several models have been proposed

to describe the capillary pressure and resultant film stress and have shown reasonable agreement with experiments with silica colloids.[141] This negative capillary pressure results in a compressive force to pull the nanoparticles together and shrink the film. The film can shrink out-of-plane, but when the film is constrained on the substrate, the capillary force causes an in-plane tension in the film, which can be relieved by fully drying or cracking (see Figure 5.7B**)**.

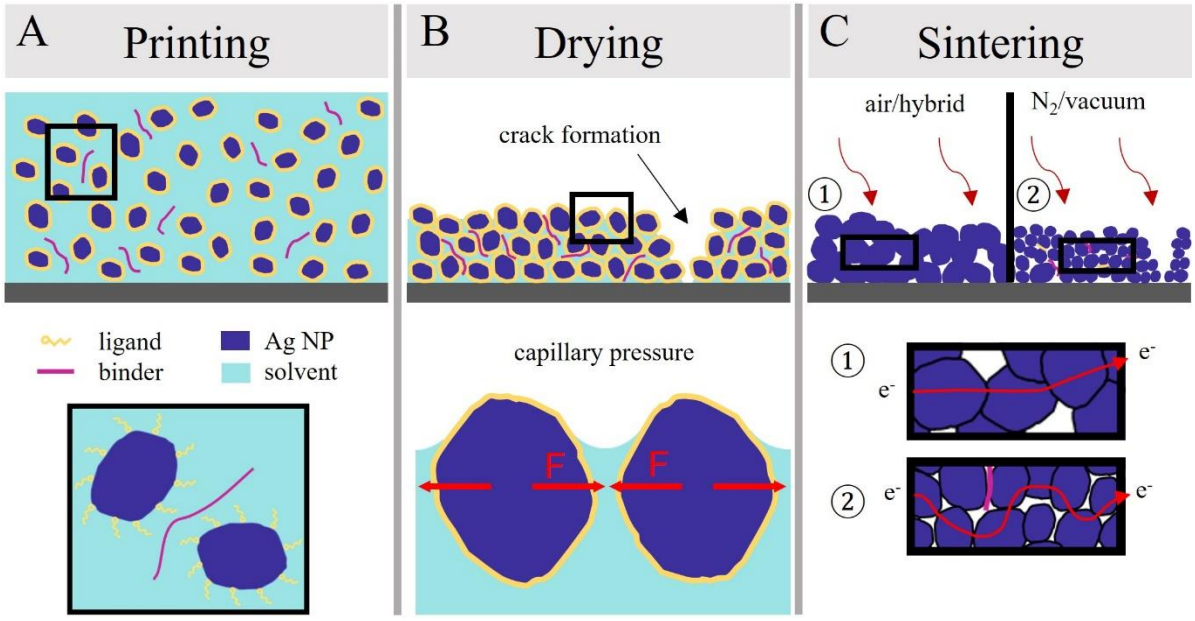

Figure 5.7: Schematic of process steps for electrical functionalization of colloidal NP ink. (A) The as printed colloidal ink, where the inset shows the composition of the ink. (B) The drying step where the inset image shows the development of capillary pressure. (C) The sintering step where the two inset images compare electron pathways between ink sintered in air vs nitrogen and vacuum environments.

The capillary pressure has a maximum achievable value $P_{max} = 10\gamma/R$ where γ is the surface tension and R is the particle radius.[139] The actual capillary pressure P developed in the consolidated region is determined by the film thickness, evaporation rate, and the permeability of the film and is limited to magnitudes less than P_{max}. Salamanca et al.[142] describes the dimensionless capillary pressure P_{cap} as the ratio of the maximum capillary pressure P_{max} to the developed capillary pressure P as,

$$P_{cap} = \frac{20}{75}\left(\frac{3\gamma\eta_0}{\dot{E}}\right)^{1/2}\frac{R(1-\phi)^2}{\mu\phi^2 H} \quad 5.1$$

where η_0 is the dispersion low shear viscosity, $\dot{E}$ is the evaporation rate, ϕ is the volume fraction of particles at close packing, μ is the solvent viscosity and H is the initial film thickness. Manipulation of Equation 5.1 by inserting the expression for the maximum achievable capillary pressure returns the capillary pressure developed in the film as

$$P = \frac{75}{2}\left(\frac{\dot{E}\gamma}{3\eta_0}\right)^{1/2}\frac{\mu\phi^2 H}{R^2(1-\phi)^2} \quad 5.2$$

The developed in-plane tensile stress, σ, is directly proportional to the capillary pressure, which leads to the ability to compare the film stress for different process conditions. The initial film thickness is the same for all samples and the volume fraction of the particles at consolidation is also assumed to be independent of sintering ambient environment. The low shear viscosity of the dispersion is a function of the volume fraction directly scaled by the solvent viscosity. Thus, following the assumption that volume fraction at close packing is the same for all samples, a comparison of in-plane tensile stress can be made that includes only the evaporation rate, surface tension, and solvent viscosity, as

$$\frac{\sigma_{vac}}{\sigma_{air}} = \left(\frac{\dot{E}_{vac}\gamma_{vac}\mu_{vac}}{\dot{E}_{air}\gamma_{air}\mu_{air}}\right)^{1/2} \quad 5.3$$

Equation 5.3 compares the film stress developed in vacuum with that developed in air; and can also be used to compare the stress between different conditions. The surface tension and the solvent viscosity are temperature dependent, so differences in solvent evaporation rate will determine the temperature at which the film consolidates and develops capillary pressure, which may be different for the different sintering conditions. As temperature increases, both

the viscosity and the surface tension decrease, thereby reducing the tensile stress in Equation 5.3 at the point of consolidation.

From Figure 5.4 and Figure 5.5 and Table 5.1, both the vacuum and N_2 conditions resulted in cracking at the pillar base (with the exception of process condition for experiment #9 in Table 5.1), while all samples dried in air were crack-free. Utilizing Equation 5.3, a comparison of the film stress can be made between the process conditions by estimating the solvent evaporation rate during film consolidation and close packing. The solvent for the ink used in this study comprises of water and ethylene glycol, and the significantly lower vapor pressure of ethylene glycol (12 Pa) vs water (3200 Pa) at 25 °C leads to the assumption that at close packing, only ethylene glycol remains as the solvent.[143] Measured evaporation rates for ethylene glycol with process conditions closely matching the ones used in this study are available for vacuum,[144] atmospheric pressure N_2 with gas flow,[145] and atmospheric pressure air.[146] The Hertz-Knudsen equation was used to scale evaporation rates to the same temperature of 25 °C, and are reported to be 52, 1.3, and 0.10 mg min^{-1} cm^{-2} for vacuum, 101 kPa N_2, and air environments, respectively. These evaporation rates are for pure liquid. Although the presence of nanoparticles, ligands, and binders present in the ink is expected to affect the absolute values of the evaporation rates, their relative rates can still be estimated to compare tensile film stress under different process conditions. Using Equation 5.3 and the reported evaporation rates, the film stress developed during drying under the N_2 environment is 3.4 times higher than in air, and the film stress developed in vacuum is 23 times higher than that in air. The significantly larger stress developed in vacuum conditions during drying is consistent with the experimental observations and supports the hypothesis that the cracking is caused by capillary stress developed during drying. The increased drying stress in N_2 relative to air is also indicative of drying stress driving the crack for the interconnect. Of the four

samples dried under 101 kPa N_2 environment, three displayed complete cracks through the thickness of the silver, while the fourth displayed a minor crack. These observations indicate the stress developed in drying under 101 kPa N_2 environment, local to the pillar base, is approximately the critical stress required to initiate crack growth in a packed particle film. When samples underwent the drying step under air followed by vacuum for sintering, such as in experiments #14-18 in Table 5.1, no cracking was observed, which further indicates that the cracks were initiated in the drying portion of the process.

5.3 Microstructure and Electrical Conductivity of Sintered Interconnect

Samples that experience vacuum or inert environment for the entirety of the thermal treatment resulted in low conductivity for process conditions 1-9 in Table 5.1. This low conductivity is not caused by the cracks shown in Figure 5.4, Figure 5.5, and Figure 5.6 as the four-wire resistance test features used to determine the conductivity did not display cracks at the pad-to-trace transition or along the trace section measured by the multimeter and shown in Figure 5.1C.

To assess the effect of processing conditions on the microstructure of the interconnects, we analyzed FIB cross-section images of several samples processed under the conditions shown in Table 5.1. Figure 5.8A-C show the microstructure of the samples sintered in vacuum, 101 kPa N_2, and air environments (the conditions in experiment #2, #8, and #11 in Table 5.1), respectively. These samples were supplied with identical heating profiles and vary only the ambient conditions. The microstructures appear significantly different, and the presence of oxygen has catalyzed the breakdown and removal of the organic ligands and binders to promote sintering. Very limited necking and particle size comparable to the original ink is observed in the microstructure of the vacuum sintered sample in Figure 5.8A, indicating poor sintering.

The microstructure in Figure 5.8B (dried and sintered under N_2 environment) shows an increase in average particle size and a higher degree of NP necking compared to the vacuum sintered condition. This effect may be partly due to more uniform heating due to the inclusion of convection as an additional heat transfer mechanism vs that in vacuum. Further, there may be trace amounts of oxygen present as the oven is only sealed under vacuum pressure. The microstructure in Figure 5.8C is for the sample sintered in air, showing a significant increase in necking and average grain size indicating increased sintering. Along with the increased particle size and necking, the conductivity of the samples represented in Figure 5.8A, B, and C increased and was 0.28 %, 16 %, and 67 % of bulk silver, respectively.

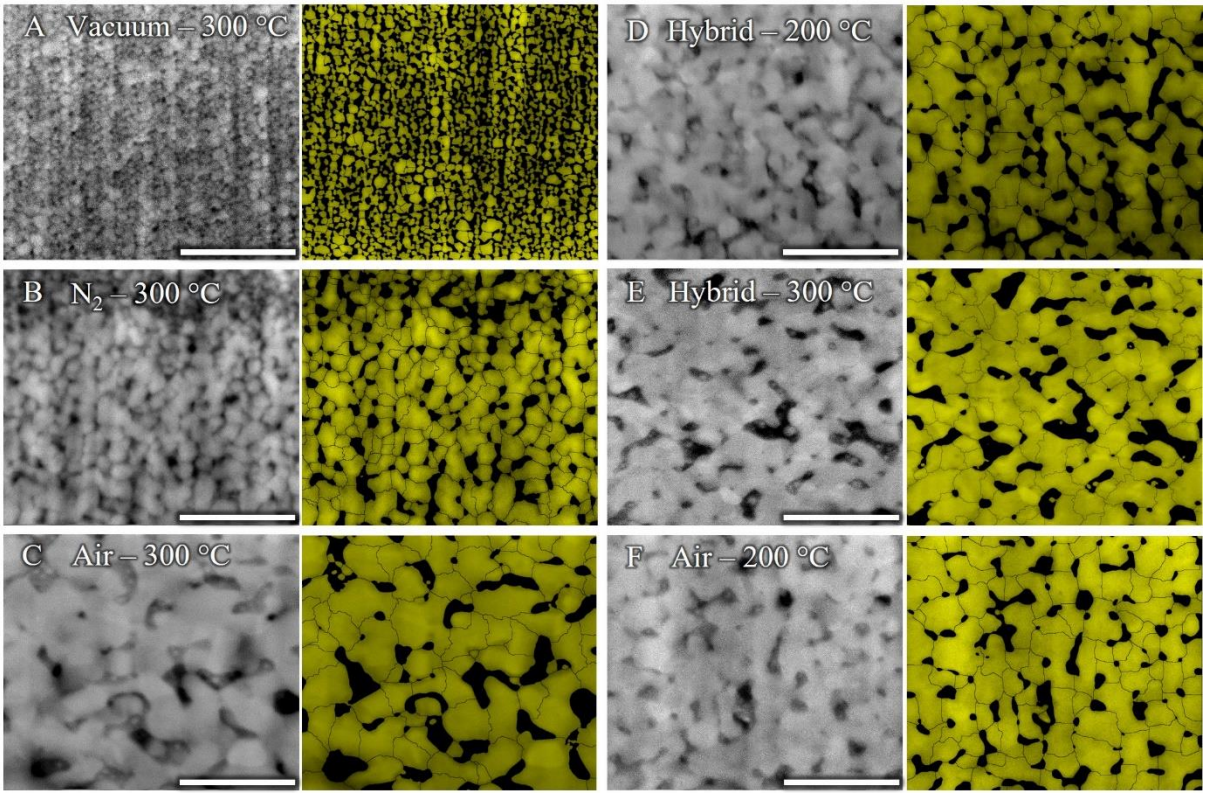

Figure 5.8: Microstructure of various key sintering process conditions and corresponding masks used for image analysis. (A-C) Comparison of different sintering atmospheres up to 300 °C where (A) is vacuum condition (process 2), (B) is N_2 at ambient pressure (process 8), and (C) is air at ambient pressure (process 11). (D-E) Comparison of the (D) hybrid process up to 200 °C (process 15), to the (E) hybrid process up to 300 °C (process 18). (F) The air only condition up to 200 °C (process 13) is shown to compare to (C) and (D). The micrographs have the same magnification and scale bars are all 500 nm.

Figure 5.8D, E, and F show microstructures for samples dried in air (process conditions for experiment #15, #18, and #13 of Table 5.1, respectively). The samples in Figure 5.8D and E are sintered in vacuum at 200 °C and 300 °C, respectively; while the sample in Figure 5.8F is sintered in air at 200 °C. Note that the microstructure of Figure 5.8E is for a sample printed on the PDMS substrate and the others are for samples printed on Si substrate. All the processes shown in Figure 5.8 A-C and F, however, are unable to produce 3D printed interconnects directly on PDMS because the vacuum and N_2 environment causes cracking in the Ag, while air exposure over 200 °C destroys the underlying PDMS substrate. The hybrid air/vacuum processes shown in Figure 5.8D-E are found to be fully compatible with the PDMS and exhibited no cracks, while showing high conductivity and a similar microstructure to the samples sintered under air.

5.3.1 Effect of Ink Composition on Sintering

The effect of different environments on the sintering of Ag NPs was investigated by Lu et al. over a series of publications,[125-127,147] where a silver NP paste was used for chip bonding on a Cu substrate in both reactive and inert environments. They determined that the removal of the organic ligands and binders to promote sintering of the NP was best performed in the presence of oxygen, but a formic acid vapor was also able to catalyze the breakdown of the organics without oxidizing the Cu substrate. In this investigation, the metal NP ink undergoes several steps before becoming electrically conductive as shown in Figure 5.7. The composition of the ink, shown in the inset of Figure 5.7A, is an important factor in determining the conditions under which these steps occur. Typically, metallic nanoparticle inks have a short-chain organic ligand bonded directly to surface of the NPs to aid in the stability of the inks and reduce agglomeration before they are printed. The reduction of surface area can drive sintering

at room temperature if the NPs are able to come in contact with each other; however, the ligands on the surface prevent that from occurring.[113] In addition to the ligands on the NP surface, long-chain polymers called binders are added to the ink to aid in cohesion to suppress cracking and increase adhesion to the substrate. Solvents are then added to reach the desired viscosity for printing; and the ink used in this investigation contains both water and ethylene glycol. A rich and active area of study is optimizing the concentration and chain length of the organic molecules used as ligands and binders in metallic NP inks to reduce the sintering temperature while maintaining the high conductivity and stability of the ink.[118]

The first step after printing metallic NP inks is to remove the solvent by drying as shown in Figure 5.7B. Densification occurs through volume loss as the solvent evaporates and the NPs redistribute. This step is where capillary pressure can cause the cracking described above. The next step is to sinter the NPs to create a conductive film as shown in Figure 5.7C. This happens in several steps as the ligands are removed or displaced and the NP surfaces come in contact and surface diffusion causes coalescence, necking, and finally, grain growth. The thermal treatment provides the energy to drive the entire process and in general, larger grains and higher density requires higher energy.

A thermogravimetric analysis (TGA) is performed on the ink in both air and 101 kPa N_2 environments at 10 °C min^{-1} to investigate the differences in weight loss between the two atmospheric conditions and the results are shown in Figure 5.9. The TGA clearly shows an initial sharp drop in weight of the ink likely due to the evaporation of the solvents (to ~45 wt%). After the sharp initial drop and as temperature rises from ~150 °C to 430 °C, the ink weight in air continues to drop in a linear fashion, which is associated with the decomposition and removal of the organic ligands and binders. This is followed by an increase in weight, which is likely due to the oxidation of Ag. In the N_2 environment, on the other hand, the ink displays

a slow but accelerating weight loss beginning at ~175 °C to 400 °C followed by a linear drop to 800 °C. This data, along with the microstructure seen in Figure 5.8A, B, and C, indicate that oxygen is instrumental for the removal of the organics and is important for sintering of the Ag NPs. The TGA data in Figure 5.9 indicates that the ligand and binder burnout processes begin at approximately 150 °C in air for the ink used in this study. However, the onset of burnout processes varies across different ink compositions and can be as high as 350 °C.[125] The maximum curing temperature for PDMS in air is 150 °C,[58] which informs hypothesis stating that a process window exists where the PDMS substrate may remain undamaged in air and the burnout of organics in the ink can begin to result in high conductivity interconnects.

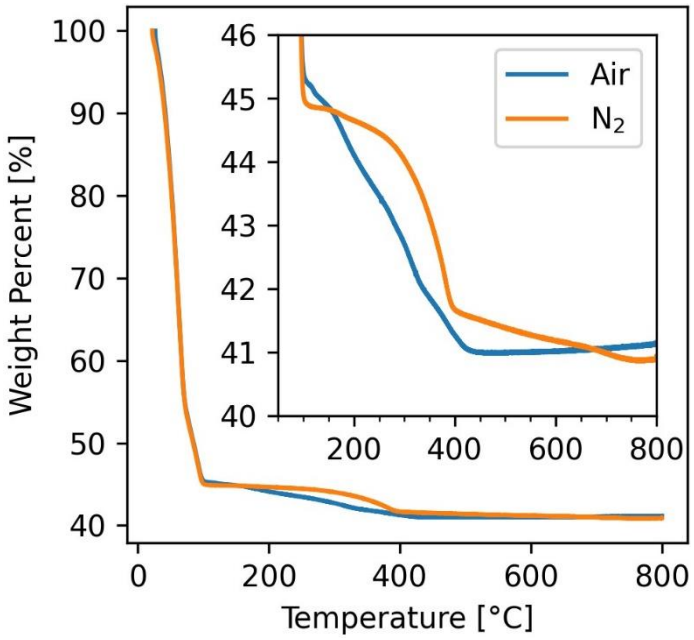

Figure 5.9: Thermogravimetric analysis of silver nanoparticle ink in nitrogen and air The inset graph shows the weight loss of the ink after the solvent has been removed showing the dependance of binder and ligand removal on the sintering environment.

To test the above hypothesis, the maximum drying temperature is increased to 150 °C from 120 °C in air, followed by a high temperature treatment under vacuum to promote further sintering as shown in Figure 5.2B. This initial drying step, performed under air, also has the added benefit of reducing cracking due to the rapid evaporation of solvents under the vacuum

condition (see section 3.1). Process conditions in experiment #14-18 (Table 5.1) use this hybrid sintering technique and can reach conductivities as high as 56 % of bulk Ag when sintered at up to 300 °C (process condition for experiment #14 in Table 5.1). When printed directly onto PDMS under the same condition up to 300 °C (condition for experiment #18 in Table 5.1), the conductivity is 43 % and it is 37 % when sintered up to 200 °C (condition for experiment #17), indicating that the additional layer of PDMS affects the conductivity. Furthermore, there is an increase in conductivity from 25 % to 37 % of bulk Ag when the ramp rate to maximum temperature is decreased from 5 °C min^{-1} to 0.5 °C min^{-1}, indicating that increased time at sintering temperatures results in higher conductivity, which has been noted in previous studies.[109,148] Process conditions of experiments #12 and #13 in Table 5.1 comprised drying and sintering in air up to 200 °C and have very high conductivities up to 64 %, which is comparable to air sintering up to 300 °C (which is 67 %). Previous studies have reported a retention of stretchability of PDMS after exposure to 200 °C in air with a slight reduction in the maximum strain that the PDMS can withstand.[72] However, cracking in the PDMS was observed in our samples cured in air up to 200 °C (same as process conditions in experiment #12 and #13 in Table 5.1). A similar trend is shown in Chapter 3, where PDMS remains stretchable after thermal treatment in vacuum up to 300 °C but shows a decrease in maximum strain before failure compared to PDMS taken to 200 °C under vacuum. Therefore, an engineering tradeoff continues to exist between high conductivity of the sintered interconnect and retention of stretchability of the substrate, but the hybrid processes (#14-18 in Table 5.1) described in this chapter extend the process boundaries to achieve high conductivity traces with 3D features printed directly onto a stretchable substrate.

5.3.2 Modeling Electrical Conductivity with Microstructure Data

The microstructures of the printed silver interconnects shown in Figure 5.8A-C show increased necking and particle coalescence with sintering in vacuum, in N_2 at atmospheric pressure, and air at atmospheric pressure. The conductivities of the samples with microstructures shown in Figure 5.8A-F are given in Table 5.2. Several methods have been developed to predict the conductivity of porous solids based on microstructural characteristics. Maxwell's effective medium theory and Bruggeman's correlation may be the most widely used models as they employ only the relatively simple measurement of volume fraction of the material to determine the effective conductivity relative to the bulk material properties.[149] However, with availability of additional data such as the tortuosity of the conducting phase or grain size of the crystalline solid, more detailed models can be used. Rosker et al.[150] recently proposed a multiscale model that modified Maxwell's effective medium theory to include grain boundary scattering and gives,

$$\frac{\kappa_{eff}}{\kappa_{bulk}} = \frac{\lambda_{gb}}{\lambda_0 + \lambda_{gb}}\left(\frac{2\phi}{3-\phi}\right) \qquad 5.4$$

where κ_{eff} is the effective conductivity, κ_{bulk} is the bulk conductivity (6.3×10^7 S m^{-1} for silver), λ_0 is the mean free path of an electron in the conductor (53 nm at 300 K for silver), ϕ is the volume fraction described above, and λ_{gb} is the characteristic line of sight distance for an electron moving across a grain in the ballistic transport regime. The characteristic line of sight is determined by the average length to cross the grain, and we follow the procedure by Rosker to approximate grains as spheres and use the average chord length of a sphere as λ_{gb}. The microstructure images in Figure 5.8 are analyzed with ImageJ[135] software by thresholding and water shedding to determine individual grains and are shown as the yellow mask images in

Figure 5.8. The 'analyze particles' function in ImageJ is then able to return the volume fraction, grain area, and perimeter.

In addition to using the multiscale model, conductivity is modeled using the standard definition for the tortuosity factor, τ, using the following relationship,[151]

$$\frac{\kappa_{eff}}{\kappa_{bulk}} = \frac{\phi}{\tau} \qquad 5.5$$

The tortuosity factor is determined using TauFactor[136] with the same mask images in Figure 5.8 without the grain boundary lines, averaged over both horizontal and vertical directions in multiple areas of the image. The tortuosity measurement results in the same tortuosity factor that can be determined from Bruggeman's correlation, which is not independent of volume fraction.

Table 5.2: Results of microstructure image analysis and comparison of measured conductivity to the microscale conductivity model, and tortuosity model.

Process Description and Number		Volume Fraction		Characteristic Length		Tortuosity Factor			Multiscale Model Conductivity		Tortuosity Model Conductivity		Measured Conductivity	
[-]	[-]	[%]	std dev	[nm]	std dev	[-]	std dev		[%] of bulk Ag	std dev	[%] of bulk Ag	std dev	[%] of bulk Ag	std dev
Vacuum - 300 °C	2	61	±9	15	±4	10	±5		12	±4	6.2	±3	0.28	±0.02
N_2 - 300 °C	8	84	±2	35	±12	1.5	±0.1		31	±10	56	±4	16	±7
Air - 300 °C	11	82	±1	67	±21	1.45	±0.07		42	±13	57	±3	67	±2
Hybrid - 200 °C	15	82	±2	50	±17	1.64	±0.04		37	±12	50	±2	39	±1
Hybrid - 300 °C	18	83	±1	50	±16	1.42	±0.11		37	±12	58	±5	43	±5
Air - 200 °C	13	87	±2	57	±15	1.35	±0.04		42	±11	64	±2	59	±5

The effective interconnect conductivity is determined utilizing both methods described in Equation 5.4 and 5.5 and compared against the measured conductivity. The full results are detailed in Table 5.2. The model results in Table 5.2 show that both the multiscale model and the tortuosity factor model overpredict the conductivity for samples sintered under vacuum and 101 kPa N_2 environments, while the air sintered sample is underpredicted by both the models.

The microstructure images for samples sintered under vacuum and N_2 environments in Figure 5.8 show more individual rounded particles rather than the porous, but continuous, grain structure similar to the air-sintered sample. The lack of necking between particles could be due to the remaining ligands and binders in the microstructure, preventing further sintering of the particles, which presents an additional scattering mechanism that is not captured by either model and may explain the overpredicted conductivity of the vacuum and N_2 sintered samples. The air sintered sample, on the other hand, is underpredicted by both the models, but the tortuosity model (57 % of bulk Ag) is closer to the measured conductivity (67 % of the bulk) compared to the multiscale model, which predicts an interconnect conductivity of only 42 % of bulk Ag. This less accurate prediction by the multiscale model may be due to the assumption of spherical particle shape made in both the microscale and macroscale sections of the model, whereas the tortuosity factor is numerically determined directly from the microstructure. The hybrid air/vacuum sintering process falls in between the predicted conductivity of the multiscale and tortuosity models and is within a standard deviation of the multiscale model as shown by Table 5.2. The correlation between porosity and conduction have been known and investigated for many years, yet an accurate general model is still an elusive goal of active research in the battery, fuel cell, and geology communities.[149] Despite the large discrepancies between predicted values and measured values of conductivity, the trend of increasing conductivity with increasing grain sizes and decreasing porosity and tortuosity is captured by both models, indicating a dependence of the conductivity on the microstructure.

5.4 Shear Test of Three-Dimensional Pillars

The strength and reliability of the 3D printed pillars are important in practical applications involving use as VIAs where bending and stretching of the device may result in transverse

loads on the pillar. The shear test apparatus shown in Figure 5.3 is used to investigate the transverse force that the pillars can withstand before failure. Both hollow circular and tapered pillar geometries are tested. In addition to testing both pillar types, the process conditions that resulted in cracking at the pillar base (vacuum and N_2) and crack-free pillars (air and hybrid) are also evaluated. The maximum force applied prior to failure during the shear test for both geometries fabricated under each process condition is shown in Figure 5.10. Clearly, the samples dried and sintered in vacuum were weakest with lowest failure force of only: 0.08 N for the tapered pillar, and only 0.012 N for the circular pillar. The reason for the lower failure force for this process condition is likely to be the presence of cracks underneath the pillars (Figure 5.4D and Figure 5.5D). The air and hybrid process conditions reach a higher failure force of 0.242 and 0.243 N, respectively, for the circular pillars, and 0.162 and 0.150 N, respectively, for the taper pillars.

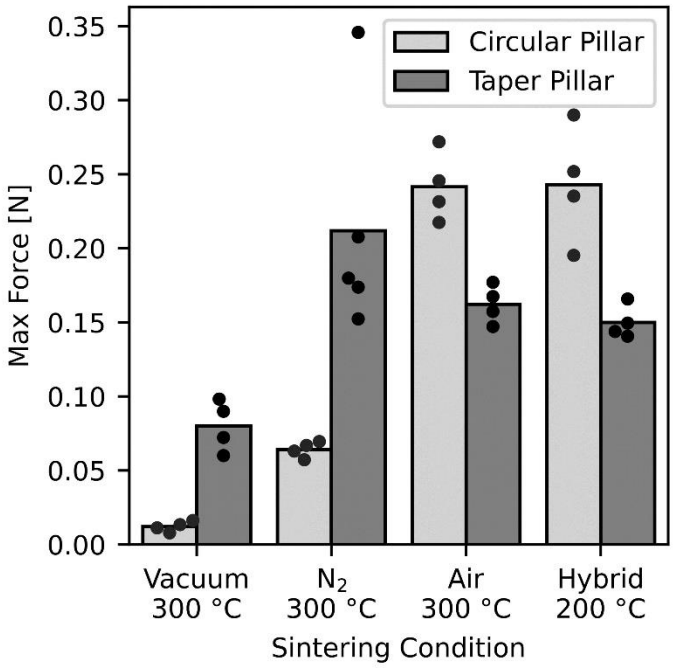

Figure 5.10: Maximum force applied to pillars prior to failure. Both the circular pillar and taper pillar geometries are tested for the sintering conditions shown.

The post failure SEM images for the hollow pillars in Figure 5.11A show a difference in failure mode between the pillars fabricated under vacuum and N_2 environments (with underlying cracks) where sections of the Ag pad underneath the pillar remain. This contrasts with the pillars fabricated in air and hybrid conditions, where the entire pillar and pad were removed indicating that failure occurred at the interface of PI and Ag pad rather than within the Ag structure. The taper pillar displays the same behavior for the vacuum process where portions of the Ag pad remain, but for the N_2, air, and hybrid environment, the failure is a mixture of the pad interface layer and the Ag pillar.

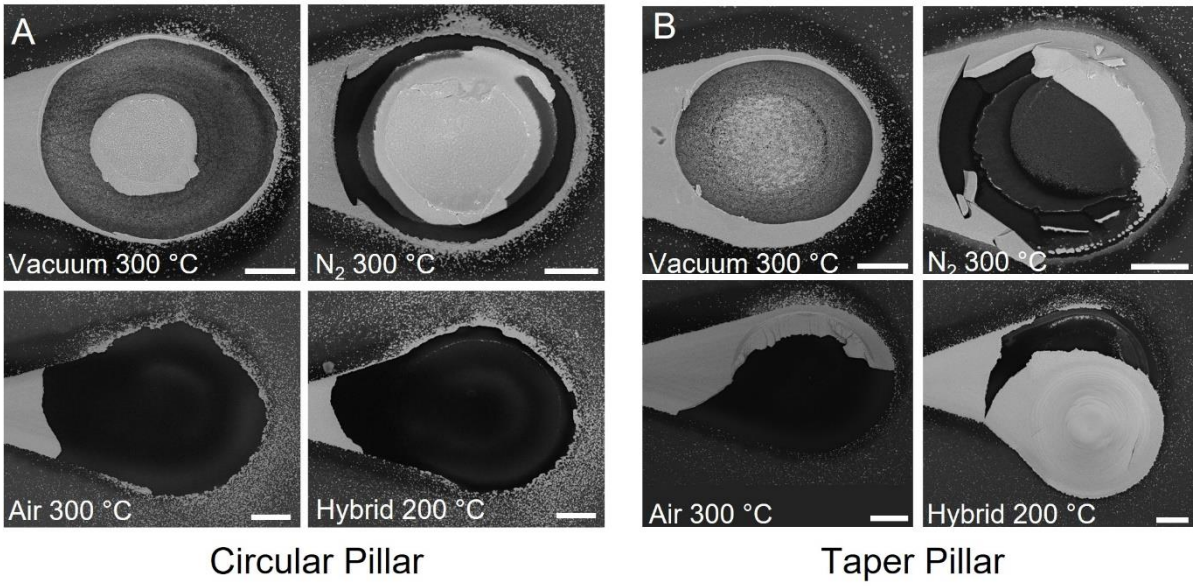

Figure 5.11: Post-failure images of both the circular and taper pillar geometries. Images from the scanning electron microscope of the (A) circular pillar failure surfaces and (B) taper pillar failure surfaces are shown for the same conditions shown in the previous graph. Scale bars are 50 μm.

A stress analysis for the compatible hybrid process to compare the stress developed with the applied load is done at three locations including the maximum bending stress location, and maximum transverse shear stress locations and shown in Figure 5.12. Location number 1 represents the largest normal stress due to bending, and location 2 and 3 represent the largest transverse shear stress locations. The normal and shear stresses are compared using the

equivalent or von-Mises stress, and the transverse shear stress at location 3 results in the highest stress as shown in Figure 5.12C. The failure location involves the interface between the silver and the polyimide, and there is a significant crack present in the case of the vacuum and N_2 environments so the stress at interface (location 1 and 2 in Figure 5.12A) is relevant. The failure stress should be similar, but the hollow pillar shows significantly higher stress for both the normal stress due to bending, and the transverse shear stress. The significantly smaller failure stress in the taper pillar indicates that the simple cantilever beam model may not capture all stresses involved or critical failure points. One hypothesis is that there is residual stress in the pillar from differences in thermal expansion, and that the residual stress in the solid taper pillar is larger than the hollow pillar, but additional analysis is required to test the hypothesis.

A

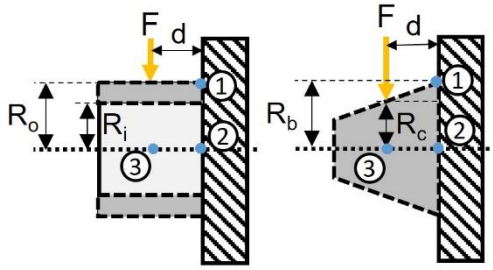

B

	[µm]	Std. Dev.
Taper Pillar		
Base Radius (R_b)	92.2	±0.9
Contact Radius (R_c)	71.2	±0.8
Circular Pillar		
Inner Radius (R_i)	88.6	±0.8
Outer Radius (R_o)	111	±2
Force Distance		
Pillar Base to Contact Point (d)	58	±3

C

	von-Mises stress, Hybrid - 200 °C			
Location	**Circular Pillar [MPa]**		**Taper Pillar [MPa]**	
1	21.6	±3.3	14.2	±1.2
2	58.0	±8.9	13.0	±1.1
3	58.0	±8.9	21.7	±1.9

Figure 5.12: Pillar stress analysis of shear test for the hybrid process condition. The cantilever beam model schematic (A) shows the dimensional locations detailed in (B), and the three blue numbered locations where the equivalent von-Mises stress was determined and detailed in (C).

The hybrid sintering process to 200 °C shows a very similar mechanical response in the pillars compared to the air sintering process at 300 °C for both the circular and taper pillar geometries and survives stresses near the yield stress of bulk silver in the case of the circular pillar geometry. The circular pillar geometry can withstand higher applied force under the

compatible hybrid process condition compared to the taper pillar but is more sensitive to cracking at the base (i.e., when processed in vacuum or N_2).

5.5 Three-Dimensional Pillars for Packaging of Fully Encapsulated Interconnects

Pillars allow for connections to external circuitry or direct contact to skin, for example to be used as an electrode for health monitoring applications. As described in the fabrication section, Dynasolve was used for a timed wet etch of the residual PDMS film covering the tips of the pillars after spin coating. The measured etch rate was 0.5 ± 0.2 μm s^{-1} tested across four samples. Images of exposed pillar tips after etching, along with profilometer and resistance plots are shown in Figure 5.13. An SEM of each of the hollow and tapered pillars after the etch step are shown in Figure 5.13A for the hollow pillar and Figure 5.13B for the tapered pillar. The pillars shown in Figure 5.1(A-B) are between 150 - 200 μm tall, while the bottom and top layers of PDMS are each around 30 μm thick, resulting in a total PDMS thickness of 60 μm. This would leave around 90 – 140 μm of the tips of the pillars above the PDMS encapsulation. However, the uncured PDMS is spin-cast onto the substrate and its viscosity creates a meniscus in the PDMS from the pillar towards the flat plane of the substrate. Stylus profilometer scans for both the hollow and tapered pillar were performed in Figure 5.13B and Figure 5.13D. For the hollow pillar (Figure 5.13B), approximately 25 μm of the tip of the pillar appears to be exposed from the top layer of PDMS with the meniscus occurring across 75 % of the height of the pillar. Similarly, for the profilometer scan of the tapered pillar (Figure 5.13D), 20 – 40 μm of the tip of the pillar is exposed from the top layer of PDMS, and again there is a meniscus occurring across 75 % of the height of the pillar.

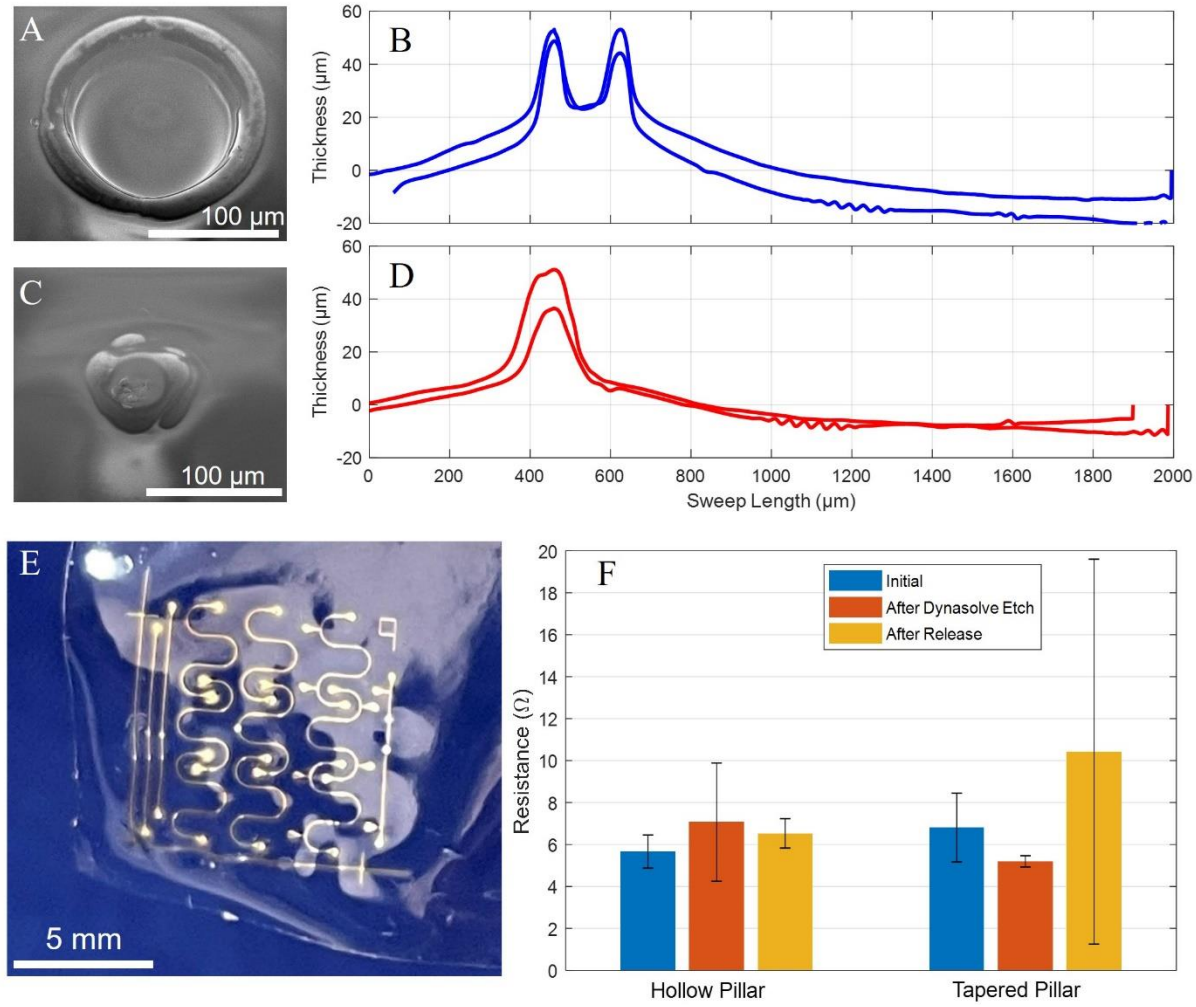

Figure 5.13: Interconnect encapsulation in PDMS and release from handle substrate. (A) SEM image of encapsulated straight hollow pillar and (C) taper full pillar with the tip exposed after the Dynasolve etching step to remove the thin top layer of PDMS. Profile scan of the exposed (B) straight hollow pillar and (D) taper full pillar showing approximately 30 µm height of exposed silver extending from the PDMS to make electrical connection (E) Released sample with retained flexibility, and (F) Resistance measurements throughout process steps. Resistance is measured from pillar to pillar, and exposed pillar tips are shown in (A) and (C).

Figure 5.13F represents measurements of the average of the resistance across each of the hollow and tapered pillars for samples with experimental condition #17 in Table 5.1, which includes a PAA release layer, along with Ag traces insulated with PI and fully encapsulated in PDMS. The error bars represent one standard deviation apart from the average across four traces. A first resistance measurement is taken after sintering the Ag and curing the top layer of PI. Further resistance measurements are taken after spin-casting the top layer of PDMS and

etching the PDMS residue above the pillars with Dynasolve. And lastly, the resistance is measured after releasing the sample by using saline to dissolve the PAA release layer (shown in Figure 5.13E). The test structures required two-point resistance measurements. Overall, the resistance values remained consistent across each of the fabrication steps with some variability due to inconsistent probe placement across the tops of the pillars and uneven placement of the sample.

The final released sample is shown in Figure 5.13E. We note a mismatch in the treatment for the bottom and the top layer of PDMS in the interconnect system. The bottom layer of PDMS undergoes several high temperature thermal treatments for curing PI and sintering the Ag layers, while the top layer of PDMS experiences a curing treatment and a short drying step after Dynasolve etching, both at 100 °C. As a result, in stretching applications, the bottom and top layers of PDMS are expected to have different elastic moduli and maximum strain-to-failure. The bonding between the top and bottom PDMS layer was tested using ASTM D3359 Tape Adhesion Test standard (see experimental methods section 5.1.3). Despite the differences in the thermal histories of the two PDMS layers, no delamination was observed during the adhesion test as seen in Figure 5.14.

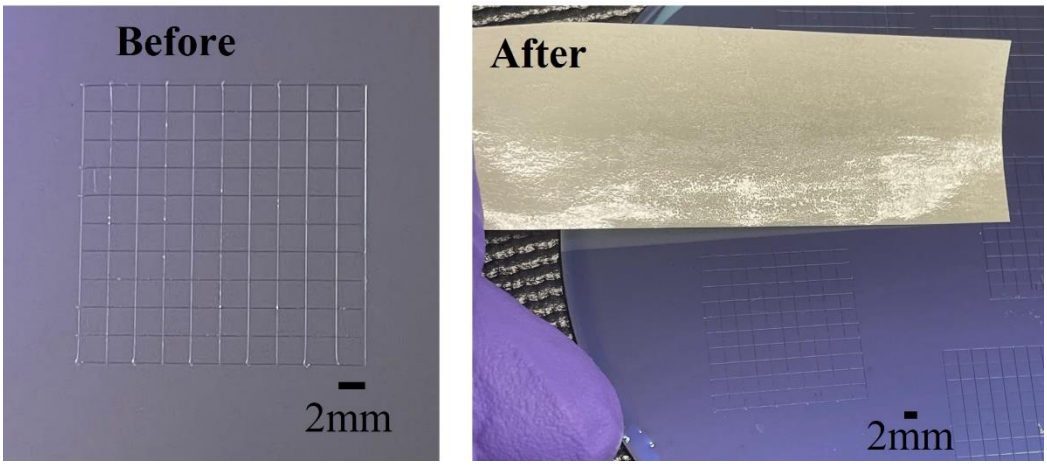

Figure 5.14: ASTM D3359 Tape Adhesion Test Results for PDMS layers. Shows before and after images from sample 1 of the test along with the tape after the test, which shows no remnants of the top PDMS layer being removed from the bottom PDMS layer following Test Method B guidelines for materials 50-125 μm thick.

5.6 Conclusions

The vacuum sintering process initially showed promise as a path to achieve high temperature sintering without damaging the stretchable PDMS substrate (developed in Chapter 3) but displayed unacceptable drawbacks in causing both cracking and low conductivity in the sintered silver interconnect traces. A hybrid sintering process including a drying step conducted in air up to 150 °C, followed by a high temperature treatment in vacuum is shown in this chapter to preserve the stretchable substrate, while producing crack-free and highly conductive 3D interconnects up to 56 % of bulk Ag. Dry nitrogen and vacuum environments are shown to produce cracking during drying due to increased inter-particle capillary force from rapid solvent evaporation. Additionally, organic ligands and binders present in Ag nanoparticle inks are shown to be removed more effectively in air at temperatures of 150 °C and above relative to an inert N_2 environment. The microstructure differences and increased conductivity of interconnects sintered under air relative to N_2 and vacuum environments further evidences the removal of the organics in the ink to be the cause of lower conductivity. A hybrid thermal process is developed where the low-temperature air drying step reduces the capillary force that initiates cracks. The air-drying step to 150 °C also increases the removal of the organics in the Ag nanoparticle ink prior to the high-temperature sintering step under vacuum, which increases the conductivity while preserving elastic characteristics of the underlying PDMS. This process development enables 3D pillars to be integrated into the embedded interconnect and extend through the PDMS layer to interface with external components or additional layers of circuitry. Additionally, the process is compatible with low temperature solder (which uses temperatures well below the thermal treatment profile peaking at 200 °C), silver paste or paint, or conductive tape.

Chapter 6

Electrocardiogram Recording via 3D Stretchable Dual-Layer Sensor Patch

Wearable devices, like smart watches, have recently become commonplace with the ability to capture biopotential signals from the skin that originate from the heart (electrocardiogram, ECG), brain (electroencephalogram, EEG) and muscle groups (electromyography EMG).[61] Achieving good contact between the skin and the electrode of the device is crucial to the quality of the signal, and represents the main drawback to the commonly used metal electrodes which are unable to conform or stretch along with the skin. Several methods to improve the compliance and contact of the electrode include using flexible micropillar arrays,[152-154] adhesive and conductive hydrogels,[155] intrinsically conductive polymers,[156] composites of soft elastomers with conductive fillers,[157] and thin serpentine metal films.[4,93,158,159] One challenge with using serpentine metal films is the ability to connect the external connection or signal processing electronics with the contact electrode. This chapter presents a multi-layer printing method to facilitate the electrical connection through a soft PDMS layer from the skin contact electrode to a fully embedded electrical interconnect which can be connected to other components.

Multi-layered stretchable electronic devices not only enable connection to contact electrodes but can also increase the functional density of electronic devices. While soft transistors have been fabricated, high performance and microscale components still rely on

very stiff semi-conductor materials which are difficult to package in a stretchable device.[25] Strain islands are successfully used to integrate these stiff components, but in a single layer device, the area available to place the components is limited since there needs to be stretchable areas to accommodate the globally applied strain (100% coverage with stiff strain islands results in a non-stretchable device).[7,8] Multi-layered designs allow for several stiff components to be stacked on one another and reduce the areal footprint enabling highly stretchable and complex devices. However, vertical interconnect accesses (VIAs) typically used in rigid circuit boards, remain non-trivial to introduce into stretchable electronics.[42]

Recently, there have been several reports of techniques to introduce multi-layered stretchable circuit designs. Most commonly, holes are created in the elastomer or insulating material and then filled with conductive material to allow for connection between layers. These holes have been created by physical cutting,[160] using photolithography to pattern sacrificial molds,[161] or using laser ablation,[162,163] and the holes can then be filled with silver paste,[160] liquid metal,[163] anisotropic metal deposition,[161] electrodeposited Cu,[42] or solder.[162] Another method used to create highly functional devices is to fabricate each layer on a mesh structure, transfer each layer on top of each other, and insert silver pillars between layers and solder in place.[164] However, these methods are often complex and time consuming, and additively manufacturing techniques can greatly simplify the process. Multi-layered printing (without VIAs) has been demonstrated using aerosol jet, ink jet, screen and extrusion printing.[165-168] Aerosol jet printing has the ability to fabricate pillars over several millimeters tall, at a high density.[36,168] 3D printed pillars have been fabricated and later encapsulated by elastomer with the tips exposed to enable VIA connection between stretchable layers using electrohydrodynamic (EHD) and aerosol jet printing, which is described in Chapter 5.[57,169]

The scope of this chapter is two-fold; first is to mechanically characterize the fully embedded interconnect, and second is to use the same printing method to demonstrate a thin, skin-wearable electrode capable of recording an ECG signal. The fully embedded interconnect is tensile tested under strain to fail and cyclical testing to characterize the stretchability for use in skin wearable devices. Following the stretchability tests, two prototypes of an ECG patch are fabricated, and the impedance from one electrode to another through the skin is measured to characterize electrical performance. Finally, ECG recordings are recorded using the multi-level printing method enabled by 3D printed VIAs and compared against commercially available electrodes.

6.1 Experimental Method

Electrical VIAs are fabricated directly on PDMS following the final process described in the fabrication section 2.2. With the pillar tips exposed, the VIA printing process is completed by printing additional layers of PI and silver nanoparticle ink for the second prototype of the ECG patch as shown in Figure 2.4. To connect to the pillar or VIA, the polyimide is first printed across a portion of the pillar as shown in Figure 2.4B. This forms a bridge between the soft stretchable PDMS and the stiff silver pillar and prevents cracks that form at the interface when the base polyimide layer is not included. Then, the next silver layer is printed on the PI layer and connected to the VIA by printing directly on the exposed silver pillar as shown in Figure 2.4C. This same process is depicted in Figure 6.3A in three dimensions for clarity.

The tensile tests are conducted while simultaneously measuring resistance of the interconnect during sample stretching. Both strain to failure and cyclical strain tests are performed. The strain rate is 1% strain/s for the strain to failure tests, and 10% strain/s for the cycle tests. The failure strain is recorded as the point at which the interconnect resistance is

measured as an open circuit. A four-point probe resistance measurement (Keysight 34470A, Keysight Electronics Company, Santa Rosa, California) of the interconnect under tensile strain is taken using the external connection points facilitated by the exposed pillars as shown in Figure 2.3B. A universal testing machine (Instron 5969, Norwood, MA) is used to capture extension and force. Engineering strain in the testing region is determined by a strain correction value determined in Chapter 3, and the engineering stress is determined by the cross-sectional area of the PDMS that encapsulates the trace (6 mm x 0.12 mm).

The strain correction factor, m, described by Equation 3.1 is also used to capture the normalized change in resistance of the test region. The measured resistance, R_m, of the embedded interconnect measures the resistance of the entire meander length, L_m, which is 36 mm and shown in Figure 6.1A. This includes a section exterior to the clamp that are completely unstrained, and the transition region which experiences less strain than the test section, which is 10 mm and shown in Figure 6.1A. The change in resistance in the high strain test region is of interest and can be found using the strain correction factor and the measured resistance. The initial resistance of the individual sections are scalers of the initial test section resistance, $R_{0,t}$. The scaler quantity is then the ratio of the length of the section divided by the length of the test sample region, L_t. An assumption that the change in resistance per initial resistance of each section is linearly proportional to the strain is made and shown explicitly for the test section as

$$\frac{\Delta R_t}{R_{0,t}} = C\varepsilon_t \tag{6.1}$$

where C is a constant that is the same for each section, and ε_t is the elastic strain in the test section. This assumption is valid for elastic strain regions, and when comparing between sections with close – but not the same – strains. The strain in each section can then be written

relative to the test section strain, which causes the C factor to drop out. By recognizing that the strain correction factor described by Equation 3.1 is a ratio of the change in length of the test region to the change in length of the clamped region, the change in electrical resistance in the test region can be found from the measured electrical resistance. This relationship is

$$\frac{\Delta R_t}{R_{0,t}} = \frac{mL_m}{L_t}\left(\frac{\Delta R_m}{R_{0,m}}\right) \tag{6.2}$$

and the change in resistance of only the higher strain test region can be determined from the total measured resistance of the meander.

For the resistance and impedance measurements, external connections are achieved by placing electrically conductive silicone (SS-25S, Silicone Solutions, Cuyahoga Falls, Ohio) on top of the four pillars placed in a cross formation (four on the dogbone sample shown in Figure 6.1A and one on the multi-layered skin-wearable patch shown in Figure 6.3E) followed by a conductive aluminum tape (16071 Aluminum tape, Ted Pella, Redding, CA). During tensile tests, these external connections are outside of the clamped region during the tensile tests to ensure that the strain measurements capture the embedded meandered interconnect rather than the strain around the external connections. Additionally, during EIS and ECG measurements, electrically insulating tape is placed on the skin directly under the external connections to ensure measured values represent the patch rather than the external connections.

The electrocardiogram (ECG) is captured from a standard bipolar lead I configuration which is where the recording electrodes are placed on the left and right arms. A driven electrode (i.e., to reduce the common-mode voltage) is placed on the left wrist and the recording electrodes are placed on the forearm. Skin is prepared for application by cleaning with soap followed by IPA wipe to remove any leftover residue. A single lead heart rate monitor (AD8232, SparkFun Electronics, Niwot, Colorado) is used to capture an analog signal which

is converted to a digital signal and recorded on a laptop computer. Commercial electrodes (Red Dot 3M, Saint Paul, MN) and (5400 Tab Electrodes, Cardinal Health, Dublin, Ohio) are used to compare with the ECG signals and skin impedance from the 3D printed electrodes. Impedance from electrode to electrode (at a distance of 6 cm on the arm) are captured using electrical impedance spectroscopy (EIS) (Metrohm Autolab, Netherlands) at frequencies ranging from 1 to 10^5 Hz with the same skin preparation as is used for the ECG recording. All biological measurements presented in this chapter were recorded on the same test subject.

6.2 Tensile Testing of 3D Interconnect

The stretchability of the 3D electrical interconnects printed via aerosol jet and fully embedded in PDMS are characterized with a tensile test of dogbone samples while simultaneously recording the electrical resistance. The dogbone shape is the same as the one tested in Chapter 3, and is shown in Figure 6.1A. The pillars with exposed tips facilitate external connection to the interconnect, and the four-point probe resistance of the interconnect is measured during the tensile tests. The meandering silver interconnect is encapsulated by the polyimide and the geometry of the interconnect is also shown in Figure 6.1A where the width of the polyimide layer w is 160 µm, the radius of curvature for the meander, r, is 500 µm, and the meander angle, θ, is varied between tests. Previous testing on samples from Chapter 4 indicated that the meander angle influenced the maximum failure strain and that angles between 180° and 270° would result in the highest strain to failure.[170] To narrow the parameter spread, three meander angles are fabricated including 180°, 210°, and 240° to investigate the effects on strain to failure and cyclical testing.

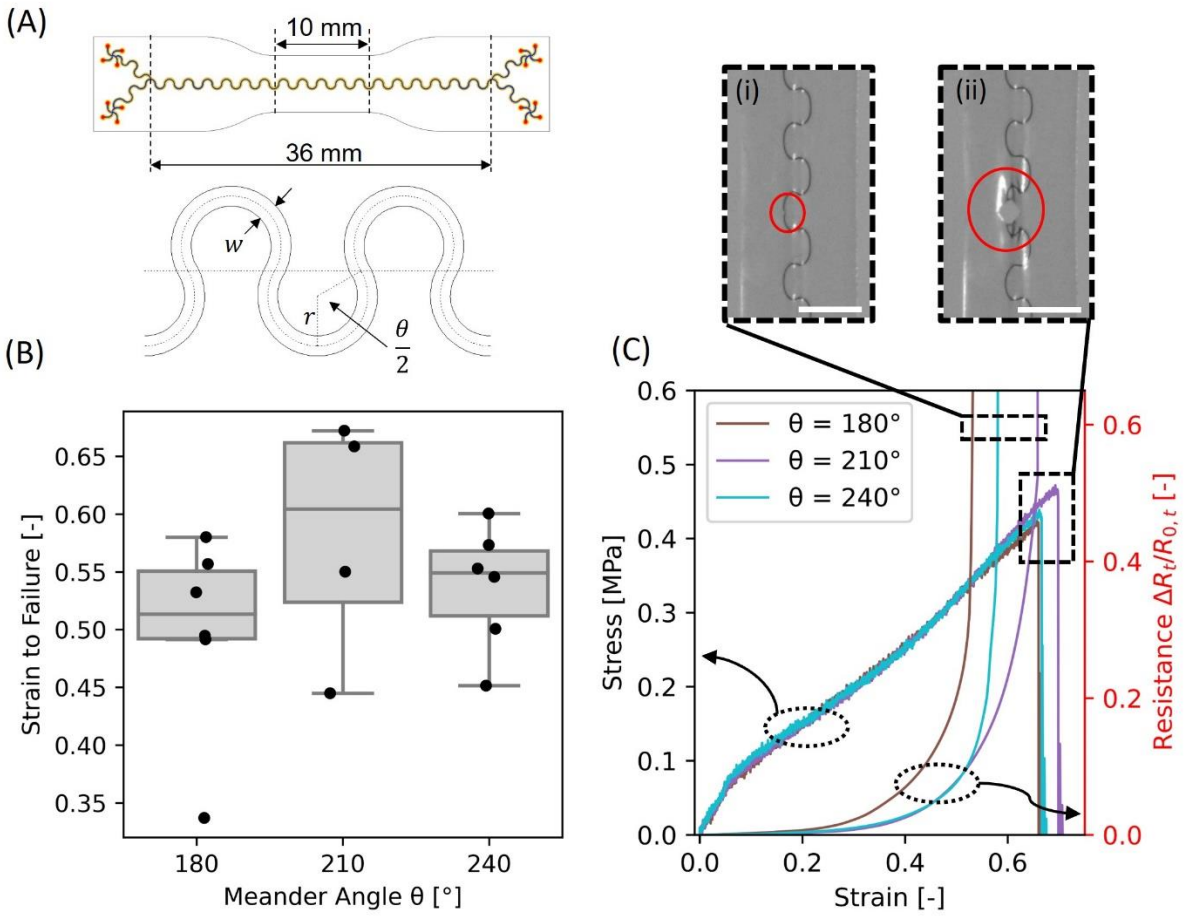

Figure 6.1: Tensile testing of fully embedded interconnect for three meander angles. (A) The shape of the dogbone sample is shown along with the dimensions of the meandering interconnect. (B) The strain to failure point (electrical disconnection) is plotted for three different meander angles (180, 210, and 240). The combined stress-strain plot along with the normalized change in resistance for three of the representative samples are shown in (C) with the inset images showing the (i) interconnect failure at electrical disconnection and (ii) just prior to complete PDMS mechanical failure. Scale bars are 3mm for inset images.

6.2.1 Strain to Failure

The tensile tests were conducted for each of the meander angles and the results are shown in Figure 6.1B. The 210° meander angle has the highest average strain to failure value of 58.1% followed by the 240° and 180° with strain to failure of 53.7% and 49.9%, respectively. A one-way analysis of variance (ANOVA) reveals, however, that there is no statistically significant difference in the mean strain to failure for the varied meander angles ($p = 0.32$). One reason for this lack of difference in failure strain may be due to the change in meander angle is too

small (i.e., larger differences in meander angles may reveal larger differences in failure strains). Despite the lack of difference for the strain to failure, the mean strain to failure of all the samples combined is 53.4% which is well above the 15% elastic strain limit of skin.[61]

Three representative data sets for each meander angle are shown in Figure 6.1C. The engineering stress/strain response for each sample is nearly identical, indicating that the PDMS properties, rather than the meander angle, dominated the mechanical response. The change in resistance of the test section for each sample is normalized by the initial resistance of the interconnect test section and plotted on the secondary y-axis. The resistance has a stable region characterized by a slight linear increase in resistance at low strain (< 20%), followed by progressively increasing resistance with increasing strain. Using a high-speed camera (NOVA S-Series, Photron, Tokyo, Japan) the failure initiation was captured and shown to be originating in the meandering interconnect and not the PDMS. This is captured in the data by the instantaneous rise in resistivity shown in Figure 6.1C and the first inset image captures the failure initiation in the interconnect. Then, the complete mechanical rupture of the interconnect and PDMS occurs later and is captured by the drop off in applied force on the sample and the second inset image of Figure 6.1C.

6.2.2 Cyclical Testing

The cyclical stability of the interconnect is characterized by utilizing the same sample geometry in Figure 6.1A and cycling between 0% and 30% strain at a rate of 10% strain/s. Figure 6.2 shows the mechanical stress/strain and the normalized change in electrical resistance results for one of the 210° meander angle samples. The first 5 cycles and the 1000th cycle data is shown in Figure 6.2 inset graph, and the mechanical response appears unchanged, while the electrical resistance increases. The change in resistance over 1000 cycles is quite small,

approximately 1% change in permanent resistance. The permanent change in resistance can be seen in the first five cycles in Figure 6.2, which indicates the occurrence of plastic deformation in the silver interconnect when stretched to 30% strain. This is followed by a more gradual increase in resistance throughout the cycling test.

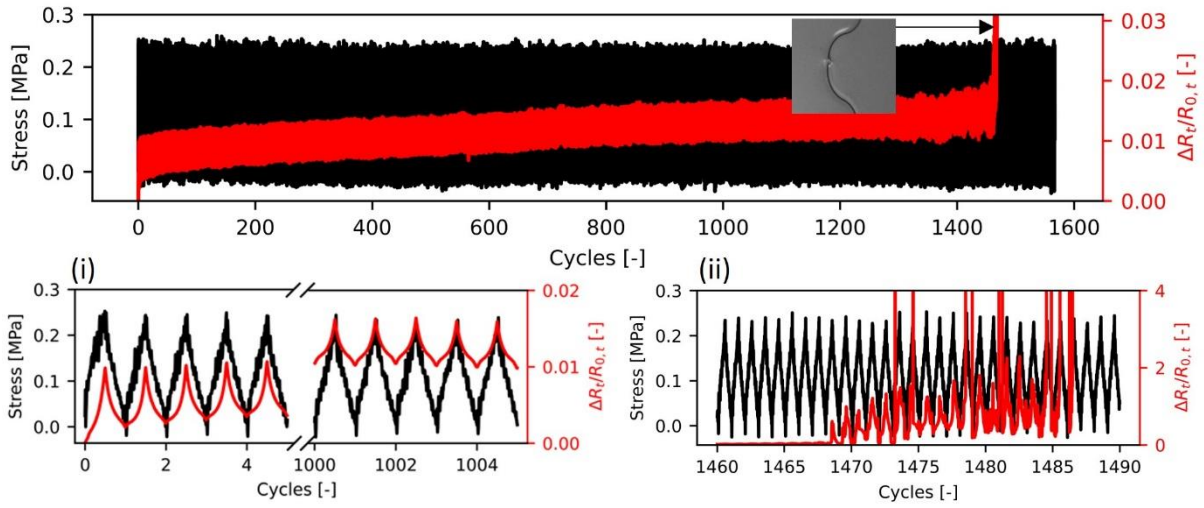

Figure 6.2: Cyclic loading to 30% strain on a 210° meander angle sample. Stress and resistance data under mechanical cycling with an inset image of the failure location. The initial five cycles and after 1000 cycles are shown in more detail in the inset graph (i) where the stress scale is the same and the normalized change in resistance is rescaled. The detail of the cycle data leading to the failure of the interconnect is shown in (ii) with a rescaled normalized change in resistance.

The progressive increase in resistance to failure is seen over 20 cycles in Figure 6.2 in the second inset graph, where the final failure cycle is 1486 for this sample. The 210° meander sample shown in Figure 6.2 represents the highest number of cycles to failure tested, followed by a 240° sample and 180° sample surviving 1080, and 446 cycles, respectively. Chronically worn ECG recording devices, such as Holter monitors, are worn for approximately 30 days, and accumulating 1000 cycles at extreme strain (i.e., above the 15% elastic strain limit of skin) during that timeframe is unlikely and indicates that the interconnect stretchability is suitable for wearable devices.

6.3 Dual Layer Sensor Patch

An initial prototype ECG sensor patch or electrode shown in Figure 6.3B-C is tested first using only the pillar tips to contact the skin. The targeted contact of the pillar tips was thought to create an intimate contact with the skin. However, the resulting impedance is shown in Figure 6.4 to increase almost an order of magnitude when replacing only one of the electrodes on the skin compared to two commercial electrodes. The leading hypothesis for the significant increase in impedance observed is that there is insufficient contact area provided by the exposed pillar tips because the resistance is inversely proportional to the contact area. To test this hypothesis, a second prototype is designed to increase the surface contact area of the electrode on the skin. The dual-layered ECG sensor patch is shown in Figure 6.3D-E and fabricated using the VIA printing process using the final two fabrication steps in Figure 6.3. The silver electrode is a meandering mesh on the surface of the multi-layered patch, and directly contacts the skin in a stretchable interface. To increase the surface area of the electrode, the meanders consist of four side-by-side printed lines to provide 36 mm^2 of contact area compared to the 0.25 mm^2 using only the pillar tips in the first prototype. The skin contact electrode is connected to the embedded interconnect using the VIA resulting in a dual layer patch that also demonstrates the ability to connect an additional printed layer to the exposed pillar tip.

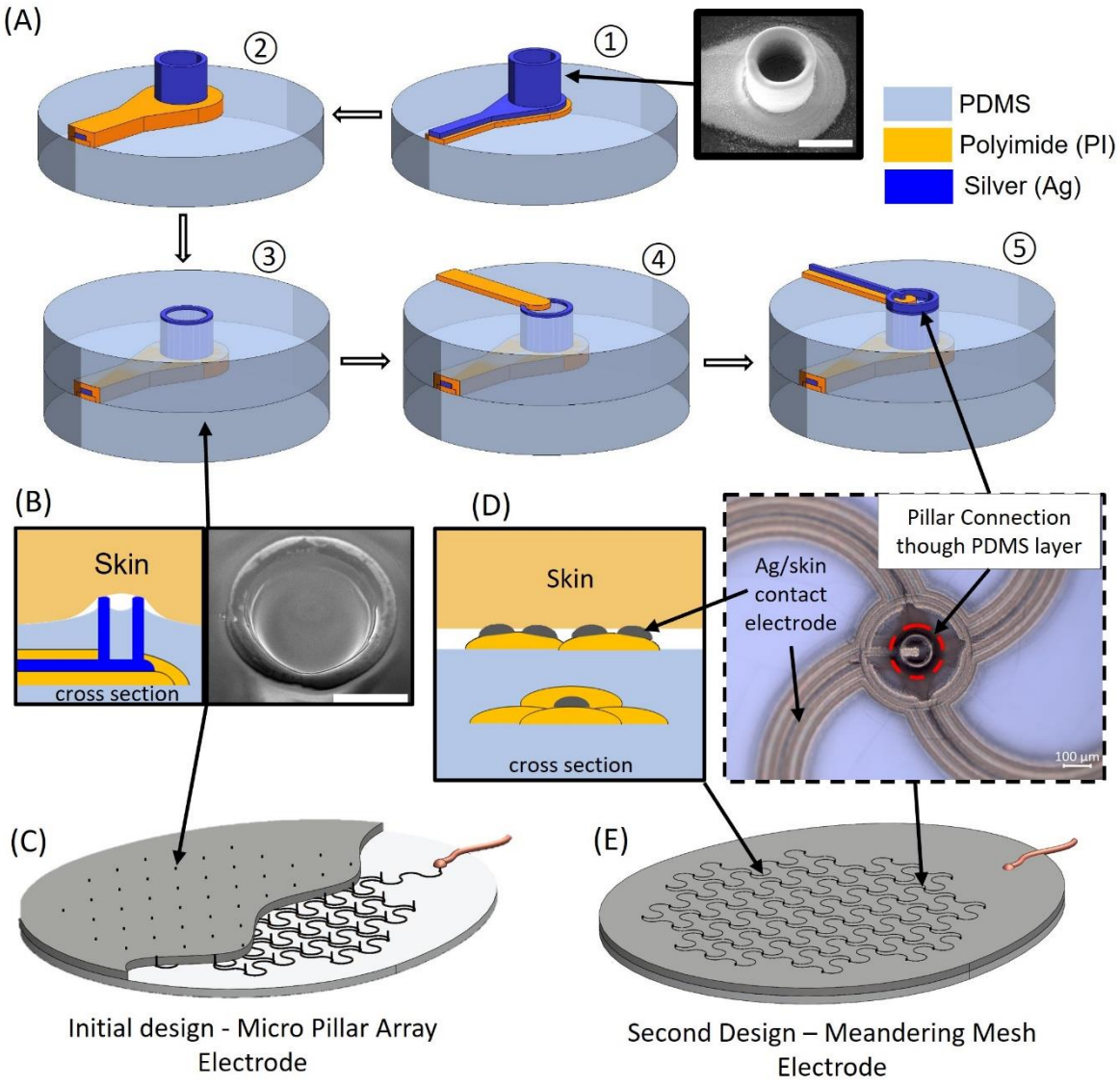

Figure 6.3: Dual-layer ECG patch design process and pillar connection schematic. (A) The fabrication process starts with (1) a 3D pillar of silver on a PI base printed directly on PDMS substrate (with an electron microscope image of the pillar where the scale bar is 100 µm). (2) The interconnect is then encapsulated by PI, and then (3) another layer of PDMS is spin cast on top with the pillar tips exposed. The initial ECG patch design stopped here and used the exposed pillar tip to contact the skin as shown in image (B). Then, an array of exposed pillars makes up the micropillar array electrode design shown in image (C). For the second design, (4) PI is printed as a base for the silver electrode layer and is printed over a section of the exposed silver pillar. (5) The top silver electrode layer is then printed to connect the pillar and embedded interconnect to the contact electrode on the top surface as shown in image (D). This allows for a meandering mesh electrode design shown in image (E).

6.3.1 Impedance Measurements

The suitability for wearable device applications is tested using EIS measurements as a measure of the device's biological signal quality. Due to the printed patch being fabricated as a dry electrode, additional interface layers were added to improve the contact between the skin and the electrodes. Interface layers tested include DI water, 1 M phosphate buffer solution (PBS), and electrode gel (Spectra 360, Parker Laboratories, Inc., Hannover, Germany). As a dry electrode, the printed patch has low adhesion to the skin, causing the skin contact electrodes to have insufficient adhesion to the skin and result in a high contact impedance. DI water is used as a baseline to measure the electrode-skin impedance of the printed patch with good adhesion to the skin. PBS is a commonly used buffer solution used in biological research as it has ion concentrations similar to the human body. Electrode gel is frequently used in hospitals to remove air gaps between the electrode-skin interface, reduce the electrical impedance, and avoid attenuation in the signal.[171] Similarly, the commercial patch electrodes used as comparison in this study also contain a wet adhesive and conductive gel. A size comparison of the printed patch and the tab electrodes are shown in Figure 6.6B. The EIS measurements comparing the initial ECG sensor prototype and the dual-layered meandering mesh design are shown in Figure 6.4, where only the DI water and PBS interface layers are shown for both the initial design (Figure 6.4A) and the dual-layer design, (Figure 6.4B). The initial design replaces only a single commercial electrode with a printed electrode, and the increase in impedance of a single patch is already almost an order of magnitude higher at low frequencies, and several orders of magnitude higher at the upper frequency range. Using two printed electrodes would increase the impedance even further. The dual-layer printed electrode has two orders of magnitude larger contact area compared to the initial printed electrode, and the resulting impedance is comparable to the tab style commercial patch when measuring between two

printed patches as shown in Figure 6.4B. From these plots, the increased surface contact of the meandering mesh reduces the impedance of the skin to values comparable to commercial electrodes and indicates suitability for capturing biopotential signals.

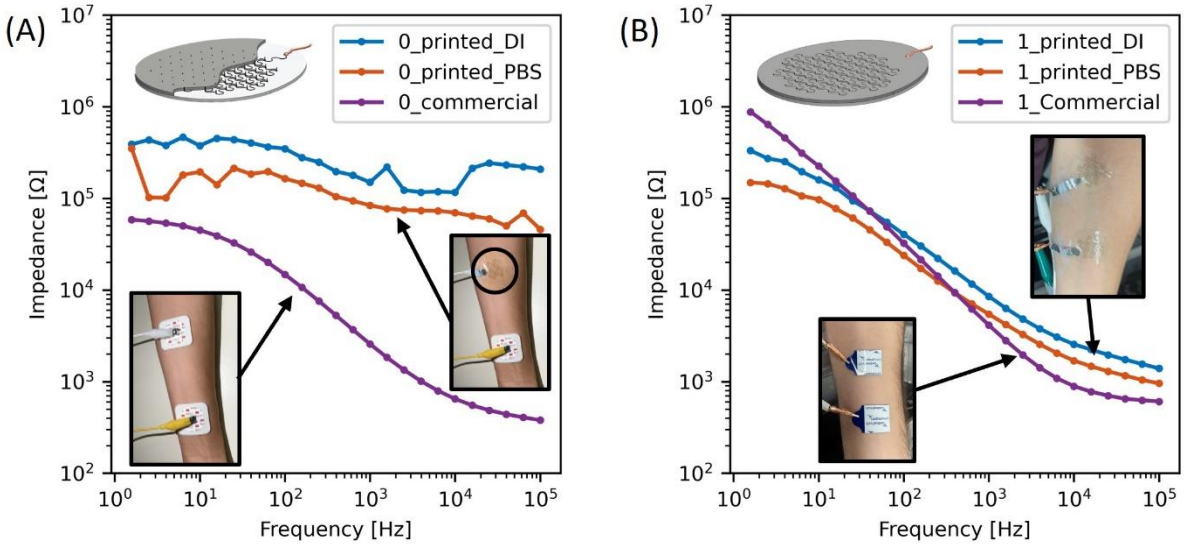

Figure 6.4: Comparison of measured impedance between initial micropillar array ECG design and the second dual-layer meandering mesh electrode design. (A) The impedance of a single printed patch with the initial micropillar array design with a commercial electrode is compared against two commercial patches. (B) The impedance of two printed patches with the second meandering mesh electrode design is compared against two commercial patches.

To test in conditions for chronic wear applications, the longevity of the patches is measured over the span of 1 hr and is shown for 100 Hz and 1 kHz in Figure 6.5B. Measurement at 100 Hz is shown to demonstrate the quality of the electrode-skin interface for ECG and EEG applications and the 1 kHz data is shown for higher frequency biomonitoring applications (e.g., EMG). From these results, the evaporation of the DI water and 1 M PBS on the printed patch are shown to increase the impedance over time. The electrode gel, on the other hand, holds a near constant impedance throughout that time. Like the printed patch with electrode gel, the commercial patch also maintains a lower constant impedance throughout the 1 hr test. There are significant ‘jumps’ in impedance for the printed patches, and these can be seen in Figure 6.5B by impedances more than an order of magnitude different from the trend. These

fluctuations are hypothesized to be caused by disconnection of the electrode from the skin, and happen more frequently on the DI water interlayer, but still occur on both the PBS and electrode gel interlayers. The commercial ECG patch shows a stable impedance over time, which may be due to the adhesive in the commercial patch keeping the electrode in continuous contact with the skin. The EIS measurements at 0 min and 60 min are shown in Figure 6.4A, where it can again be observed how the DI water and 1 M PBS impedance measurements increase over time, while the electrode gel remains constant similar to the commercial patch.

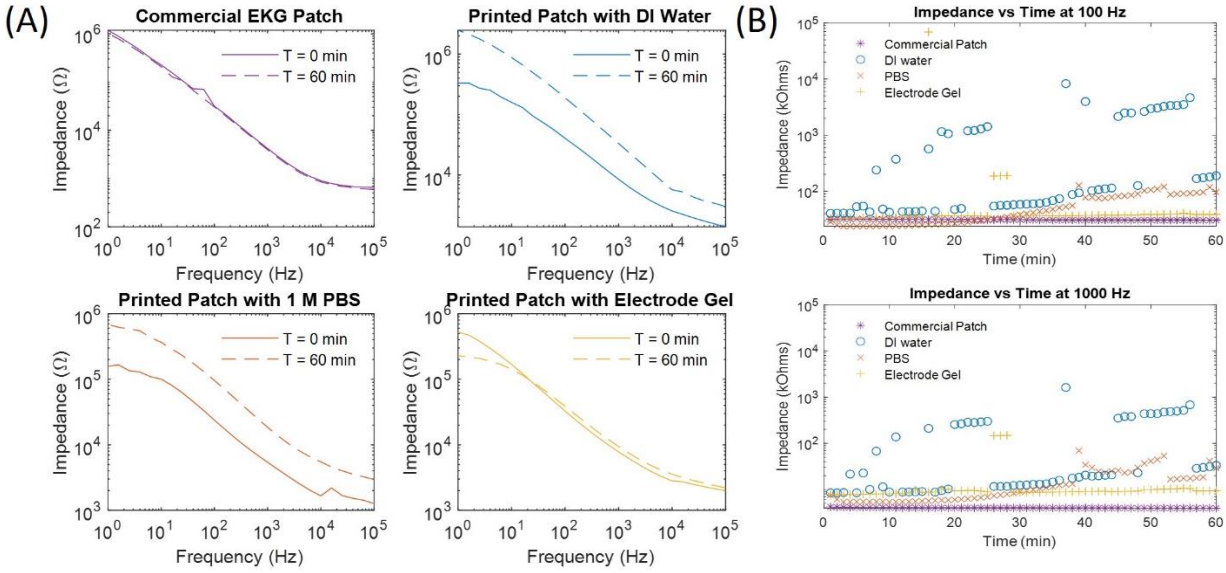

Figure 6.5: Impedance comparison for the dual layer printed electrodes and commercial electrodes. (A) Impedance frequency response for different interface layers compared with the commercial electrode shown at 0 min and 60 min. (B) Impedance at 100 Hz and 1 kHz for each interlayer liquid in comparison with the commercial electrode recorded every minute for 1 hr.

6.3.2 ECG Recording

As a demonstration of the skin-wearable and dual-layer printed electrode for biomonitoring applications, an ECG recording is captured from both the commercial patches and the printed patches. Figure 6.6A shows the placement of the electrodes on the skin following the Lead I configuration with recording electrodes placed on the forearms and the driven electrode placed on the left wrist. The external connection is facilitated by the aluminum tape which is connected

to the skin contact electrode through pillar VIAs and shown in the inset image of Figure 6.6A. The size comparison between the printed patch and tab style commercial patch is shown in Figure 6.6B.

Figure 6.6C shows the recorded ECG signals for the commercial patch and the printed patch with each of the added interface layers. All the measurements display a clearly recorded signal capturing the typical waveforms of a clinical ECG recording. The DI water recording shows a noticeably larger signal to noise ratio compared to the other signals. Both the printed patches with the PBS and electrode gel interlayer capture ECG signals with a qualitatively low signal to noise ratio similar to the commercial patch.

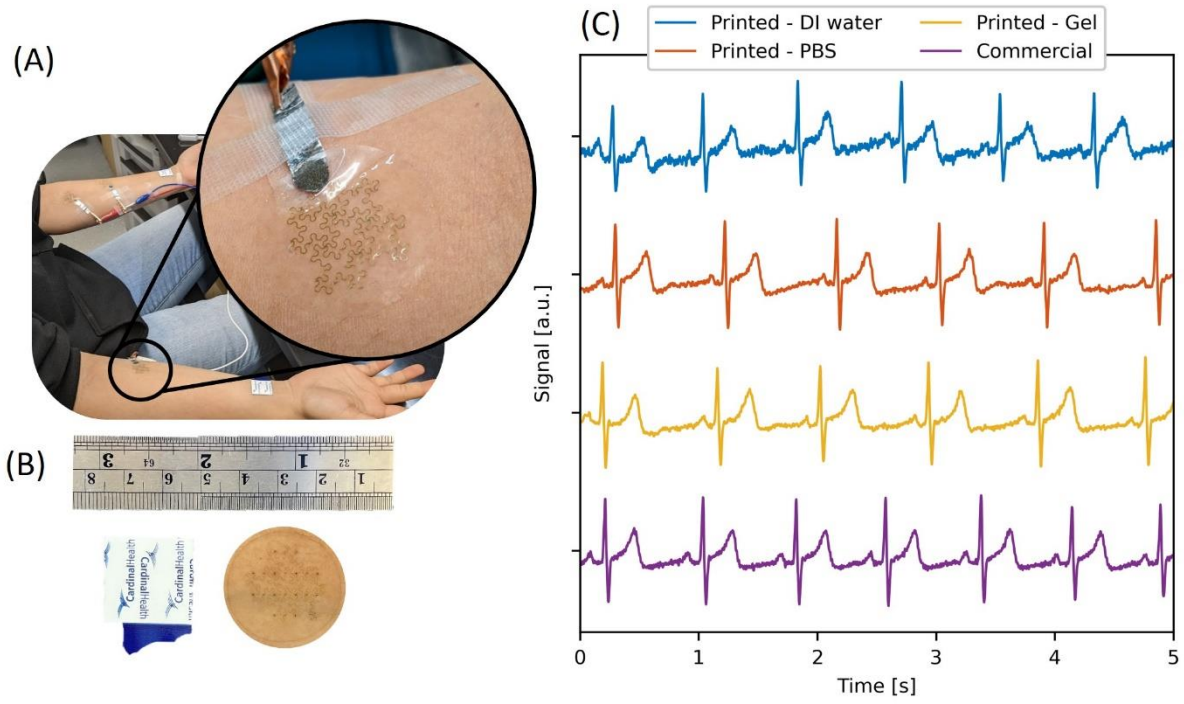

Figure 6.6: Electrocardiogram signal comparison between 3D printed and commercial electrodes. (A) The test set up is shown with recording electrodes on the forearms and the driven electrode on the left wrist to create a standard Lead I configuration. The inset image is a close-up of the 3D printed electrode with external connection via pillars. (B) Size comparison between the commercial electrode and the 3D printed electrode. (C) ECG recordings with different interlayer liquids compared with the commercial electrode.

6.4 Conclusions

A dual-level skin-wearable electrode is demonstrated using 3D printed VIAs to connect fully embedded interconnects with a surface electrode. The VIAs are fabricated directly in-place, using aerosol jet printing to create the 3D pillars in addition to the meandering interconnects and the polyimide encapsulation layer. An ECG signal is captured from three of these printed electrodes with a comparable quality to commercial patches when applied to the skin with a PBS solution or electrode gel. Skin impendence measurements show that using electrode gel as the interface material with the printed electrode provides the best impendence performance overtime compared to using PBS solution or DI water. The stretchability of the embedded interconnects is shown to withstand strains significantly larger than skin to function in wearable devices. The strain to failure of the embedded interconnects is shown to have a strain to failure of over 50% with more than 1000 cycles demonstrated at 30% strain. The stretchability of the interconnections and functionality of the printed VIAs are promising indicators that this technique can be utilized to incorporate off-the-shelf components to increase functionality and create dense multi-level and highly functional stretchable devices.

Chapter 7

Conclusions

In this thesis, stretchable meandering metallic electrical interconnects with 3D pillars for use as through layer connectivity are printed directly on an elastomer substrate using a wafer-compatible aerosol jet printing method. Process development is driven by investigating and solving the problems of delamination between polymer layers, cracking in the metal during sintering, and low conductivity of the sintered interconnects. Using the developed fabrication method, the interconnect is mechanically characterized using strain to failure and cyclical tensile tests to describe the stretchability. A multi-layer electrode capable of recording an electrocardiogram is fabricated to demonstrate the use of pillars as a VIA, and interface with human skin.

Integrating functional 3D structures on a stretchable electronics platform including multiple materials can unlock rich feature possibilities, but fabrication challenges associated with multi-material printing on a thin stretchable substrate are numerous. The first challenge investigated is the process temperature incompatibility between the sintering temperatures of nanoparticle silver ink used for the conductor, and the stretchable PDMS substrate. In Chapter 3, an initial investigation is carried out to determine if PDMS can retain the hyperelastic behavior when subjected to higher temperatures (200 to 300 °C) which are ideal for sintering the silver nanoparticle ink. The results indicate that the 20:1 PDMS maintained suitable mechanical properties and hyperelastic behavior through high-temperature treatment, including maintaining significant film stretchability. There was, however, a decrease in desired

mechanical performance as the post-cure heating temperature increased from 100 °C to 300 °C, as the failure strain decreased from 250 % to 106 %. Interestingly, the modulus decreased from 0.805 MPa to 0.621 MPa over the same increase in temperature which is beneficial for interfacing with other softer materials. The softening of the PDMS on heating indicates that polymer chain degradation rather than crosslinking occurs at temperatures up to 300 °C. The stretchability maintained by PDMS shows a limited degradation of its properties upon thermal exposure and demonstrates the suitability of the vacuum thermal treatment for subsequent microelectronics fabrication processes in temperatures up to 300 °C.

The second challenge investigated is the delamination between polyimide layers that is observed during the curing cycle of the top encapsulating polyimide layer. Experimental observations in Chapter 4 led to two hypotheses of the root cause of the delamination. Vapor driven delamination, similar to the pop-corning effect observed in conventional electronics packaging, is determined to be the cause of the delamination, and the analytical model developed provided the ability to perform a parametric analysis and resulted in a delamination mechanism map. Meander geometries are also investigated via a perturbation of the straight crack model, and the inside edge of the meander is shown to have a higher energy release rate when compared to the outside edge. Design guidelines for the polyimide layer thicknesses and silver widths are provided to aid in the future development of printed interconnects. Understanding the root cause also led to a process change to include a drying step to drive off moisture absorbed in the polyimide layer prior to reaching high temperatures where damaging vapor pressures are developed.

The vacuum sintering process initially showed promise as a path to achieve high temperature sintering without damaging the stretchable PDMS substrate (developed in Chapter 3) but resulted in two unacceptable drawbacks when including 3D pillars in the system to fully

embed the interconnect in PDMS. Chapter 5 investigates the process conditions that cause cracking at the pillar base and low conductivity in the sintered silver. Dry nitrogen and vacuum environments are shown to produce cracking during drying due to increased inter-particle capillary force from rapid solvent evaporation. Furthermore, organic ligands and binders present in Ag nanoparticle inks are shown to be removed more effectively in air at temperatures of 150 °C and above relative to the N_2 and vacuum environments. A hybrid sintering process including a drying step conducted in air up to 150 °C, followed by a high temperature treatment in vacuum is shown to preserve the stretchable substrate, while producing crack-free and highly conductive 3D interconnects up to 56 % of bulk Ag. This process development enables 3D pillars to be integrated into the embedded interconnect and extend through the PDMS layer to interface with external components or function as a VIA to connect to additional layers of circuitry.

After addressing fundamental processing challenges, fully embedded interconnects with external connectivity and multi-level device architectures can be explored. In chapter 6 the interconnects demonstrate strain to failure of over 50% and survive over 1000 cycles at 30% strain. The electrical resistance was simultaneously measured during the tensile tests enabled by pillars extending through the top layer of PDMS. A thin dual-layered electrode is fabricated using a meandering mesh design and is utilized to record skin potentials and capture an electrocardiogram. The work detailed in this thesis to investigate and solve fabrication challenges to realize functional 3D printed VIAs directly on a thin and stretchable substrate using the aerosol jet represents a substantial contribution to the additive manufacturing and stretchable electronics fields.

7.1 Future Work

While several processing developments have led to a successful demonstration of 3D multi-layered interconnects that can monitor cardiac signals, much work is required to achieve functional stretchable devices following the fabrication scheme developed in this thesis. The ECG electrode had intermittent contact with the skin and had inconsistent impedance compared to the commercial electrode. Adding an adhesive layer, integrating adhesive compounds in the PDMS, or adding a conductive and adhesive interlayer could improve the interface with the skin. The external connection is currently a stiff and relatively large aluminum tape that does not stretch and flex with the skin, and it may be another cause of disconnection with the skin causing an intermittent signal. Fabricating a patch with multiple electrodes with wireless data transfer and power would remove the need for external connection and allow the patch to conform to the skin.

The ability to integrate stiff high performance integrated circuit chips and common surface mount components into the stretchable electronics system would enable multi-functional devices on par with the state-of-the-art stiff and flexible printed circuit boards. Conceptually, stiffness gradients can be patterned with a base of polymer with a silver pad similar to the base of the pillars developed in this work. Then, components can be soldered in place using a low temperature solder or using an unsintered layer of silver nanoparticle ink. The aerosol jet could then print an encapsulation layer of polymer on top of the components to provide a stiffness gradient on all sides.

Including a high density of interconnects and stiff components will significantly decrease the overall stretchability of the system. Including multi-level and varied height VIAs would allow stacking stiff components out of the plane to enable less dense packing in the stretching

plane and allow for more flexibility in packaging to connect across several layers. Currently, the pillars are only able to connect through one layer of PDMS.

The manufacturing process detailed in this thesis requires several steps of removing the substrate from the aerosol jet printer, long curing and sintering times, and a custom vacuum oven capable of pressure and temperature control. Several material choices, and process changes could significantly speed up the fabrication process. A UV curable polymer could be substituted for the polyimide and serve the same stiffness gradient function, while curing in seconds on the aerosol jet platen without being removed. This could allow for immediate printing of the conductive layer on the polymer stiffness gradient. Following the same cure in-place concept, laser sintering is an option for metal nanoparticle inks and would be compatible with the layer-by-layer printing process of 3D features and opens the possibility of using lower cost Cu nanoparticle inks. However, close tracking of pillar height would be required to correctly aim the laser at the correct height. This would allow the same capability for the part to remain on the printing platen during sintering, and it would only need to be removed for spin casting of the next stretchable layer and eliminate the need for a specialized vacuum oven. Eliminating the etching step would enable a fully additive process and remove the need for harsh etching chemicals, but the buildup of PDMS during spinning around the pillars would need to be avoided. Enabling integration of high-performance components over several layers and speeding up the fabrication process would move towards a commercially viable process.

References

1 Herculano-Houzel, S. The remarkable, yet not extraordinary, human brain as a scaled-up primate brain and its associated cost. *Proc Natl Acad Sci* **109**, 10661-10668, doi:10.1073/pnas.1201895109 (2012).

2 Rogers, J. A., Ghaffari, R. & Kim, D.-H. *Stretchable Bioelectronics for Medical Devices and Systems*. (Springer International Publishing, 2016).

3 Majidi, C. Soft Robotics: A Perspective—Current Trends and Prospects for the Future. *Soft Robotics* **1**, 5-11, doi:10.1089/soro.2013.0001 (2014).

4 Chung, H. U., Kim, B. H., Lee, J. Y., Lee, J., Xie, Z., Ibler, E. M., . . . Rogers, J. A. Binodal, wireless epidermal electronic systems with in-sensor analytics for neonatal intensive care. *Science* **363**, doi:10.1126/science.aau0780 (2019).

5 Park, Y. L., Chen, B. R., Perez-Arancibia, N. O., Young, D., Stirling, L., Wood, R. J., . . . Nagpal, R. Design and control of a bio-inspired soft wearable robotic device for ankle-foot rehabilitation. *Bioinspir Biomim* **9**, 016007, doi:10.1088/1748-3182/9/1/016007 (2014).

6 Xu, S., Jayaraman, A. & Rogers, J. A. Skin sensors are the future of health care. *Nature* **571**, 319-321 (2019).

7 Hsu, P. I., Huang, M., Xi, Z., Wagner, S., Suo, Z. & Sturm, J. C. Spherical deformation of compliant substrates with semiconductor device islands. *Journal of Applied Physics* **95**, 705-712, doi:10.1063/1.1634370 (2004).

8 Lu, N., Yoon, J. & Suo, Z. Delamination of stiff islands patterned on stretchable substrates. *International Journal of Materials Research* **98**, 717-722, doi:10.3139/146.101529 (2007).

9 Naserifar, N., LeDuc, P. R. & Fedder, G. K. Material Gradients in Stretchable Substrates toward Integrated Electronic Functionality. *Adv Mater* **28**, 3584-3591, doi:10.1002/adma.201505818 (2016).

10 Kim, D. H., Ahn, J. H., Choi, W. M., Kim, H. S., Kim, T. H., Song, J., . . . Rogers, J. A. Stretchable and foldable silicon integrated circuits. *Science* **320**, 507-511, doi:10.1126/science.1154367 (2008).

11 Xu, S., Zhang, Y., Jia, L., Mathewson, K. E., Jang, K. I., Kim, J., . . . Rogers, J. A. Soft microfluidic assemblies of sensors, circuits, and radios for the skin. *Science* **344**, 70-74, doi:10.1126/science.1250169 (2014).

12 Hammock, M. L., Chortos, A., Tee, B. C., Tok, J. B. & Bao, Z. The evolution of electronic skin (e-skin): a brief history, design considerations, and recent progress. *Adv Mater* **25**, 5997-6038, doi:10.1002/adma.201302240 (2013).

13 Dickey, M. D. Stretchable and Soft Electronics using Liquid Metals. *Adv Mater* **29**, doi:10.1002/adma.201606425 (2017).

14 Wang, J., Cai, G., Li, S., Gao, D., Xiong, J. & Lee, P. S. Printable Superelastic Conductors with Extreme Stretchability and Robust Cycling Endurance Enabled by Liquid-Metal Particles. *Adv Mater* **30**, e1706157, doi:10.1002/adma.201706157 (2018).

15 Markvicka, E. J., Bartlett, M. D., Huang, X. & Majidi, C. An autonomously electrically self-healing liquid metal-elastomer composite for robust soft-matter robotics and electronics. *Nat Mater* **17**, 618-624, doi:10.1038/s41563-018-0084-7 (2018).

16 Kim, T. A., Kim, H. S., Lee, S. S. & Park, M. Single-walled carbon nanotube/silicone rubber composites for compliant electrodes. *Carbon* **50**, 444-449, doi:10.1016/j.carbon.2011.08.070 (2012).
17 Kim, K. H., Vural, M. & Islam, M. F. Single-walled carbon nanotube aerogel-based elastic conductors. *Adv Mater* **23**, 2865-2869, doi:10.1002/adma.201100310 (2011).
18 Hsu, Y.-Y., Gonzalez, M., Bossuyt, F., Vanfleteren, J. & De Wolf, I. Polyimide-Enhanced Stretchable Interconnects: Design, Fabrication, and Characterization. *IEEE Transactions on Electron Devices* **58**, 2680-2688, doi:10.1109/ted.2011.2147789 (2011).
19 Jones, J., Lacour, S. P., Wagner, S. & Suo, Z. Stretchable wavy metal interconnects. *Journal of Vacuum Science & Technology A: Vacuum, Surfaces, and Films* **22**, 1723-1725, doi:10.1116/1.1756879 (2004).
20 Kim, D. H., Song, J., Choi, W. M., Kim, H. S., Kim, R. H., Liu, Z., . . . Rogers, J. A. Materials and noncoplanar mesh designs for integrated circuits with linear elastic responses to extreme mechanical deformations. *Proc Natl Acad Sci U S A* **105**, 18675-18680, doi:10.1073/pnas.0807476105 (2008).
21 Khan, Y., Garg, M., Gui, Q., Schadt, M., Gaikwad, A., Han, D., . . . Arias, A. C. Flexible Hybrid Electronics: Direct Interfacing of Soft and Hard Electronics for Wearable Health Monitoring. *Advanced Functional Materials* **26**, 8764-8775, doi:10.1002/adfm.201603763 (2016).
22 Xu, S., Zhang, Y., Cho, J., Lee, J., Huang, X., Jia, L., . . . Rogers, J. A. Stretchable batteries with self-similar serpentine interconnects and integrated wireless recharging systems. *Nat Commun* **4**, 1543, doi:10.1038/ncomms2553 (2013).
23 Kim, R. H., Kim, D. H., Xiao, J., Kim, B. H., Park, S. I., Panilaitis, B., . . . Rogers, J. A. Waterproof AlInGaP optoelectronics on stretchable substrates with applications in biomedicine and robotics. *Nat Mater* **9**, 929-937, doi:10.1038/nmat2879 (2010).
24 Choi, C., Lee, J. M., Kim, S. H., Kim, S. J., Di, J. & Baughman, R. H. Twistable and Stretchable Sandwich Structured Fiber for Wearable Sensors and Supercapacitors. *Nano Lett* **16**, 7677-7684, doi:10.1021/acs.nanolett.6b03739 (2016).
25 Wang, S., Xu, J., Wang, W., Wang, G. N., Rastak, R., Molina-Lopez, F., . . . Bao, Z. Skin electronics from scalable fabrication of an intrinsically stretchable transistor array. *Nature* **555**, 83-88, doi:10.1038/nature25494 (2018).
26 Huang, Q. & Zhu, Y. Printing Conductive Nanomaterials for Flexible and Stretchable Electronics: A Review of Materials, Processes, and Applications. *Advanced Materials Technologies* **4**, doi:10.1002/admt.201800546 (2019).
27 Perelaer, J., Smith, P. J., Mager, D., Soltman, D., Volkman, S. K., Subramanian, V., . . . Schubert, U. S. Printed electronics: the challenges involved in printing devices, interconnects, and contacts based on inorganic materials. *Journal of Materials Chemistry* **20**, doi:10.1039/c0jm00264j (2010).
28 Ko, S. H., Chung, J., Hotz, N., Nam, K. H. & Grigoropoulos, C. P. Metal nanoparticle direct inkjet printing for low-temperature 3D micro metal structure fabrication. *Journal of Micromechanics and Microengineering* **20**, doi:10.1088/0960-1317/20/12/125010 (2010).
29 Han, Y. & Dong, J. Electrohydrodynamic Printing for Advanced Micro/Nanomanufacturing: Current Progresses, Opportunities, and Challenges. *Journal of Micro and Nano-Manufacturing* **6**, doi:10.1115/1.4041934 (2018).

30 Han, Y. & Dong, J. Design of Integrated Ring Extractor for High Resolution Electrohydrodynamic (EHD) 3D Printing. *Procedia Manufacturing* **5**, 1031-1042, doi:10.1016/j.promfg.2016.08.070 (2016).
31 Fernández-Pradas, J. M., Sopeña, P., González-Torres, S., Arrese, J., Cirera, A. & Serra, P. Laser-induced forward transfer for printed electronics applications. *Applied Physics A* **124**, doi:10.1007/s00339-018-1648-8 (2018).
32 Tanaka, T., Ishikawa, A. & Kawata, S. Two-photon-induced reduction of metal ions for fabricating three-dimensional electrically conductive metallic microstructure. *Applied Physics Letters* **88**, doi:10.1063/1.2177636 (2006).
33 Geng, Q., Wang, D., Chen, P. & Chen, S. C. Ultrafast multi-focus 3-D nano-fabrication based on two-photon polymerization. *Nat Commun* **10**, 2179, doi:10.1038/s41467-019-10249-2 (2019).
34 Secor, E. B. Principles of aerosol jet printing. *Flexible and Printed Electronics* **3**, doi:10.1088/2058-8585/aace28 (2018).
35 Saleh, M. S., Hu, C. & Panat, R. Three-dimensional microarchitected materials and devices using nanoparticle assembly by pointwise spatial printing. *Sci Adv* **3**, e1601986, doi:10.1126/sciadv.1601986 (2017).
36 Sadeq Saleh, M., HamidVishkasougheh, M., Zbib, H. & Panat, R. Polycrystalline micropillars by a novel 3-D printing method and their behavior under compressive loads. *Scripta Materialia* **149**, 144-149, doi:10.1016/j.scriptamat.2018.02.027 (2018).
37 Saleh, M. S., Li, J., Park, J. & Panat, R. 3D printed hierarchically-porous microlattice electrode materials for exceptionally high specific capacity and areal capacity lithium ion batteries. *Additive Manufacturing* **23**, 70-78, doi:10.1016/j.addma.2018.07.006 (2018).
38 Rahman, M. T., Moser, R., Zbib, H. M., Ramana, C. V. & Panat, R. 3D printed high performance strain sensors for high temperature applications. *Journal of Applied Physics* **123**, doi:10.1063/1.4999076 (2018).
39 Rahman, M. T., Cheng, C.-Y., Karagoz, B., Renn, M., Schrandt, M., Gellman, A. & Panat, R. High Performance Flexible Temperature Sensors via Nanoparticle Printing. *ACS Applied Nano Materials* **2**, 3280-3291, doi:10.1021/acsanm.9b00628 (2019).
40 Rahman, M. T., Rahimi, A., Gupta, S. & Panat, R. Microscale additive manufacturing and modeling of interdigitated capacitive touch sensors. *Sensors and Actuators A: Physical* **248**, 94-103, doi:10.1016/j.sna.2016.07.014 (2016).
41 Ali, M. A., Hu, C., Jahan, S., Yuan, B., Saleh, M. S., Ju, E., . . . Panat, R. Sensing of COVID-19 Antibodies in Seconds via Aerosol Jet Nanoprinted Reduced-Graphene-Oxide-Coated 3D Electrodes. *Adv Mater* **33**, e2006647, doi:10.1002/adma.202006647 (2021).
42 Biswas, S., Schoeberl, A., Hao, Y., Reiprich, J., Stauden, T., Pezoldt, J. & Jacobs, H. O. Integrated multilayer stretchable printed circuit boards paving the way for deformable active matrix. *Nat Commun* **10**, 4909, doi:10.1038/s41467-019-12870-7 (2019).
43 Lacour, S. P., Wagner, S., Narayan, R. J., Li, T. & Suo, Z. Stiff subcircuit islands of diamondlike carbon for stretchable electronics. *Journal of Applied Physics* **100**, doi:10.1063/1.2210170 (2006).
44 Romeo, A., Liu, Q., Suo, Z. & Lacour, S. P. Elastomeric substrates with embedded stiff platforms for stretchable electronics. *Applied Physics Letters* **102**, doi:10.1063/1.4799653 (2013).

45 Naserifar, N., LeDuc, P. R. & Fedder, G. K. Drop casting of stiffness gradients for chip integration into stretchable substrates. *Journal of Micromechanics and Microengineering* **27**, doi:10.1088/1361-6439/aa63af (2017).
46 Graz, I. M., Cotton, D. P. J., Robinson, A. & Lacour, S. P. Silicone substrate with in situ strain relief for stretchable thin-film transistors. *Applied Physics Letters* **98**, doi:10.1063/1.3570661 (2011).
47 Harris, K. D., Elias, A. L. & Chung, H. J. Flexible electronics under strain: a review of mechanical characterization and durability enhancement strategies. *Journal of Materials Science* **51**, 2771-2805, doi:10.1007/s10853-015-9643-3 (2015).
48 Gonzalez, M., Axisa, F., Bulcke, M. V., Brosteaux, D., Vandevelde, B. & Vanfleteren, J. Design of metal interconnects for stretchable electronic circuits. *Microelectronics Reliability* **48**, 825-832, doi:10.1016/j.microrel.2008.03.025 (2008).
49 Waghule, T., Singhvi, G., Dubey, S. K., Pandey, M. M., Gupta, G., Singh, M. & Dua, K. Microneedles: A smart approach and increasing potential for transdermal drug delivery system. *Biomed Pharmacother* **109**, 1249-1258, doi:10.1016/j.biopha.2018.10.078 (2019).
50 Forssell, M. *Long-Term Insulation of Active Electronics Embedded in Compliant Neural Probes*, Carnegie Mellon University, (2019).
51 Rahman, M. T., Moser, R., Zbib, H. M., Ramana, C. & Panat, R. 3D printed high performance strain sensors for high temperature applications. *Journal of Applied Physics* **123**, 024501 (2018).
52 Binder, S., Glatthaar, M. & Rädlein, E. Analytical Investigation of Aerosol Jet Printing. *Aerosol Science and Technology* **48**, 924-929, doi:10.1080/02786826.2014.940439 (2014).
53 Chen, G., Gu, Y., Tsang, H., Hines, D. R. & Das, S. The Effect of Droplet Sizes on Overspray in Aerosol-Jet Printing. *Advanced Engineering Materials* **20**, doi:10.1002/adem.201701084 (2018).
54 Mahajan, A., Frisbie, C. D. & Francis, L. F. Optimization of aerosol jet printing for high-resolution, high-aspect ratio silver lines. *ACS Appl Mater Interfaces* **5**, 4856-4864, doi:10.1021/am400606y (2013).
55 Gomathi, N., Mishra, I., Varma, S. & Neogi, S. Surface modification of poly(dimethylsiloxane) through oxygen and nitrogen plasma treatment to improve its characteristics towards biomedical applications. *Surface Topography: Metrology and Properties* **3**, doi:10.1088/2051-672x/3/3/035005 (2015).
56 Li, C. Y. & Liao, Y. C. Adhesive Stretchable Printed Conductive Thin Film Patterns on PDMS Surface with an Atmospheric Plasma Treatment. *ACS Appl Mater Interfaces* **8**, 11868-11874, doi:10.1021/acsami.6b02844 (2016).
57 Brenneman, J., Tansel, D. Z., Fedder, G. K. & Panat, R. High-Conductivity Crack-Free 3D Electrical Interconnects Directly Printed on Soft PDMS Substrates. *Advanced Materials Technologies*, doi:10.1002/admt.202200396 (2022).
58 Company, D. C. SYLGARD™ 184 Silicone Elastomer Kit Technical Data Sheet. (2017).
59 HDMicroSystems. Product Bulletin PI 2525, PI 2555, PI 2574. (2012).
60 Wang, X., Liu, Z. & Zhang, T. Flexible Sensing Electronics for Wearable/Attachable Health Monitoring. *Small* **13**, doi:10.1002/smll.201602790 (2017).

61 Liu, Y., Pharr, M. & Salvatore, G. A. Lab-on-Skin: A Review of Flexible and Stretchable Electronics for Wearable Health Monitoring. *ACS Nano* **11**, 9614-9635, doi:10.1021/acsnano.7b04898 (2017).
62 Belanger, M.-C., Yves Marois. Hemocompatibility, Biocompatibility, Inflammatory and in Vivo Studies of Primary Reference Materials Low-Density Polyethylene and Polydimethylsiloxane: A Review. *Journal of Biomedical Materials Research* **58**, 467-477 (2001).
63 Eduok, U., Faye, O. & Szpunar, J. Recent developments and applications of protective silicone coatings: A review of PDMS functional materials. *Progress in Organic Coatings* **111**, 124-163, doi:10.1016/j.porgcoat.2017.05.012 (2017).
64 Dutta, I. & Panat, R. Highly stretchable interconnect devices and systems. United States Patent #9770759 (2017).
65 Arafat, Y., Dutta, I. & Panat, R. Super-stretchable metallic interconnects on polymer with a linear strain of up to 100%. *Applied Physics Letters* **107**, 081906 (2015).
66 Wang, Z., Volinsky, A. A. & Gallant, N. D. Crosslinking effect on polydimethylsiloxane elastic modulus measured by custom-built compression instrument. *Journal of Applied Polymer Science* **131** (2014).
67 Grassie, N. & Macfarlane, I. G. The thermal degradation of polysiloxanes—I. Poly(dimethylsiloxane). *European Polymer Journal* **14**, 875-884, doi:10.1016/0014-3057(78)90084-8 (1978).
68 Camino, G., Lomakin, S. M. & Lazzari, M. Polydimethylsiloxane thermal degradation Part 1. Kinetic aspects. *Polymer* **42**, 2395-2402, doi:10.1016/s0032-3861(00)00652-2 (2001).
69 Liu, M., Sun, J. & Chen, Q. Influences of heating temperature on mechanical properties of polydimethylsiloxane. *Sensors and Actuators A: Physical* **151**, 42-45, doi:10.1016/j.sna.2009.02.016 (2009).
70 Khanafer, K., Duprey, A., Schlicht, M. & Berguer, R. Effects of strain rate, mixing ratio, and stress-strain definition on the mechanical behavior of the polydimethylsiloxane (PDMS) material as related to its biological applications. *Biomed Microdevices* **11**, 503-508, doi:10.1007/s10544-008-9256-6 (2009).
71 Liu, M. Characterization study of bonded and unbonded polydimethylsiloxane aimed for bio-micro-electromechanical systems-related applications. *Journal of Micro/Nanolithography, MEMS, and MOEMS* **6**, doi:10.1117/1.2731381 (2007).
72 Johnston, I. D., McCluskey, D. K., Tan, C. K. L. & Tracey, M. C. Mechanical characterization of bulk Sylgard 184 for microfluidics and microengineering. *Journal of Micromechanics and Microengineering* **24**, doi:10.1088/0960-1317/24/3/035017 (2014).
73 Schneider, F., Fellner, T., Wilde, J. & Wallrabe, U. Mechanical properties of silicones for MEMS. *Journal of Micromechanics and Microengineering* **18**, doi:10.1088/0960-1317/18/6/065008 (2008).
74 Ogden, R. W. Large Deformation Isotropic Elasticity - On the Correlation of Theory and Experiment for Incompressible Rubberlike Solids. *Proceedings of the Royal Society A: Mathematical, Physical and Engineering Sciences* **326**, 565-584, doi:10.1098/rspa.1972.0026 (1972).
75 Mooney, M. A theory of large elastic deformation. *Journal of applied physics* **11**, 582-592 (1940).

76 Hopf, R., Bernardi, L., Menze, J., Zundel, M., Mazza, E. & Ehret, A. E. Experimental and theoretical analyses of the age-dependent large-strain behavior of Sylgard 184 (10:1) silicone elastomer. *J Mech Behav Biomed Mater* **60**, 425-437, doi:10.1016/j.jmbbm.2016.02.022 (2016).
77 Kim, T. K., Kim, J. K. & Jeong, O. C. Measurement of nonlinear mechanical properties of PDMS elastomer. *Microelectronic Engineering* **88**, 1982-1985, doi:10.1016/j.mee.2010.12.108 (2011).
78 ASTM. Standard Test Methods for Vulcanized Rubber and Thermoplastic Elastomers— Tension. D412. 2016
79 Asma Sharfeddin, A. A. V., Greeshma Mohan, Nathan D. Gallant. Comparison of the macroscale and microscale tests for measuring elastic properties of polydimethylsiloxane. *Journal of Applied Polymer Science* **132**, doi:10.1002/app.42680 (2015).
80 Liu, M., Sun, J., Sun, Y., Bock, C. & Chen, Q. Thickness-dependent mechanical properties of polydimethylsiloxane membranes. *Journal of Micromechanics and Microengineering* **19**, doi:10.1088/0960-1317/19/3/035028 (2009).
81 Ehret, A. E. On a molecular statistical basis for Ogden's model of rubber elasticity. *Journal of the Mechanics and Physics of Solids* **78**, 249-268, doi:10.1016/j.jmps.2015.02.006 (2015).
82 Bernardi, L., Hopf, R., Ferrari, A., Ehret, A. E. & Mazza, E. On the large strain deformation behavior of silicone-based elastomers for biomedical applications. *Polymer Testing* **58**, 189-198, doi:10.1016/j.polymertesting.2016.12.029 (2017).
83 Smooth-On. Mold Max™ 60 High Heat Resistant Silicone Rubber Compound Datasheet. (2021).
84 Smooth-On. Ecoflex™ Near Clear™ Series Datasheet. (2021).
85 Lam, D. C. C., Chong, J. I. T. & Pin, T. The role of water in delamination in electronics packages: water evaporation from epoxy. *IEEE Transactions on Components and Packaging Technologies* **25**, 708-713, doi:10.1109/tcapt.2002.806174 (2002).
86 Dupont. Kapton: Summary of Properties. (2017).
87 HDMicroSystems. Product Bulletin: PI 2525, PI 2555 & PI 2574. (2012).
88 Brown, H. R., Yang, A. C. M., Russell, T. P., Volksen, W. & Kramer, E. J. Diffusion and Self-Adhesion of the Polyimide PMDA-ODA. *Polymer* **29**, 1807-1811, doi:10.1016/0032-3861(88)90395-3 (1988).
89 Freund, L. B. & Suresh, S. in *Thin Film Materials, Stress, Defect Formation and Surface Evolution* Ch. 4, 220-311 (Cambridge University Press, 2003).
90 Suhir, E. An Approximate Analysis of Stresses in Multilayered Elastic Thin Films. *Journal of Applied Mechanics* **55**, 143-148 (1988).
91 Herbert, R., Mishra, S., Lim, H. R., Yoo, H. & Yeo, W. H. Fully Printed, Wireless, Stretchable Implantable Biosystem toward Batteryless, Real-Time Monitoring of Cerebral Aneurysm Hemodynamics. *Adv Sci (Weinh)* **6**, 1901034, doi:10.1002/advs.201901034 (2019).
92 Hoang, M. V., Chung, H.-J. & Elias, A. L. Irreversible bonding of polyimide and polydimethylsiloxane (PDMS) based on a thiol-epoxy click reaction. *Journal of Micromechanics and Microengineering* **26**, doi:10.1088/0960-1317/26/10/105019 (2016).

93 Lee, C. H., Ma, Y., Jang, K.-I., Banks, A., Pan, T., Feng, X., . . . Rogers, J. A. Soft Core/Shell Packages for Stretchable Electronics. *Advanced Functional Materials* **25**, 3698-3704, doi:10.1002/adfm.201501086 (2015).
94 Lee, S. P., Ha, G., Wright, D. E., Ma, Y., Sen-Gupta, E., Haubrich, N. R., . . . Ghaffari, R. Highly flexible, wearable, and disposable cardiac biosensors for remote and ambulatory monitoring. *NPJ Digit Med* **1**, 2, doi:10.1038/s41746-017-0009-x (2018).
95 Jou, J.-H., Liu, C.-H., Liu, J.-M. & King, J.-S. Adhesion of Polyimide to Silicon and Polyimide. *Journal of Applied Polymer Science* **47**, 1219-1232 (1993).
96 Fan, X. J., Zhou, J., Zhang, G. Q. & Ernst, L. J. A Micromechanics-Based Vapor Pressure Model in Electronic Packages. *Journal of Electronic Packaging* **127**, 262-267, doi:10.1115/1.1939027 (2005).
97 Zhang, X., Meng, H., Wang, H. & Guo, F. Effect of thermal misfit stress on steam-driven delamination in electronic packages. *Engineering Fracture Mechanics* **194**, 61-72, doi:10.1016/j.engfracmech.2018.03.008 (2018).
98 Andrews, E. H. & Stevenson, A. Fracture Energy of Epoxy Resin Under Plane Strain Conditions. *Journal of Materials Science* **13**, 1680-1688 (1978).
99 Liechti, K. M. & Shirani, A. Large Scale Yielding in Blister Specimens. *International Journal of Fracture* **67**, 21-36 (1994).
100 Dillard, D. A. & Bao, Y. The Peninsula Blister Test: A High and Constant Strain Energy Release Rate Fracture Specimen for Adhesives. *The Journal of Adhesion* **33**, 253-271, doi:10.1080/00218469108026498 (2006).
101 Audoly, B. Stability of Straight Delamination Blisters. *Physical Review Letters* **83** (1999).
102 Xu, D., Liechti, K. M. & de Lumley-Woodyear, T. H. Closed Form Nonlinear Analysis of the Peninsula Blister Test. *The Journal of Adhesion* **82**, 831-866, doi:10.1080/00218460600822922 (2006).
103 Allen, M. G. & Senturia, S. D. Application of the Island Blister Test for Thin Film Adhesion Measurement. *The Journal of Adhesion* **29**, 219-231, doi:10.1080/00218468908026488 (1989).
104 Lam, D. C. C., Chong, I. T. & Tong, P. Parametric Analysis of Steam Driven Delamination in Electronics Package. *IEEE Transactions on Electronics Packaging Manufacturing* **23**, 208-213 (2000).
105 Denton, D., Day, D., Priore, D. F., Senturia, S., Anolick, E. & Scheider, D. Moisture diffusion in poltimide films in integrated circuits. *Journal of electronic materials* **14**, 119-136 (1985).
106 Sacher, E. & Susko, J. R. Water Permeation of Polymer Films. I. Polyimide. *Journal of Applied Polymer Science* **23**, 2355-2364 (1979).
107 Timoshenko, S. & Woinowski-Krieger, S. *Theory of Plates and Shells*. 2nd edn, (McGraw-Hill Book Company, 1959).
108 Danaei, R., Varghese, T., Ahmadzadeh, M., McCloy, J., Hollar, C., Sadeq Saleh, M., . . . Panat, R. Ultrafast fabrication of thermoelectric films by pulsed light sintering of colloidal nanoparticles on flexible and rigid substrates. *Advanced Engineering Materials* **21**, 1800800 (2019).
109 Rahman, M. T., McCloy, J., Ramana, C. V. & Panat, R. Structure, electrical characteristics, and high-temperature stability of aerosol jet printed silver nanoparticle films. *Journal of Applied Physics* **120**, doi:10.1063/1.4960779 (2016).

110 Kim, Y., Ren, X., Kim, J. W. & Noh, H. Direct inkjet printing of micro-scale silver electrodes on polydimethylsiloxane (PDMS) microchip. *Journal of Micromechanics and Microengineering* **24**, doi:10.1088/0960-1317/24/11/115010 (2014).
111 Renn, M. J., Schrandt, M., Renn, J. & Feng, J. Q. Localized Laser Sintering of Metal Nanoparticle Inks Printed with Aerosol Jet® Technology for Flexible Electronics. *Journal of Microelectronics and Electronic Packaging* **14**, 132-139, doi:10.4071/imaps.521797 (2017).
112 Perelaer, J., de Gans, B. J. & Schubert, U. S. Ink-jet Printing and Microwave Sintering of Conductive Silver Tracks. *Advanced Materials* **18**, 2101-2104, doi:10.1002/adma.200502422 (2006).
113 Wakuda, D., Hatamura, M. & Suganuma, K. Novel method for room temperature sintering of Ag nanoparticle paste in air. *Chemical Physics Letters* **441**, 305-308, doi:10.1016/j.cplett.2007.05.033 (2007).
114 Danaei, R., Varghese, T., Ahmadzadeh, M., McCloy, J., Hollar, C., Sadeq Saleh, M., . . . Panat, R. Ultrafast Fabrication of Thermoelectric Films by Pulsed Light Sintering of Colloidal Nanoparticles on Flexible and Rigid Substrates. *Advanced Engineering Materials* **21**, doi:10.1002/adem.201800800 (2019).
115 Park, S.-H., Jang, S., Lee, D.-J., Oh, J. & Kim, H.-S. Two-step flash light sintering process for crack-free inkjet-printed Ag films. *Journal of Micromechanics and Microengineering* **23**, doi:10.1088/0960-1317/23/1/015013 (2013).
116 Ma, S., Bromberg, V., Liu, L., Egitto, F. D., Chiarot, P. R. & Singler, T. J. Low temperature plasma sintering of silver nanoparticles. *Applied Surface Science* **293**, 207-215, doi:10.1016/j.apsusc.2013.12.135 (2014).
117 Shen, W., Zhang, X., Huang, Q., Xu, Q. & Song, W. Preparation of solid silver nanoparticles for inkjet printed flexible electronics with high conductivity. *Nanoscale* **6**, 1622-1628, doi:10.1039/c3nr05479a (2014).
118 Mo, L., Guo, Z., Wang, Z., Yang, L., Fang, Y., Xin, Z., . . . Li, L. Nano-Silver Ink of High Conductivity and Low Sintering Temperature for Paper Electronics. *Nanoscale Res Lett* **14**, 197, doi:10.1186/s11671-019-3011-1 (2019).
119 Huang, G. W., Xiao, H. M. & Fu, S. Y. Wearable Electronics of Silver-Nanowire/Poly(dimethylsiloxane) Nanocomposite for Smart Clothing. *Sci Rep* **5**, 13971, doi:10.1038/srep13971 (2015).
120 Kamyshny, A. & Magdassi, S. Conductive nanomaterials for printed electronics. *Small* **10**, 3515-3535, doi:10.1002/smll.201303000 (2014).
121 Choi, Y., Seong, K. d. & Piao, Y. Metal−Organic Decomposition Ink for Printed Electronics. *Advanced Materials Interfaces* **6**, doi:10.1002/admi.201901002 (2019).
122 Arafat, Y., Dutta, I. & Panat, R. On the deformation mechanisms and electrical behavior of highly stretchable metallic interconnects on elastomer substrates. *Journal of Applied Physics* **120**, 115103 (2016).
123 Xu, S., Zhang, Y., Cho, J., Lee, J., Huang, X., Jia, L., . . . Zhang, H. Stretchable batteries with self-similar serpentine interconnects and integrated wireless recharging systems. *Nature communications* **4**, 1-8 (2013).
124 Saleh, M. S., Hu, C., Brenneman, J., Al Mutairi, A. M. & Panat, R. 3D printed three-dimensional metallic microlattices with controlled and tunable mechanical properties. *Additive Manufacturing* **39**, doi:10.1016/j.addma.2021.101856 (2021).

125 Bai, J. G., Lei, T. G., Calata, J. N. & Lu, G.-Q. Control of nanosilver sintering attained through organic binder burnout. *Journal of Materials Research* **22**, 3494-3500, doi:10.1557/jmr.2007.0440 (2011).
126 Yan, H., Mei, Y.-H., Wang, M., Li, X. & Lu, G.-Q. Pressureless sintering multi-scale Ag paste by a commercial vacuum reflowing furnace for massive production of power modules. *Journal of Materials Science: Materials in Electronics* **30**, 9634-9641, doi:10.1007/s10854-019-01297-x (2019).
127 Zheng, H., Berry, D., Ngo, K. D. T. & Lu, G.-Q. Chip-Bonding on Copper by Pressureless Sintering of Nanosilver Paste Under Controlled Atmosphere. *IEEE Transactions on Components, Packaging and Manufacturing Technology* **4**, 377-384, doi:10.1109/tcpmt.2013.2296882 (2014).
128 Liu, S., Li, Y., Xing, S., Liu, L., Zou, G. & Zhang, P. Structure Inheritance in Nanoparticle Ink Direct-Writing Processes and Crack-Free Nano-Copper Interconnects Printed by a Single-Run Approach. *Materials (Basel)* **12**, doi:10.3390/ma12091559 (2019).
129 Dalal, N., Gu, Y., Hines, D. R., Dasgupta, A. & Das, S. Cracks in the 3D-printed conductive traces of silver nanoparticle ink. *Journal of Micromechanics and Microengineering* **29**, doi:10.1088/1361-6439/ab2f25 (2019).
130 Lee, D. J., Oh, J. H. & Bae, H. S. Crack formation and substrate effects on electrical resistivity of inkjet-printed Ag lines. *Materials Letters* **64**, 1069-1072, doi:10.1016/j.matlet.2010.02.014 (2010).
131 Prosser, J. H., Brugarolas, T., Lee, S., Nolte, A. J. & Lee, D. Avoiding cracks in nanoparticle films. *Nano Lett* **12**, 5287-5291, doi:10.1021/nl302555k (2012).
132 Scherer, G. W. Drying Gels: VIII. Revision and review. *Journal of Non-Crystalline Solids* **109**, 171-182 (1989).
133 Lee, W. P. & Routh, A. F. Why Do Drying Films Crack? *Langmuir* **20** (2004).
134 Routh, A. F. & Russel, W. B. Process Model for Latex Film Formation Limiting Regimes for Individual Driving Forces. *Langmuir* **15**, 7762-7773 (1999).
135 Schneider, C. A., Rasband, W. S. & Eliceiri, K. W. NIH Image to ImageJ: 25 years of image analysis. *Nat Methods* **9**, 671-675, doi:10.1038/nmeth.2089 (2012).
136 Cooper, S. J., Bertei, A., Shearing, P. R., Kilner, J. A. & Brandon, N. P. TauFactor: An open-source application for calculating tortuosity factors from tomographic data. *SoftwareX* **5**, 203-210, doi:10.1016/j.softx.2016.09.002 (2016).
137 ASTM. D3359 Standard Test Methods for Rating Adhesion by Tape Test. 2017
138 Scherer, G. W. Theory of Drying. *Journal of the American Ceramic Society* **73**, 3-14, doi:10.1111/j.1151-2916.1990.tb05082.x (1990).
139 Routh, A. F. Drying of thin colloidal films. *Rep Prog Phys* **76**, 046603, doi:10.1088/0034-4885/76/4/046603 (2013).
140 Greer, J. R. & Street, R. A. Mechanical characterization of solution-derived nanoparticle silver ink thin films. *Journal of Applied Physics* **101**, doi:10.1063/1.2735404 (2007).
141 Juillerat, F., Bowen, P. & Hofmann, H. Formation and drying of colloidal crystals using nanosized silica particles. *Langmuir* **22**, 2249-2257, doi:10.1021/la052304a (2006).
142 Salamanca, J. M., Ciampi, E., Faux, D. A., Glover, P. M., McDonald, P. J., Routh, A. F., . . . Keddie, J. L. Lateral Drying in Thick Films of Waterborne Colloidal Particles. *Langmuir* **17**, 3202-3207, doi:10.1021/la001590h (2001).

143 MEGlobal. Physical Properties of Ethylene Glycol. (2008).
144 Ando, K., Arakawa, M. & Terasaki, A. Evaporation Processes of a Liquid Droplet of Ethylene Glycol in a Vacuum. *Chemistry Letters* **45**, 961-963, doi:10.1246/cl.160381 (2016).
145 Su, Y.-Y., Marsh, A., Haddrell, A. E., Li, Z.-M. & Reid, J. P. Evaporation Kinetics of Polyol Droplets: Determination of Evaporation Coefficients and Diffusion Constants. *Journal of Geophysical Research: Atmospheres* **122**, 12,317-312,334, doi:10.1002/2017jd027111 (2017).
146 Rusdi, M., Moroi, Y., Nakahara, H. & Shibata, O. Evaporation from water-ethylene glycol liquid mixture. *Langmuir* **21**, 7308-7310, doi:10.1021/la040134g (2005).
147 Lei, T. G., Calata, J. N., Lu, G.-Q., Chen, X. & Luo, S. Low-Temperature Sintering of Nanoscale Silver Paste for Attaching Large-Area $({>}100~{\rm mm}^{2})$ Chips. *IEEE Transactions on Components and Packaging Technologies* **33**, 98-104, doi:10.1109/tcapt.2009.2021256 (2010).
148 Greer, J. R. & Street, R. A. Thermal cure effects on electrical performance of nanoparticle silver inks. *Acta Materialia* **55**, 6345-6349, doi:10.1016/j.actamat.2007.07.040 (2007).
149 Tjaden, B., Cooper, S. J., Brett, D. J. L., Kramer, D. & Shearing, P. R. On the origin and application of the Bruggeman correlation for analysing transport phenomena in electrochemical systems. *Current Opinion in Chemical Engineering* **12**, 44-51, doi:10.1016/j.coche.2016.02.006 (2016).
150 Rosker, E. S., Barako, M. T., Nguyen, E., DiMarzio, D., Kisslinger, K., Duan, D. W., . . . Tice, J. Approaching the Practical Conductivity Limits of Aerosol Jet Printed Silver. *ACS Appl Mater Interfaces* **12**, 29684-29691, doi:10.1021/acsami.0c06959 (2020).
151 Nguyen, T.-T., Demortière, A., Fleutot, B., Delobel, B., Delacourt, C. & Cooper, S. J. The electrode tortuosity factor: why the conventional tortuosity factor is not well suited for quantifying transport in porous Li-ion battery electrodes and what to use instead. *npj Computational Materials* **6**, doi:10.1038/s41524-020-00386-4 (2020).
152 Myllymaa, S., Pirinen, S., Myllymaa, K., Suvanto, M., Pakkanen, T. A., Pakkanen, T. T. & Lappalainen, R. Improving electrochemical performance of flexible thin film electrodes with micropillar array structures. *Measurement Science and Technology* **23**, doi:10.1088/0957-0233/23/12/125701 (2012).
153 Stauffer, F., Thielen, M., Sauter, C., Chardonnens, S., Bachmann, S., Tybrandt, K., . . . Voros, J. Skin Conformal Polymer Electrodes for Clinical ECG and EEG Recordings. *Adv Healthc Mater* **7**, e1700994, doi:10.1002/adhm.201700994 (2018).
154 Kim, T., Park, J., Sohn, J., Cho, D. & Jeon, S. Bioinspired, Highly Stretchable, and Conductive Dry Adhesives Based on 1D-2D Hybrid Carbon Nanocomposites for All-in-One ECG Electrodes. *ACS Nano* **10**, 4770-4778, doi:10.1021/acsnano.6b01355 (2016).
155 Wang, L., Xu, T. & Zhang, X. Multifunctional conductive hydrogel-based flexible wearable sensors. *TrAC Trends in Analytical Chemistry* **134**, doi:10.1016/j.trac.2020.116130 (2021).
156 Cao, J., Yang, X., Rao, J., Mitriashkin, A., Fan, X., Chen, R., . . . Ouyang, J. Stretchable and Self-Adhesive PEDOT:PSS Blend with High Sweat Tolerance as Conformal Biopotential Dry Electrodes. *ACS Appl Mater Interfaces* **14**, 39159-39171, doi:10.1021/acsami.2c11921 (2022).

157 Yamamoto, Y., Yamamoto, D., Takada, M., Naito, H., Arie, T., Akita, S. & Takei, K. Efficient Skin Temperature Sensor and Stable Gel-Less Sticky ECG Sensor for a Wearable Flexible Healthcare Patch. *Adv Healthc Mater* **6**, doi:10.1002/adhm.201700495 (2017).
158 Kim, D. H., Lu, N., Ma, R., Kim, Y. S., Kim, R. H., Wang, S., . . . Rogers, J. A. Epidermal electronics. *Science* **333**, 838-843, doi:10.1126/science.1206157 (2011).
159 Fan, J. A., Yeo, W. H., Su, Y., Hattori, Y., Lee, W., Jung, S. Y., . . . Rogers, J. A. Fractal design concepts for stretchable electronics. *Nat Commun* **5**, 3266, doi:10.1038/ncomms4266 (2014).
160 Xu, R., He, P., Lan, G., Behrouzi, K., Peng, Y., Wang, D., . . . Lin, L. Facile Fabrication of Multilayer Stretchable Electronics via a Two-mode Mechanical Cutting Process. *ACS Nano*, doi:10.1021/acsnano.1c10011 (2021).
161 Guo, L. & DeWeerth, S. P. High-density stretchable electronics: toward an integrated multilayer composite. *Adv Mater* **22**, 4030-4033, doi:10.1002/adma.201000515 (2010).
162 Huang, Z., Hao, Y., Li, Y., Hu, H., Wang, C., Nomoto, A., . . . Xu, S. Three-dimensional integrated stretchable electronics. *Nature Electronics* **1**, 473-480, doi:10.1038/s41928-018-0116-y (2018).
163 Jiang, Q., Zhang, S., Jiang, J., Fei, W. & Wu, Z. Pneumatic Enabled Vertical Interconnect Access of Liquid Alloy Circuits toward Highly Integrated Stretchable Electronics. *Advanced Materials Technologies* **6**, doi:10.1002/admt.202000966 (2021).
164 Song, H., Luo, G., Ji, Z., Bo, R., Xue, Z., Yan, D., . . . Zhang, Y. Highly-integrated, miniaturized, stretchable electronic systems based on stacked multilayer network materials. *Sci Adv* **8**, eabm3785, doi:10.1126/sciadv.abm3785 (2022).
165 Jing, Q., Choi, Y. S., Smith, M., Ou, C., Busolo, T. & Kar-Narayan, S. Freestanding Functional Structures by Aerosol-Jet Printing for Stretchable Electronics and Sensing Applications. *Advanced Materials Technologies* **4**, doi:10.1002/admt.201900048 (2019).
166 van den Brand, J., de Kok, M., Koetse, M., Cauwe, M., Verplancke, R., Bossuyt, F., . . . Vanfleteren, J. Flexible and stretchable electronics for wearable health devices. *Solid-State Electronics* **113**, 116-120, doi:10.1016/j.sse.2015.05.024 (2015).
167 Zhou, L. y., Fu, J. z., Gao, Q., Zhao, P. & He, Y. All-Printed Flexible and Stretchable Electronics with Pressing or Freezing Activatable Liquid-Metal–Silicone Inks. *Advanced Functional Materials* **30**, doi:10.1002/adfm.201906683 (2019).
168 Saleh, M. S., Ritchie, S. M., Nicholas, M. A., Gordon, H. L., Hu, C., Jahan, S., . . . Panat, R. P. CMU Array: A 3D nanoprinted, fully customizable high-density microelectrode array platform. *Sci Adv* **8**, eabj4853, doi:10.1126/sciadv.abj4853 (2022).
169 Ren, P. & Dong, J. Direct Fabrication of VIA Interconnects by Electrohydrodynamic Printing for Multi-Layer 3D Flexible and Stretchable Electronics. *Advanced Materials Technologies* **6**, doi:10.1002/admt.202100280 (2021).
170 Tansel, D. Z., Brenneman, J., Panat, R. & Fedder, G. K. in *2022 IEEE 35th International Conference on Micro Electro Mechanical Systems Conference (MEMS)* 353-356 (2022).

171 Davis, P. D., Parbrook, G. D. & Kenny, G. N. C. in *Basic Physics and Measurement in Anaesthesia (Fourth Edition)* (eds P. D. Davis, G. D. Parbrook, & G. N. C. Kenny) 171-188 (Butterworth-Heinemann, 1995).

Appendices

Appendix 1. Contribution of Work

Sub Project	Task	Lead Student	Status
Mechanical Characterization of PDMS (Chapter 3)	1. Stretchable Substrate Fabrication	D. Tansel	Published[1]
	2. Mechanical testing	D. Tansel	
	3. Hyperelastic model fitting	J. Brenneman	
Vapor Driven Delamination (Chapter 4)	1. Stretchable Substrate Fab	D. Tansel	Published[2]
	2. Printing of Interconnect	J. Brenneman	
	3. Thermal treatment	D. Tansel	
	4. Imaging of Interconnects	D. Tansel J. Brenneman	
	5. Theoretical and Numerical Modeling	J. Brenneman	
Cracking and conductivity of Ag Interconnect (Chapter 5)	1. Stretchable Substrate Fab	D. Tansel	Published[3]
	2. Printing of Interconnect	J. Brenneman	
	3. Thermal treatment	D. Tansel	
	4. SEM and FIB cross sectioning	J. Brenneman	
	5. Theoretical Modeling	J. Brenneman	
3D stretchable Interconnect Mechanical Characterization (Chapter 6)	1. Design of Interconnect Geometry	J. Brenneman	Paper in Progress[4]
	2. Stretchable Substrate Fab	D. Tansel	
	3. Printing of Interconnect	J. Brenneman	
	4. Thermal Treatment	D. Tansel	
	5. Mechanical Characterization	J. Brenneman	
	6. Electrical Characterization	D. Tansel	
ECG electrode demonstration (Chapter 6)	1. Prototype ECG design	J. Brenneman	Paper in Progress[4]
	2. Stretchable Substrate Fab	D. Tansel	
	3. Printing of ECG patch	J. Brenneman	
	4. Imaging of ECG patch	D. Tansel J. Brenneman	
	5. Electrical characterization of ECG patch	D. Tansel	

1. Tansel, D. Z., Brenneman, J., Fedder, G. K., & Panat, R. (2020). Mechanical characterization of polydimethylsiloxane (PDMS) exposed to thermal histories up to 300 °C in a vacuum environment. *Journal of Micromechanics and Microengineering, 30*(6). doi:10.1088/1361-6439/ab82f4
2. Brenneman, J., Tansel, D. Z., Fedder, G. K., & Panat, R. (2021). Interfacial delamination and delamination mechanism maps for 3D printed flexible electrical interconnects. *Extreme Mechanics Letters*, 43. doi:10.1016/j.eml.2021.101199
3. Brenneman, J., Tansel, D. Z., Fedder, G. K., & Panat, R. (2022). High-Conductivity Crack-Free 3D Electrical Interconnects Directly Printed on Soft PDMS Substrates. *Advanced Materials Technologies*. doi:10.1002/admt.202200396
4. Brenneman, J., Tansel, D. Z., Fedder, G. K., & Panat, R. (In Process). Stretchable Multi-Layer Wearable Electrode Patch with Microscale VIAs Fabricated using 3D Aerosol Jet Printing.

In addition to the research covered in this thesis, I contributed to and led other projects that were fruitful during my tenure as a PhD student. Using the same aerosol jet printing process, I contributed to the fabrication of lattice structures that were then compressed in a microscale compression tester which is similar set up to the pillar shear test set-up covered in Chapter 5. I developed a semi-empirical model that captured the oscillations associated with the layer-by-layer collapse of the structural lattice. This resulted in a publication in Additive Manufacturing.

5. Saleh, M. S., Hu, C., Brenneman, J., Al Mutairi, A. M., & Panat, R. (2021). 3D printed three-dimensional metallic microlattices with controlled and tunable mechanical properties. *Additive Manufacturing*, 39. doi:10.1016/j.addma.2021.101856

I further developed the oscillation model and applied it to previously published data to investigate the effects of material composition, fabrication technique, and lattice shape on the oscillation behavior, collapse stress, and energy absorption of the structural lattice. This work is currently under review at Advanced Engineering Materials.

6. Brenneman, J., Lovalekar, M., & Panat, R. (Under Review). A semi-empirical model for post-yield stress-instability in the stress-strain response of three-dimensional lattice structures under compressive loads. *Advanced Engineering Materials*